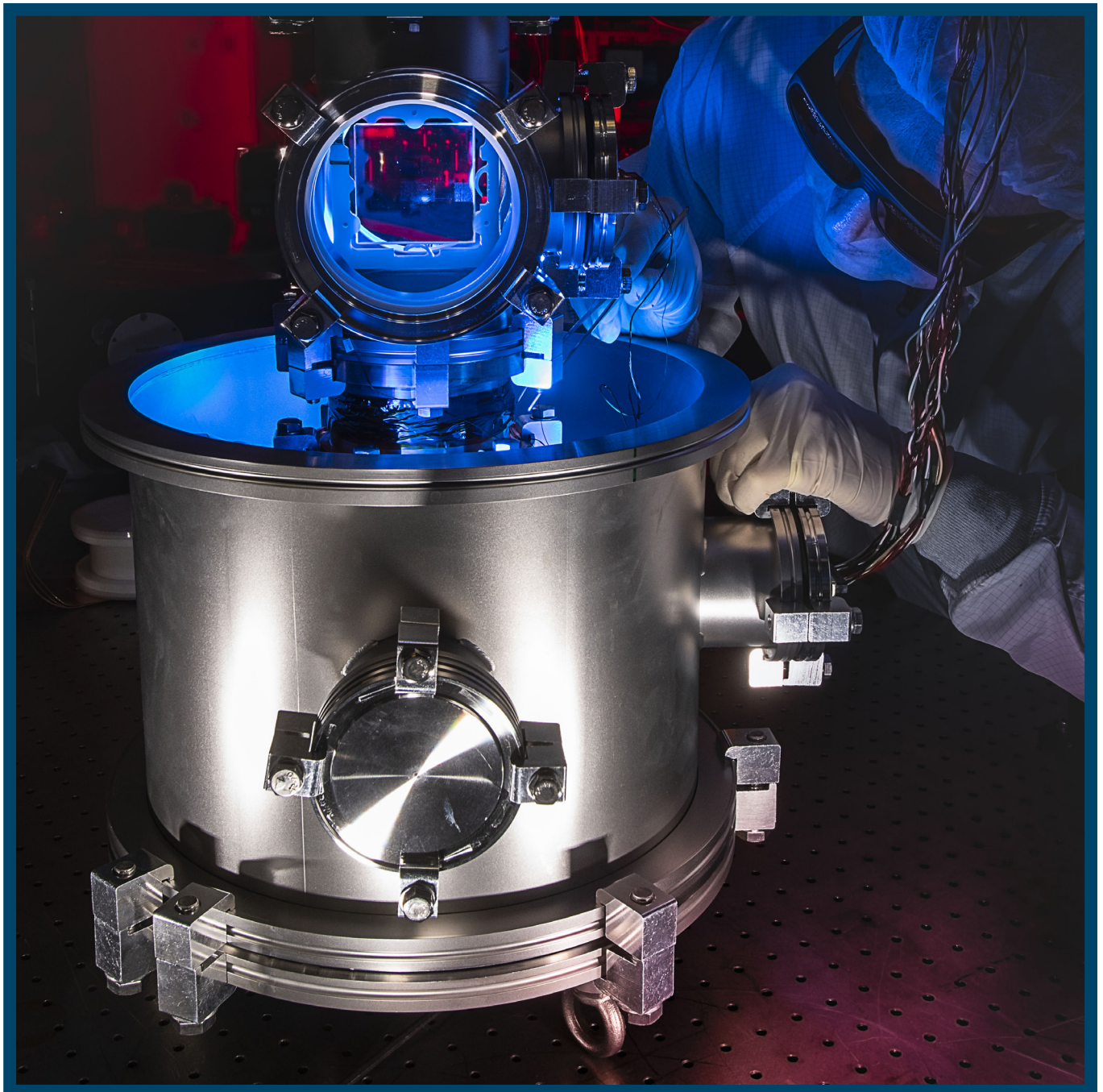# LLE Review

Quarterly Report

UR
LLE

About the Cover:

The photo on the cover shows Research Engineer Ildar Begishev adjusting thermostatic sensors on the internal chamber of a two-chamber cryostat. The cryostat is used to cool down nonlinear ammonium dihydrogen phosphate (ADP) crystals to –70°C in order to generate the fifth harmonic (211 nm) of a neodymium laser. The deep ultraviolet (UV) laser beam is necessary to measure density of a high-temperature plasma. Phase matching for the fifth-harmonic–generation process is extremely sensitive to the crystal temperature, and this unique two-chamber cryostat allows one to hold the temperature at a given level across the entire aperture of a 65-mm × 65-mm crystal with an accuracy better than 0.1°C. As result, 26% of input laser energy was transformed into a UV beam at 211 nm—a record for conversion efficiency.

The photo to the right presents a section of the Multi-Terawatt (MTW) laser. Dr. Begishev is preparing the experimental setup to generate the fifth harmonic in the two-chamber cryostat, shown in the center. The inset shows the ADP crystal inside the two-chamber cryostat. This research was provided in collaboration with Livermore Lawrence National Laboratory.

LLE Review

Quarterly Report

UR
LLE

Contents

In Brief

This volume of LLE Review 157, covering the period October–December 2018, is sectioned among research areas at LLE and external users of the Omega Laser Facility. Articles appearing in this volume are the principal summarized results of long-form research articles. Readers seeking a more-detailed account of research activities are invited to seek out the primary materials appearing in print, detailed in the publications and presentations section at the end of this volume.

Highlights of research presented in this volume include the following:

- Igumenshchev *et al.* review the consequences of rarefaction flows on mitigation of laser imprint in direct-drive implosions (p. 1). Rarefaction flows can result in a decay of imprinted modulations during early hydrodynamic evolution. Three-dimensional *ASTER* simulations were used to demonstrate the mechanism and achieve performance closer to that of 1-D simulations when the implosion develops an after-shock rarefaction flow than in designs without such flow.

- Davies *et al.* infer the fuel areal density of laser-driven magnetized liner implosions on OMEGA from secondary neutron yields (p. 3). The results broadly indicate discrepancy between 1-D and 2-D simulation predictions and the experimentally measured areal density and convergence ratio.

- Milder *et al.* present a statistical study on the implications of non-Maxwellian electron velocity distribution functions on the inference of plasma parameters using collective Thomson scattering (p. 6). Small changes in the shape of the distribution function are found to be the limiting factor in the determination of plasma conditions.

- Henchen *et al.* infer heat flux through laser-produced coronal plasma using collective Thomson scattering (p. 8). The results of the experiment suggest that classical thermal transport theory is not valid in plasma with steep temperature gradients.

- Karasiev *et al.* present a report on the status of free-energy representations for homogeneous electron gas (p. 10). The equivalence between three global representations of the free energy, the Karasiev–Sjostrom–Dufty–Trickey (KSDT) representation; its descendant, the corrected KSDT; and the Groth–Dornheim–Bonitz parameterization are demonstrated through their correspondence with quantum Monte Carlo results of Dornheim *et al.*

- An electron spectrometer with multiple viewing angles has been developed for the OMEGA ten-inch–manipulator diagnostic platform (p. 13). Habara *et al.* discuss how this versatile diagnostic can be deployed on the OMEGA and OMEGA EP Laser Systems.

- Serafini *et al.* studied the ultrafast optical properties of single-crystal cadmium magnesium telluride for use in x-ray radiation detectors (p. 15). The carrier recombination and trapping components of electronic relaxation are analyzed with a coupled rate-equation model.

- Begishev *et al.* present the fifth-harmonic conversion of a neodymium glass laser using large-aperture ammonium dihydrogen phosphate (ADP) crystals (p. 18). Phase-matching conditions for the sum-frequency generation are reached by cooling ADP crystals to –70°C.

- Kafka and Demos study the interaction of 10-ps and 0.6-ps laser pulses with microparticles located on the surface of a multi-layer dielectric mirror (p. 21). These findings aid in understanding and assessing the risk of contamination-induced damage in short-pulse laser systems.

- Kosc *et al*. study the laser-induced–damage threshold for nematic liquid crystals at pulse durations from 600 fs to 1.5 ns (p. 24). Such data provide guidance for future applications in high-power and/or peak intensity laser systems.

- Demos *et al*. study the dominant mechanisms of laser-induced damage in optical materials with 355-nm, ~1-ns pulses (p. 27). The study finds two damage pathways for the optical material, arising from self-focusing, which is caused by refractive index change from electron energy transition in the material, and from local intense heating causing above-melting temperatures near the surface of the material.

- Shmayda *et al*. present a process for extracting tritium from contaminated water using combined electrolysis and catalytic exchange (p. 30). This process provides an economical and robust form of tritium recovery.

- Sharpe *et al*. quantify the distribution of tritium in the near surface of stainless-steel alloy 316 (p. 33). Such measurements inform understanding of tritium migration through stainless steel with implications for decontamination.

- Ghosh *et al*. present cathodic electrolytic deposition used to synthesize nanoscale copper-hydroxyapatite coatings for antibacterial implants (p. 36). Results show the copper nanoparticles reduced numbers of *E. Coli* and *S. aureus* by 78% and 83%, respectively.

- Zhang *et al*. study the effect of heat treatment of silver hydroxyapatite coatings on the antibacterial properties of the coating (p. 38). The results demonstrate that heat treatment enhances the antibacterial coating and reduces variability.

- Koroliov *et al*. use terahertz time-domain spectroscopy (THz-TDS) to characterize graphene nanofiller within nanocomposite materials (p. 40). The THz-TDS method probes the dielectric properties of the sample, providing global information regarding the dispersion of graphene and its *in-situ* electronic quality.

- Kruschwitz *et al*. present a wavelength-tunable ultraviolet beam on OMEGA EP (p. 43). This upgrade allows experiments to characterize the interaction of the tunable beam with one or more fixed-wavelength beams on OMEGA.

- In order to characterize on-shot conditions, LLE has built a full-beam-in-tank (FBIT) diagnostic to characterize the OMEGA focal spot. Waxer *et al*. discuss how these results provide a measure of the on-shot laser uniformity on target from data collected inside the target chamber (p. 46).

- Bauer *et al*. compare results from FBIT data to equivalent-target-plane (ETP) measurements for the OMEGA focal spot (p. 49). Preliminary data suggest that upstream diagnostics such as the ETP compare closely with the results found using FBIT.

- Sampat *et al*. report on efforts to achieve power balance requirements for OMEGA to less than 1% rms (p. 52). Management of saturation in the stage-E and F amplifiers is shown to provide control of beam power while maintaining the requested pulse shape.

- Puth *et al*. summarize operations of the Omega Laser Facility during the first quarter of the FY19 reporting period (p. 54).

- Frenje *et al*. present a study of stopping power for low-Z materials near the Bragg peak (p. 56). Data show good agreement in most cases for electron–ion Coulomb scattering except for DD-t, which is postulated to depend more strongly on ion–ion nuclear elastic scattering than predicted.

- Sio *et al*. measure the relative timing between the nuclear reaction history of different fuel-ion (D, T, ^{3}He) populations using a particle x-ray temporal diagnostic (p. 59). The observed rate histories are more closely represented with a kinetic-ion model as compared with average-ion fluid models.

Steven T. Ivancic
Editor

Rarefaction Flows and Mitigation of Imprint in Direct-Drive Implosions

I. V. Igumenshchev,[1] A. L. Velikovich,[2] V. N. Goncharov,[1] R. Betti,[1] E. M. Campbell,[1] J. P. Knauer,[1] S. P. Regan,[1] A. J. Schmitt,[2] R. C. Shah,[1] and A. Shvydky[1]

[1]Laboratory for Laser Energetics, University of Rochester
[2]Plasma Physics Division, Naval Research Laboratory

A 3-D hydrodynamic simulation using the code *ASTER*[1] helped to identify a new mechanism that is responsible for mitigating imprint with a scale length corresponding to Legendre modes down to $\ell \simeq 30$ in direct-drive OMEGA implosions[2] driven by laser pulses with a picket(s). This mechanism involves rarefaction flows developed by unsupported shocks. Rarefaction flows can result in a decay of imprint modulations in implosion shells during their early evolution, consequently improving the stability of these shells with respect to the acceleration Rayleigh–Taylor (RT)[3] growth at a later time.

Figure 1 illustrates the development of imprint modulations in implosion shells compressed by supported and unsupported shocks, which are produced by continuous and picket laser pulses, respectively. The green areas at the ablation front indicate the locations of modulations originating from laser nonuniformities in the beginning of the pulses. These modulations can feed through to the shell (to the left) in the case of a supported shock [Fig. 1(a)] and cannot feed through in the case of a unsupported shock, which develops a post-shock rarefaction flow [Fig. 1(b)]. As a result, imprint is mitigated only in the latter case, in which modulations are localized near the ablation front and moved away (to the right) with the ablating mass.
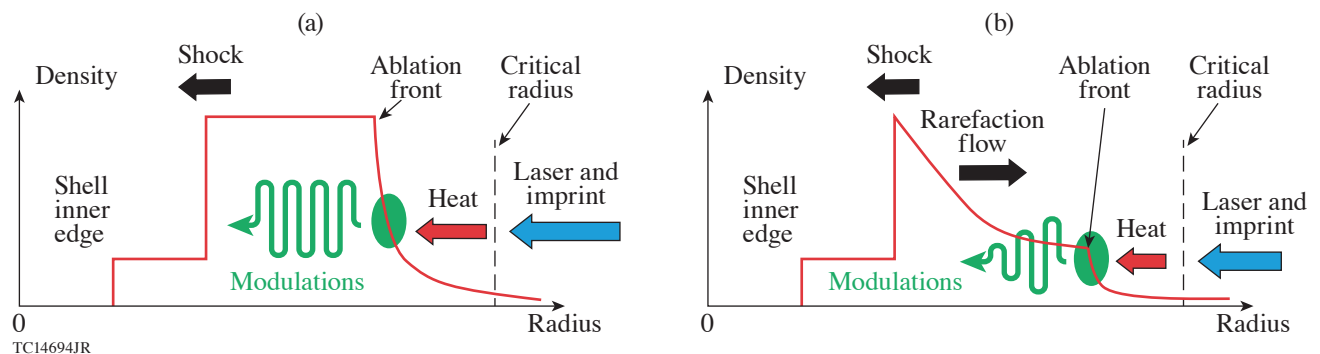
Figure 1
(a) Imprint modulations (the green area) localized at the ablation front can feed through to an implosion shell compressed by a supported shock but (b) cannot feed through in a shell compressed by an unsupported shock.

Three-dimensional *ASTER* simulations were used to demonstrate the new mechanism and employed two OMEGA cryogenic implosion designs having laser pulses with and without a picket. Simulations show that imprint is not mitigated in the no-picket design; therefore, large seeds for RT growth during the target acceleration phase are provided, resulting in a "broken shell" just prior to the target deceleration phase [see Fig. 2(a)]. This implosion shows poor performance, producing only 13% of neutron yield and 37% of neutron-averaged areal mass predicted in 1-D (symmetric) simulations. Contrary to this, simulations of the single-picket design, which develops an after-shock rarefaction flow, show apparent mitigation of the dangerous imprint modes $\ell \sim 100$ to 200. This implosion is characterized by relatively small-amplitude perturbations in the shell with dominant modes $\ell \sim$ 30 to 60 [see Fig. 2(b)] and produces 46% of neutron yield and 81% of neutron-averaged areal mass of those in 1-D simulations.
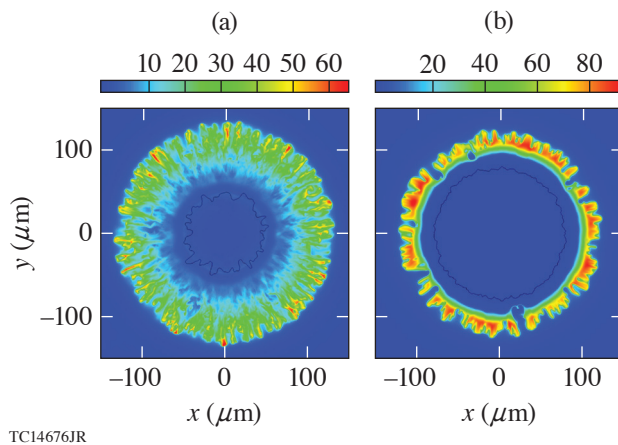
Figure 2

Meridional cross sections of the distribution of density (in g/cm^3) from 3-D simulations of the designs using the (a) no-picket and (b) single-picket laser pulses. The images are shown at times corresponding to moments prior to deceleration of the implosion shells.

TC14676JR

1. I. V. Igumenshchev *et al.*, Phys. Plasmas **23**, 052702 (2016).

2. T. R. Boehly *et al.*, Opt. Commun. **133**, 495 (1997).

3. Lord Rayleigh, Proc. London Math Soc. **XIV**, 170 (1883); G. Taylor, Proc. R. Soc. London Ser. A **201**, 192 (1950).

Inferring Fuel Areal Density from Secondary Neutron Yields in Laser-Driven Magnetized Liner Inertial Fusion

J. R. Davies,[1] D. H. Barnak,[1,2] R. Betti,[1] E. M. Campbell,[1] V. Yu. Glebov,[1] E. C. Hansen,[1,3] J. P. Knauer,[1] J. L. Peebles,[1] and A. B. Sefkow[1]

[1]Laboratory for Laser Energetics, University of Rochester
[2]Los Alamos National Laboratory
[3]FLASH Center, University of Chicago

Laser-driven magnetized liner inertial fusion (MagLIF[1]) experiments are being carried out on the OMEGA laser[2–6] to study scaling by providing data from targets ~10× smaller in linear dimensions than those used on the Z pulsed-power machine[7–9] at Sandia National Laboratories. One of the key initial design criteria in the development of MagLIF[1] was to find a means to achieve fusion conditions in a cylindrical implosion at a convergence ratio of less than 30. It is well-known that high-convergence implosions are very sensitive to small departures from symmetry in the drive and targets, making them impractical. By preheating to ~100 eV, temperatures up to 9 keV can be achieved in an adiabatic, cylindrical compression with a convergence ratio <30. In MagLIF an axial magnetic field reduces electron thermal conduction from the fuel into the liner during compression, making it possible to achieve a near-adiabatic compression at a lower implosion velocity. With the compressed axial magnetic field, alpha particles can be confined from deuterium–tritium (D–T) fusion without reaching a radial areal density of $\rho R \sim 0.6$ g/cm^2, if, instead, a radially integrated axial magnetic field $BR \sim 0.6$ T·m is achieved. In experiments on Z, the radially integrated axial magnetic field in the compressed deuterium fuel was inferred to be ~0.4 T·m from the ratio of secondary D–T fusion neutrons to primary D–D fusion neutrons.[9] The D–D fusion reaction has two equally probable branches:

$$D + D \longrightarrow T(1.01\,\text{MeV}) + p(3.02\,\text{MeV})$$

$$\longrightarrow {}^3\text{He}(0.82\,\text{MeV}) + n(2.45\,\text{MeV}), \tag{1}$$
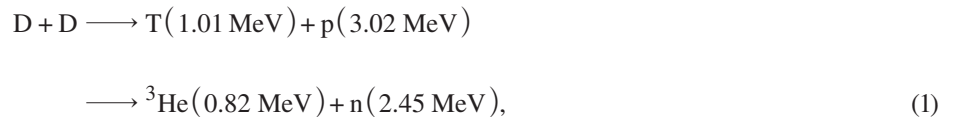
where the kinetic energies given in parentheses are in the center of the momentum frame. The tritium may go on to fuse with the deuterium, producing secondary 14.5-MeV neutrons. The longer the path length of the tritium in the deuterium, and the higher the density of the deuterium, the greater the probability of D–T fusion. Calculations indicated that for the Z experiments, the increase in path length of the tritium resulting from the compressed axial magnetic field was a major contributor to the secondary D–T yield.[9] The BR in MagLIF targets on OMEGA will be at least ~10× lower than on Z because the radius is 10× smaller and the initial axial magnetic field is approximately the same (currently 9 T, but values up to 30 T can be achieved). Therefore, magnetic confinement of charged fusion products cannot be achieved on OMEGA. As a result, the secondary D–T yield from D$_2$ fuel is determined by the radial areal density ρR of the compressed fuel.[10] While not an important metric for MagLIF, fuel areal density does provide useful information on the convergence ratio of the fuel, which cannot be determined from the x-ray imaging diagnostics available on OMEGA[4] because they do not have sufficient spatial resolution for a compressed fuel that should be <10 μm in radius.

The fuel areal density can be obtained approximately from

$$\rho R = 5.18 \pm 1.04 \frac{Y_{\text{DT}}}{Y_{\text{DD}}} \text{ g/cm}^2, \tag{2}$$

assuming a point or line source of tritium on the axis, and straight-line propagation of the tritium with no energy loss and no end losses. The result is only weakly dependent on the radial distribution of the tritium production. For the increase in D–T fusion cross section caused by collisional slowing of the tritium to be negligible, and for angular scattering to be negligible, requires

$$\rho R \ll 14.5 T_{\text{keV}}^{3/2} \text{ mg/cm}^2. \tag{3}$$

For end losses to reduce the mean path length by less than 10% requires

$$\frac{L}{R} > 12, \tag{4}$$

where L is the length of the cylinder. For the magnetic field to cause a negligible increase in path length requires

$$BR \ll 0.25 \text{ T·m.} \tag{5}$$

All of these conditions are comfortably satisfied in laser-driven MagLIF experiments on OMEGA.

Successful laser-driven MagLIF shots have been taken with all four combinations of preheat on/off and axial magnetic field on/off for 1.8 mg/cm^3 of deuterium and for compression-only and compression with field for 1.2 mg/cm^3 of deuterium. The inferred areal density by type of shot is given in Table I.

TABLE I: Areal density ρR and the increase in areal density $C_0 = \rho R/(\rho R)_0$ inferred from measured secondary- to primary-yield ratios by shot type and obtained from 1-D *LILAC* and 2-D *HYDRA* simulations for nominal laser and target parameters. For the integrated shot and the compression-only shots at 1.2 mg/cm^3, the upper limit is based on a D–T yield $<2 \times 10^5$.

Type (number of shots)	ρR (mg/cm^2)	$\rho R_{1\text{-D}}$ (mg/cm^2)	$\rho R_{2\text{-D}}$ (mg/cm^2)	C_0	$C_{0,1\text{-D}}$	$C_{0,2\text{-D}}$
Compression only: 1.8 mg/cm^3 (2)	1.2±0.4	3.8	3.3	22±7	77	68
Preheated: 1.8 mg/cm^3 (2)	0.98±0.39	2.2	1.7	19±8	46	35
Magnetized: 1.8 mg/cm^3 (2)	0.67±0.08	1.7	1.9	13±2	34	39
Integrated: 1.8 mg/cm^3 (1)	<0.64	1.6	1.4	<13	32	29
Compression only: 1.2 mg/cm^3 (2)	<2.7	2.2	3.4	<82	70	100
Magnetized: 1.2 mg/cm^3 (2)	1.2±0.3	1.2	1.5	37±8	37	46

The fuel convergence ratio is of more interest in MagLIF than the areal density; both the initial Z point design[1] and the OMEGA point design[3] set out to achieve a convergence ratio of 25. If the fuel density profile remains uniform and there are no end losses, the fuel convergence ratio is $\rho R/(\rho R)_0$, which we will refer to as C_0, our zeroth-order estimate of a neutron-averaged fuel convergence, the values of which are given in Table I. When fuel density peaks at the edge, which is to be expected, C_0 will underestimate the convergence ratio; if fuel density peaks at the center, C_0 will overestimate the convergence ratio. End losses, which are to be expected, will result in C_0 underestimating the convergence ratio. Therefore, we expect C_0 to be somewhat lower than the actual convergence ratio C.

Even if the actual convergence ratio is as high as $2C_0$, the integrated shot has achieved a convergence ratio <26, meeting our initial point design objective, despite the lower fuel density. In any case, the values of C_0 should provide an indication of how the fuel convergence ratio is modified by preheating, magnetization, and fuel density, which are important aspects of MagLIF. The results indicate that preheating, magnetization, and increasing fuel density reduce the fuel convergence ratio, as expected.

The inferred areal densities also provide a useful point of comparison with simulations. Areal densities from 1-D *LILAC*[3,4] and 2-D *HYDRA*[3,4,6] are included in Table I. The simulations overestimate the areal densities for all except the magnetized 1.2-mg/cm^3 shots, where agreement is good, although the 2-D simulations are toward the upper end of the error bar. The simulations give values of C_0 that are 2× to 3× higher than the measurements, excluding the 1.2-mg/cm^3 results. The simulations would be expected to overestimate the areal density because the growth of nonuniformities from the laser beams and targets, which are not considered, will break up the compressed fuel. In 1-D and 2-D the imploding shell must converge on the axis and will stop only once the pressure in the fuel becomes high enough. In 3-D, opposing elements of the shell can miss the axis and not compress the fuel to such a high pressure. The growth of nonuniformities is expected to be greater the higher the convergence, and the discrepancies between the measured and simulated areal densities are greater at higher values, excluding the 1.2-mg/cm^3 results. It is possible that the agreement between measurements and simulations for magnetized 1.2-mg/cm^3 shots is just a matter of chance, with the actual value lying at the lower end indicated by the experimental uncertainty, particularly as the D–T yields in these shots are at the very lowest detectable levels.

The areal density diagnostic described here will be applied to future laser-driven MagLIF shots that will include higher magnetic fields (up to ~30 T), a scan of preheat energies, and higher fuel densities. The simulations will be extended to 3-D, using laser and target parameters as close as possible to the as-shot values, and the effects of cross-beam energy transfer and nonlocal thermal transport will be taken into consideration.

1. S. A. Slutz *et al.*, Phys. Plasmas **17**, 056303 (2010).

2. D. H. Barnak *et al.*, Phys. Plasmas **24**, 056310 (2017).

3. J. R. Davies *et al.*, Phys. Plasmas **24**, 062701 (2017).

4. E. C. Hansen *et al.*, Plasma Phys. Control. Fusion **60**, 054014 (2018).

5. J. R. Davies *et al.*, Phys. Plasmas **25**, 062704 (2018).

6. E. C. Hansen *et al.*, Phys. Plasma **25**, 122701 (2018).

7. A. B. Sefkow *et al.*, Phys. Plasmas **21**, 072711 (2014).

8. M. R. Gomez *et al.*, Phys. Rev. Lett. **113**, 155003 (2014).

9. P. F. Schmit *et al.*, Phys. Rev. Lett. **113**, 155004 (2014).

10. E. G. Gamaliĭ *et al.*, JETP Lett. **21**, 70 (1975); H. Azechi *et al.*, Appl. Phys. Lett. **49**, 555 (1986); M. D. Cable and S. P. Hatchett, J. Appl. Phys. **62**, 2233 (1987); S. Kurebayashi *et al.*, Phys. Plasmas **12**, 032703 (2005).

Impact of Non-Maxwellian Electron Velocity Distribution Functions on Inferred Plasma Parameters in Collective Thomson Scattering

A. L. Milder,[1,2] S. T. Ivancic,[1] J. P. Palastro,[1] and D. H. Froula[1,2]

[1]Laboratory for Laser Energetics, University of Rochester
[2]Department of Physics and Astronomy, University of Rochester

Optical Thomson scattering is a powerful diagnostic that is widely used to measure plasma conditions in laser-produced plasmas.[1] As large multibeam facilities are constructed to achieve inertial confinement fusion around the world,[2–4] accurate measurements of plasma conditions are becoming increasingly important for understanding the importance of missing physics in the large hydrodynamic simulations. Local and time-resolved measurements of Thomson-scattered spectra have provided valuable insight into a range of studies, including laser–plasma instabilities,[2] thermal transport,[5] and more generally inertial confinement fusion.[6,7]

The high density present in laser-produced plasmas results in scattering optical light from collective plasma-wave fluctuations. The scattering from low-frequency fluctuations generates ion-acoustic spectral features, while scattering from high-frequency fluctuations generates electron plasma wave spectral features. Early collective scattering measurements from high-frequency fluctuations used the theory developed two decades earlier by Salpeter[8] to associate the wavelength of spectral peaks with density, through the Bohm–Gross dispersion relation, and the width of spectral peaks to temperature, through Landau damping, but the small scattering cross section for Thomson scattering has resulted in relatively few experiments where electron temperature and density were measured from the electron plasma wave features.[6,9–11] Recent experiments have used the full Thomson-scattered spectrum to extract plasma conditions, but these studies have been limited to assuming Maxwellian distribution functions. However, variation in the shape of the distribution functions can lead to significant changes to the Thomson-scattering spectrum.[12]

Here, we investigate the sensitivity of electron temperature and density inferred from collective Thomson scattering to non-Maxwellian electron distribution functions. Analyzing synthetic electron plasma wave Thomson-scattering spectra, under the false assumption that the electron distribution function is Maxwellian, can lead to gross errors in the inferred electron density and temperature. Figure 1 shows that the inferred temperature and density can differ from the actual values by 50% and 30%, respectively. These errors stem from changes in the shape of the scattered spectra and can be removed by including the correct shape of the electron distribution function in the analysis. Other changes to the shape of the electron distribution function can result in errors in the inferred parameters, as in the case of heat flux.[7] These errors of 50% in temperature and 30% in density are for extreme changes to the electron distribution function, but even for small changes in the shape of the distribution function, the errors in temperature and density are larger than the statistical uncertainty of ~5% that is typical[10,11] and can be a limiting factor in determining plasma conditions.
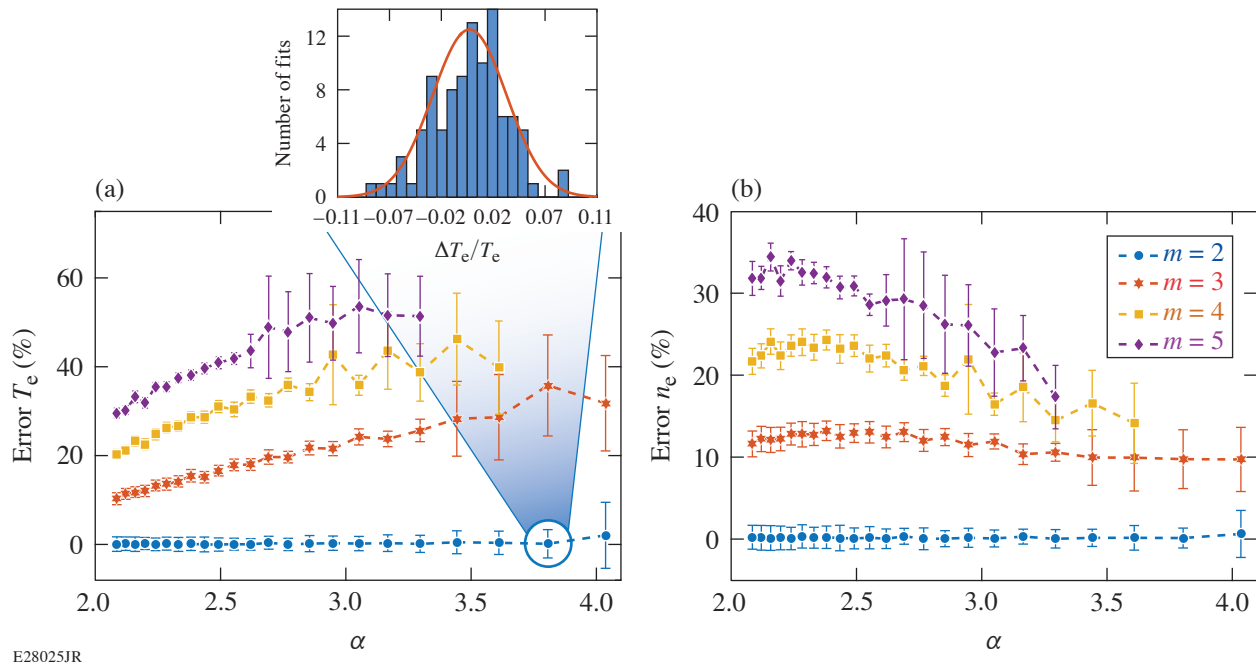
E28025JR

Figure 1

Percent error in (a) temperature and (b) density as a function of the normalized phase velocity $\left(\alpha = v_\phi / v_{\text{th}}\right)$ when the fit model assumes a Maxwellian electron distribution function and the true electron distribution function is super-Gaussian. The absolute difference between the inferred and actual parameter dividend by the actual parameter (percent error) is calculated for a range of phase velocities. The values for four different super-Gaussian orders are plotted in different colors with error bars that represent the standard deviation of 100 fits.

1. D. H. Froula *et al.*, *Plasma Scattering of Electromagnetic Radiation: Theory and Measurement Techniques*, 2nd ed. (Academic Press, Amsterdam, 2011).

2. C. A. Haynam *et al.*, Appl. Opt. **46**, 3276 (2007).

3. J. L. Miquel, C. Lion, and P. Vivini, J. Phys.: Conf. Ser. **688**, 012067 (2016).

4. W. Zheng *et al.*, High Power Laser Sci. Eng. **4**, e21 (2016).

5. R. J. Henchen *et al.*, Phys. Rev. Lett. **121**, 125001 (2018).

6. S. H. Glenzer *et al.*, Phys. Plasmas **6**, 2117 (1999).

7. D. H. Froula *et al.*, Phys. Plasmas **13**, 052704 (2006).

8. E. E. Salpeter, Phys. Rev. **120**, 1528 (1960).

9. J. S. Ross *et al.*, Phys. Rev. Lett. **104**, 105001 (2010).

10. J. S. Ross *et al.*, Rev. Sci. Instrum. **81**, 10D523 (2010).

11. S. C. Snyder *et al.*, Phys. Rev. E **50**, 519 (1994).

12. J. Zheng, C. X. Yu, and Z. J. Zheng, Phys. Plasmas **4**, 2736 (1997).

Measuring Heat Flux from Collective Thomson Scattering with Non-Maxwellian Distribution Functions

R. J. Henchen,[1,2] M. Sherlock,[3] W. Rozmus,[4] J. Katz,[1] P. E. Masson-Laborde,[5] D. Cao,[1] J. P. Palastro,[1] and D. H. Froula[1,6]

[1]Laboratory for Laser Energetics, University of Rochester
[2]Department of Mechanical Engineering, University of Rochester
[3]Lawrence Livermore National Laboratory
[4]Department of Physics, University of Alberta, Canada
[5]Commissariat á l'energie atomique et aux énergies, France
[6]Department of Physics and Astronomy, University of Rochester

Thermal transport in plasmas is of particular interest to inertial confinement fusion, where a correct description of heat flux is crucial to modeling the absorption of incident laser beams used to implode fusion targets. Electron thermal transport is a fundamental process in plasma physics that becomes difficult to calculate since even in the most modest conditions, classical theory tends to break down. Extensive work has attempted to determine the nonlocal heat flux that is responsible for transporting thermal energy over large distances but quantitative experiments are required.

In laser-produced plasmas, where energy is primarily deposited locally at the critical density, temperature gradients inherently drive non-Maxwellian electron distribution functions as electrons carry the heat down the temperature gradient and slower electrons carry a return current up the temperature gradient to maintain neutrality. A consequence of heat flux, and the ensuing distortion of the distribution function, is to change the partition of energy between the thermal electrons and the thermal fluctuations. This has a particularly large effect on the amplitude of the fluctuations that have phase velocities near the velocity of the heat-carrying electrons. The heat flux modifies both the number of electrons and the slope of the distribution function, which directly changes the local Landau damping of ion-acoustic and Langmuir waves.

Collective Thomson scattering measures the fluctuation spectrum, and when probing electron plasma fluctuations with phase velocities in the region of heat-carrying electrons, the spectrum can be used to determine the heat flux.[1] The first-order effect of the electron distribution function on the Thomson-scattering spectrum can be observed in the dependence of the peak power scattered into the electron plasma wave feature,

$$P_{\text{peak}} \propto \frac{f_{\text{e}}(v)}{\left[\mathrm{d}f_{\text{e}}(v) \big/ \mathrm{d}v \right]^2} \Bigg|_{v = v_\phi},\tag{1}$$

where $f_{\text{e}}(v)$ is the electron distribution function and $\mathrm{d}f_{\text{e}}(v)$ is elevated at the phase velocity v_ϕ.

We present the direct measurement of heat flux using collective Thomson scattering from a laser-produced coronal plasma. The heat flux was measured in two ways that were used to experimentally determine the validity of classical thermal transport. The first measurement of heat flux used the classically derived non-Maxwellian electron distribution functions to reproduce the electron plasma wave Thomson-scattering spectra, while the second method used the measured plasma conditions to calculate the

classical heat flux. Figure 1(a) shows the experimental setup, where six 351-nm laser beams created a blowoff aluminum plasma. A 526-nm Thomson-scattering probe beam was used to scatter light from five locations in the coronal plasma. At each location the complete collective Thomson-scattering spectrum was measured and used to determine the electron temperature (T_e) and density (n_e) profiles. These plasma conditions were used to calculate the classical heat flux ($q = -\kappa \nabla T_e$), where κ is the classical thermal conductivity that depends only on the local electron temperature and density.

E24097JR
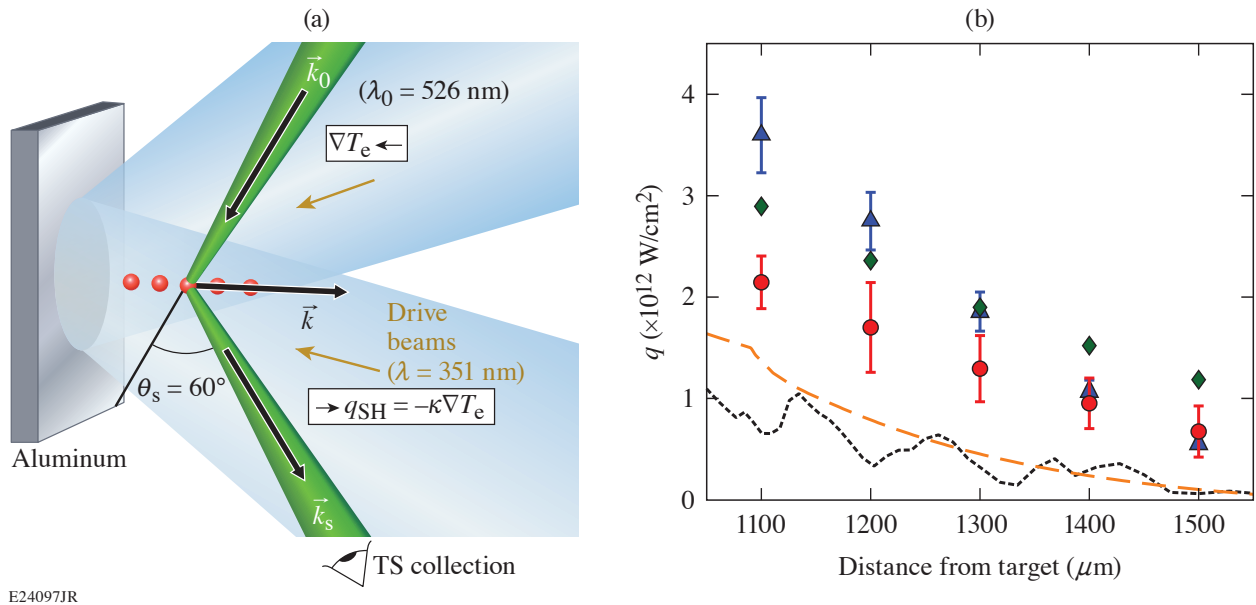
Figure 1

(a) The experimental setup is shown where six beams (blue) produced a blowoff plasma from a planar target (gray). A Thomson-scattering probe beam (green) with wave vector $\vec{k}_0$ was oriented relative to the target to probe plasma waves $(\vec{k})$ along the central axis, where the temperature gradient is the largest. Five Thomson-scattering locations (red) along the target normal provided measurements of plasma parameter profiles (T_e, n_e, ∇T_e). (b) Heat-flux measurements (red circles) are shown at $t = 1.5$ ns after the start of the $\lambda_{3\omega}$ beams as a function of distance from the initial target surface. Classical heat-flux values determined from the measured plasma parameters (blue triangles) are included along with results from full-scale SNB (black dotted line) and *FLASH* (orange dashed line) simulations in addition to 1-D SNB calculations using the measured plasma profiles (green diamonds).

Figure 1(b) shows that in regions where the electron–ion mean free path is small compared to the temperature gradients $\left(\lambda_{ei}/\left|L_T\right| < 7 \times 10^{-3}\right)$, the two heat-flux measurements agreed (red and blue symbols), which demonstrates the validity of the classical Spitzer–Härm theory. For larger relative temperature gradients (i.e., closer to the intial target surface, $<1500\ \mu$m), the flux determined from non-Maxwellian electron distribution functions derived from classical theory was not consistent with the heat flux determined from measurements of the plasma conditions. This experimentally demonstrated that in plasmas with steep relative temperature gradients, the classical thermal transport theory is not valid. To determine the flux in this region, non-Maxwellian electron distribution functions consistent with nonlocal thermal transport were used to fit the Thomson-scattering spectra. At the steepest relative temperature gradient (1100 μm), the nonlocal heat-flux measurements were up to 1.5× smaller than the flux determined from classical theory. One-dimensional calculations using the Schurtz–Nicolaï–Busquet (SNB) model (diamonds), initiated with the measured plasma conditions, show a reduced heat flux compared with the classical theory but overestimated the flux at all locations compared with the nonlocal measurements.

1. R. J. Henchen *et al.*, Phys. Rev. Lett. **121**, 125001 (2018).

Status of Free-Energy Representations
for Homogeneous Electron Gas

V. V. Karasiev,[1] S. B. Trickey,[2] and J. W. Dufty[3]

[1]Laboratory for Laser Energetics, University of Rochester
[2]Quantum Theory Project, Departments of Physics and Chemistry, University of Florida
[3]Department of Physics, University of Florida

The homogeneous electron gas (HEG) is a well-studied system at zero temperature as a model for electrons in solids and as a model for fully ionized plasmas at temperatures T well above the Fermi temperature T_F. For a long while far less information was available from either theory or simulation at intermediate temperatures and densities, in large part due to lack of motivation. That has changed recently with growing experimental access to observations on states of matter in this domain. Such access is driving growth in the fields of warm dense matter (WDM) and high-energy-density physics. Accordingly, the first quantum Monte Carlo (QMC) simulations for the HEG in this domain were reported only six years ago.[1] Subsequently Dornheim *et al.*[2] produced improved QMC results for temperatures $0.5 \leq t = T/T_F \leq 8$ over a wide density range (Wigner–Seitz radii $0.1 \leq r_s \leq 10$). They also developed and used significantly improved finite-size corrections. Those data currently seem to be the most-accurate finite-temperature HEG results available.

For practical purposes a representation interpolating such QMC data and extrapolating it via known theoretical limits is needed. The target is an equation of state for the complete thermodynamics of the HEG, provided by the free energy as a function of r_s and t. A rather complete review of the recent simulations and their representations is given in Ref. 3. As noted there, the program for constructing a free energy from theoretical limits and simulation data was originally presented and used in Ref. 4, which presented a representation, "KSDT" (Karasiev–Sjostrom–Dufty–Trickey), based on the original data of Ref. 1 and the $T = 0$ data of Ref. 5. Subsequently, Groth *et al.*[6] used the KSDT approach and protocol to reparametrize the exchange-correlation (XC) contribution to the free energy against the finite-size–corrected QMC results of Ref. 2 along with the Singwi–Tosi–Land–Sjölander (STLS) approximation[7] for low-t ($t < 0.5$) behavior and for connection with the $T = 0$ data of Ref. 5. The resulting representation is denoted as "GDB" (Groth–Dornheim–Bonitz). Essentially simultaneously, a small error in the use of zero-temperature data for KSDT was detected and repaired to yield the corrected KSDT representation "corrKSDT" (see Supplemental Material for Ref. 8).

This work achieved three objectives: The first is based on recent simulation studies of the free energy for the HEG in a domain of the (r_s,t) plane not previously explored. The data combined with thermodynamic consistency and known theoretical limits led to three global representations of the free energy, corrKSDT, its direct antecedent KSDT, and GDB. The equivalence of these for reproducing the simulation data for $f(r_s,t)$ was demonstrated. Furthermore, the equivalence of corrKSDT and GDB for the XC component alone was illustrated, although the original KSDT representation has some inconsequential small errors for $f_{xc}(r_s,t)$ (Ref. 2). Figure 1 demonstrates that the two fits match the available QMC data indistinguishably for $t \geq 0.5$ and are in perfect agreement for $t < 0.5$.

The second objective was to draw attention to the fact that, in spite of these very accurate representations for $f(r_s,t)$, thermodynamic properties obtained by temperature derivatives exhibit striking anomalies. Those occur outside the domain for which simulation data are available and are properties of the extrapolation/interpolation provided by the fitting procedure. This was discussed and it was noted that the entropy per particle (first-order temperature derivative) can become negative for large r_s and small t. For the corrKSDT and GDB representations, this corresponds to state conditions beyond the expected spin polarization
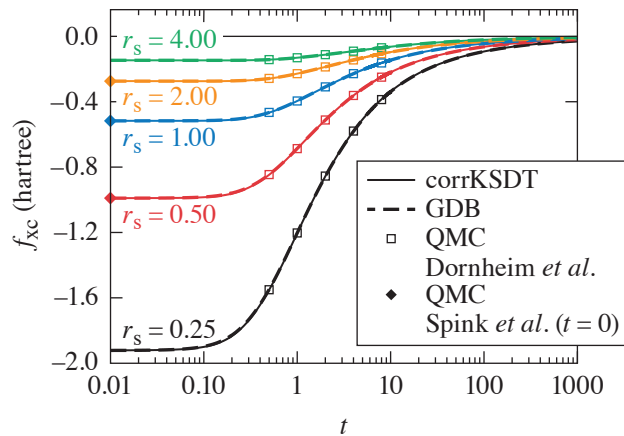
TC14705JR

Figure 1
Comparison between f_{xc} values from the corrKSDT and GDB parametrizations and QMC data from Ref. 9 for the unpolarized HEG at $r_s = 0.25$, 0.5, 1, 2, and 4. The ground-state limit ($t = 0$, Ref. 5) QMC values also are shown.

transition and therefore outside the domain of their intended application. A second more-serious anomaly occurs for the specific heat c_V (second derivative with respect to T). In that case, all of the representations predict unusual oscillatory behavior for t between 0.1 and 1 and $r_s \geq 10$. Figure 2 shows c_V calculated for the noninteracting and interacting HEG from the corrKSDT and GDB representations. As anticipated, the specific heat curves from the two parametrizations are practically identical, a consequence of the small procedural differences of parameter fitting in the two. Even though the oscillatory behavior might be an indication of some kind of critical point, it is far more plausible that it is an artifact introduced by the QMC data of Ref. 2 and the way that corrKSDT and GDB represent those data. Without any theoretical or simulation guidance, this must be seen as a possible flaw in the representation function.
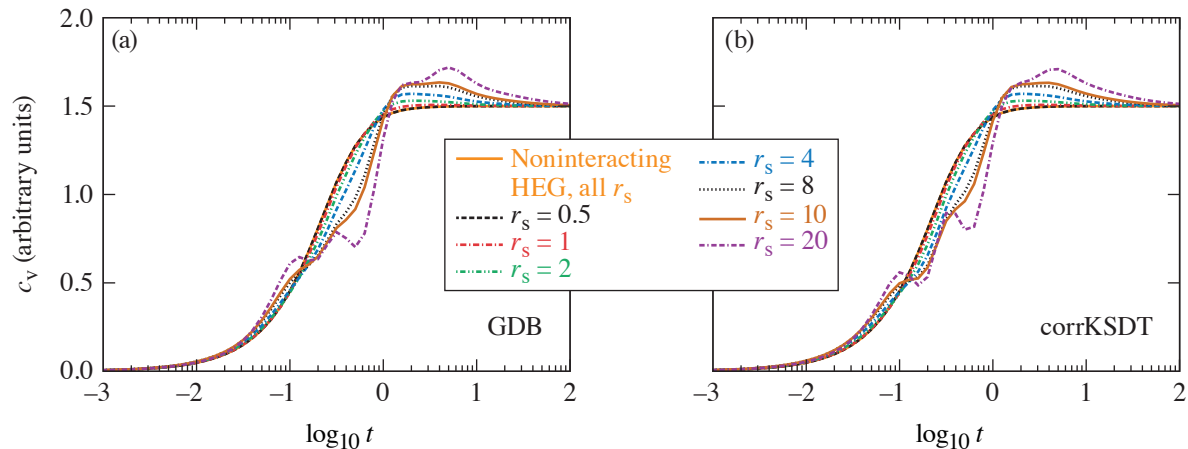
TC14706JR

Figure 2
Electron specific heat c_V for the noninteracting and interacting HEG calculated with (a) GDB and (b) corrKSDT parametrizations.

The third objective was to verify the use of the three representations as essentially interchangeable for use as local density approximation (LDA) functionals in free-energy DFT calculations and in more-refined f_{xc} approximations. It is helpful to note the parallel with most $T = 0$ DFT calculations. They are based in a similar way on ground-state HEG simulations. Generalized gradient approximations, for example, have the LDA (consequently the HEG) as a limiting case. Therefore, the extensions discussed here to the entire (r_s, t) plane constitute an essential prerequisite for addressing WDM in an accurate, practical fashion. A first example of a nonempirical semilocal free-energy density functional for matter under extreme conditions, built on the LDA representations here, was noted.[8]

1. E. W. Brown *et al.*, Phys. Rev. Lett. **110**, 146405 (2013).

2. T. Dornheim *et al.*, Phys. Rev. Lett. **117**, 156403 (2016).

3. T. Dornheim, S. Groth, and M. Bonitz, Phys. Rep. **744**, 1 (2018).

4. V. V. Karasiev *et al.*, Phys. Rev. Lett. **112**, 076403 (2014).

5. G. G. Spink, R. J. Needs, and N. D. Drummond, Phys. Rev. B **88**, 085121 (2013).

6. S. Groth *et al.*, Phys. Rev. Lett. **119**, 135001 (2017).

7. S. Tanaka and S. Ichimaru, J. Phys. Soc. Jpn. **55**, 2278 (1986).

8. V. V. Karasiev, J. W. Dufty, and S. B. Trickey, Phys. Rev. Lett. **120**, 076401 (2018).

9. T. Schoof *et al.*, Phys. Rev. Lett. **115**, 130402 (2015).

A Ten-Inch-Manipulator–Based Fast-Electron Spectrometer with Multiple Viewing Angles

H. Habara,[1] T. Iwawaki,[1] K. A. Tanaka,[1,†] T. Gong,[1,‡] M. S. Wei,[2] S. T. Ivancic,[2] W. Theobald,[2] C. M. Krauland,[3] S. Zhang,[3] and G. Fiksel[4]

[1]Graduate School of Engineering, Osaka University, Japan
[2]Laboratory for Laser Energetics, University of Rochester
[3]Department of Mechanical and Aerospace Engineering, University of California at San Diego
[4]Center for Ultrafast Optical Science, University of Michigan
[†]Currently at Extreme Light Infrastructure: Nuclear Physics, Romania
[‡]Currently at Research Center of Laser Fusion, China Academy of Engineering Physics, People's Republic of China

The measurement of angularly resolved energy distributions of MeV electrons is important for gaining a better understanding of the interaction of ultra-intense laser pulses with plasma, especially for fast-ignition laser-fusion research. It is also crucial when evaluating the production of suprathermal (several tens of keV) electrons through laser–plasma instabilities in conventional hot-spot–ignition and shock-ignition research. For these purposes, we developed a ten-inch-manipulator (TIM)–based multichannel electron spectrometer—the Osaka University electron spectrometer (OU-ESM)—that combines angular resolution with high-energy resolution. The OU-ESM consists of five small electron spectrometers set at every 5°, with an energy range from ~40 keV to ~40 MeV. A low-magnetic-field option provides a higher spectral resolution for an energy range of up to ~5 MeV. This versatile diagnostic with a variable electron energy range can be deployed for experiments on the OMEGA and OMEGA EP Laser Systems.

The spectrometer uses permanent magnets in a Ni-coated yoke to disperse the electrons in energy. Assuming that the magnetic-flux density is constant, the electron motion is determined by the Larmor motion according to the electron's kinetic energy, given by

$$E = mc^2 \left[\sqrt{\left(\frac{l^2 + h^2}{2h}\right)^2 \left(\frac{eB}{mc}\right)^2 + 1} - 1 \right],$$ (1)

where l is the longitudinal position of the signal on the detector from the magnet entrance, h is the height between the electron incident axis and the detector plane, e is the electric charge, B is the magnetic flux density, m is the electron mass, and c is the speed of light in vacuum, respectively. Because fast electrons created by ultra-intense lasers have considerably large emission angles, a collimator is used to guarantee a parallel electron beam into the magnetic field. Consequently, the number of accelerated electrons, N, per solid angle and per energy is given by

$$\frac{dN^2}{d\Omega dE} = \frac{I_{IP}}{\Delta l \Delta \Omega} \frac{1}{S(E)\varphi} \frac{h}{ceBl} \sqrt{1 + \left(\frac{2h}{l^2 + h^2}\right)^2 \left(\frac{mc}{eB}\right)^2},$$ (2)

where I_{IP} is the signal intensity on the detector, Δl is the spatial resolution of the detector, $\Delta \Omega$ is the solid angle, $S(E)$ is the detector sensitivity, and φ is the fading rate of the signal.[1]

Although it is very important to observe the energy spectrum in different viewing angles, this usually requires multiple electron spectrometers at different port locations around the target chamber. Given that this option is severely restricted because of port availability and interference issues with other diagnostics and laser beams, we maximized the capability of this diagnostic by combining five mini spectrometers at different viewing angles into a module that fits in a single diagnostic shuttle system—the TIM. Figure 1(a) shows a photograph of the OU-ESM. The diagnostic can be inserted into the TIM's on both the OMEGA and the OMEGA EP target chambers. The pointer pin shown at the bottom of Fig. 1(a) is used to align the diagnostic to a given aiming location. Every spectrometer channel is then automatically pointed correctly to the aiming point within the mechanical tolerance. A 20-mm-thick tungsten heavy metal alloy block on the front face with 700-μm-diam holes in front of each magnet serves as a collimator. A large piece of imaging plate (IP) serves as a detector attached to the cover plate of the detector box. Figure 1(b) shows an example of raw data that were taken in a fast-ignition–relevant experiment when a short IR pulse channeled through a preformed, long-scale-length plasma.[2,3] The pre-plasma was formed by a 1-ns, low-intensity UV pulse. A high-intensity, 10-ps pulse ($\sim 1 \times 10^{19}$ W/cm^2) was injected into the long-scale-length plasma. Figure 1(c) shows the inferred electron spectra. An important feature of the system is that the strength of the magnet in each channel can be changed between 0.45 T (high-field operation) and 0.045 T (low-field operation). The detectable energy range in high-field operation is from $\sim$0.6 to $\sim$40 MeV in the inner channels, whereas energy ranges from $\sim$0.6 to $\sim$25 MeV in the side channels. In the low-field operation, the energy range is from $\sim$40 keV to $\sim$5 MeV in the inner channels and from $\sim$40 keV to $\sim$2.5 MeV in the side channels. The five horizontal lines in Fig. 1(b) correspond to the signals from CH1 (bottom) to CH5 (top). In this experiment, CH3 was located on the laser axis. Channel 2 and CH4 were operated in low-field mode, whereas CH1, CH3, and CH5 were in high-field mode.

(a) (b) (c) Shot 22900

E28262JR
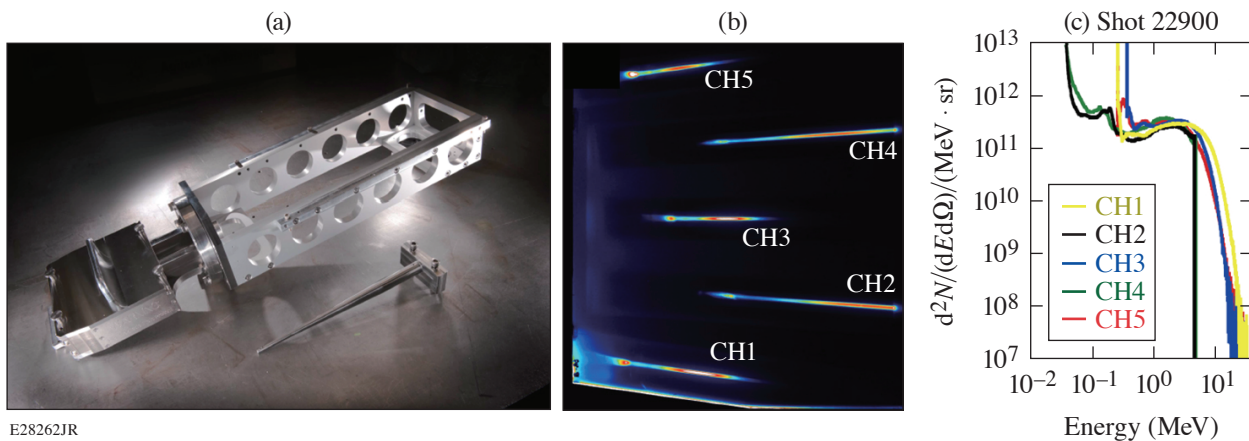
Figure 1
(a) Photograph of the OU-ESM, (b) raw data on an imaging plate, and (c) analyzed fast-electron energy spectra from an OMEGA EP experiment that demonstrated the channeling of an intense 10-ps IR laser pulse through a pre-plasma created by a 2-kJ, 1-ns UV pulse.

1. K. A. Tanaka *et al.*, Rev. Sci. Instrum. **76**, 013507 (2005).

2. L. Ceurvorst *et al.*, Phys. Rev. E **97**, 043208 (2018).

3. S. Ivancic *et al.*, Phys. Rev. E **91**, 051101(R) (2015).

Time-Resolved, Nonequilibrium Carrier and Coherent Acoustic Phonon Dynamics in (Cd,Mg)Te Single Crystals for Radiation Detectors

J. Serafini,[1,2] A. Hossain,[3] R. B. James,[3,4] S. B. Trivedi,[5] and R. Sobolewski[1,6,#]

[1]Department of Physics and Astronomy and Laboratory for Laser Energetics, University of Rochester
[2]Department of Microsystems Engineering, Rochester Institute of Technology
[3]Brookhaven National Laboratory
[4]Savannah River National Laboratory
[5]Brimrose Technology Corporation
[6]Department of Electrical and Computer Engineering, University of Rochester
[#]Also at the Institute of Electron Technology, Poland

Volume-type radiation detectors are devices that collect charged particles, such as electrons, produced by photon interaction with the detector material, typically a single crystal. In the case of highly energetic x-ray radiation photons, they interact with matter through three main mechanisms: the photoelectric effect, the Compton effect, and electron–positron pair production. The photoelectric effect is by far the most dominant effect among them because Compton-scattered photons, as well as high-energy gammas from electron–pair annihilations, typically escape from the detection volume and their energy cannot be collected. Photo-conductive devices are, in fact, the most popular solid-state radiation detectors since they can often operate at room temperature, cover the spectral range up to hard x rays and even γ rays, and are easy to design and fabricate.

There is a high demand for solid-state x-ray detectors in applications ranging from medical imaging to homeland security (portable screening units) and astrophysics. Currently, cadmium zinc telluride [(Cd,Zn)Te or CZT] is the accepted material of choice; however, because of its large Zn segregation constant, it has poor crystal-growth yield, making it costly to fabricate in large volumes.[1,2] Proposed alternatives to CZT are cadmium manganese telluride [(Cd,Mn)Te or CMnT] single crystals[3,4] and most recently developed cadmium magnesium telluride [(Cd,Mg)Te or CMgT] (Ref. 5). All of the above materials are ternary alloys that contain tellurium, which ensures their very high stopping power and 100% absorption efficiency for x-ray photons with energies up to above 100 keV (Ref. 4). However, CMgT also possesses all other necessary qualities for an optimal radiation detector, i.e., high density (5.83 g/cm^3), high electron effective mass (49.5), ultrahigh resistivity (~10^{10} Ω-cm), and a good electron mobility lifetime ($\mu\tau_e$) product (>10^{-4} cm^2/V) (Ref. 5). In addition, the CMgT "parent" crystals, CdTe and MgTe, exhibit very similar lattice constants, namely, 6.48 Å and 6.42 Å, respectively,[6] resulting in a high crystallinity yield of the CMgT material.

This summary focuses on the ultrafast optical properties of the latest member of the above-mentioned ternary materials, namely, the CMgT single crystal. We present comprehensive femtosecond pump–probe spectroscopy studies where we measure time-resolved carrier dynamics and, subsequently, analyze the data within a coupled rate-equation model, developed to reveal both the carrier recombination and trapping components of the relaxation process. In addition, we time-resolve long-lived coherent acoustic phonons (CAP's) in a manner similar to a method earlier implemented for CMnT crystals.[7]

In our experiments, we test CMgT crystals with optimal composition and ultrahigh resistivity for x-ray detection applications,[8] namely Cd$_{0.92}$Mg$_{0.08}$Te, and with two different dopants: indium (CMgT:In) and germanium (CMgT:Ge). In both cases, doping ensures that the resulting crystals exhibit ultrahigh resistivity; however, the used dopants act very differently. Indium doping is intended to simply compensate the native concentration of holes (CdTe-based crystals are naturally *p*-type semiconductors), while

Ge is a deep impurity, introduced to "pin down" the Fermi level at the middle of the band gap. The impurities obviously affect the crystalline quality of the resulting materials, negatively affecting the $\mu\tau_e$ product that needs to be as large as possible for a sensitive detector. Therefore, typically, the single crystals intended for x-ray detectors are annealed after their growth in order to improve their crystalline structure. In our work, we compare time-resolved dynamics of photoexcited carriers in CMgT:In and CMgT:Ge, both as-grown and annealed crystals, in order to determine what material exhibits the best transport properties, i.e., minimal trap concentration and the longest electron lifetime, required for the optimal photoelectric radiation detector.

To understand the physics of the nonequilibrium relaxation dynamics of photoexcited carriers in our CMgT crystals (see Fig. 1 as an example), we fitted our experimental probe-normalized, transient-reflectivity $\Delta R/R$ waveforms, measured in both one- and two-color setups, to the trapping and relaxation model that we developed and presented in Ref. 9. We note that in Fig. 1, as well as all other cases, the numerical total concentration of photoexcited carriers' dependence (solid red line) fit perfectly with the experimental $\Delta R/R$ transient (black circles). The initial fast relaxation time τ_1 is ascribed as the direct trapping of excited electrons, while the subsequent relatively much slower relaxation time τ_2 can be interpreted as the Shockley–Read–Hall recombination. The values of the fitting parameters, in the case of Fig. 1, are $\tau_1 = 0.21$ ps and $\tau_2 = 4.77$ ps. The subpicosecond value of τ_1 indicates that, in this sample, carrier trapping is the dominant mechanism of the photoresponse. The latter also explains the negative dip at the relaxation part of the $\Delta R/R$ signal. The value of τ_2 is also very short, showing that traps are also very effective in nonradiative electron-hole recombination. Therefore, our approach provides a detailed description of the physical processes governing both the carrier excitation and subsequent relaxation dynamics in our as-grown and annealed CMgT:In and CMgT:Ge samples.
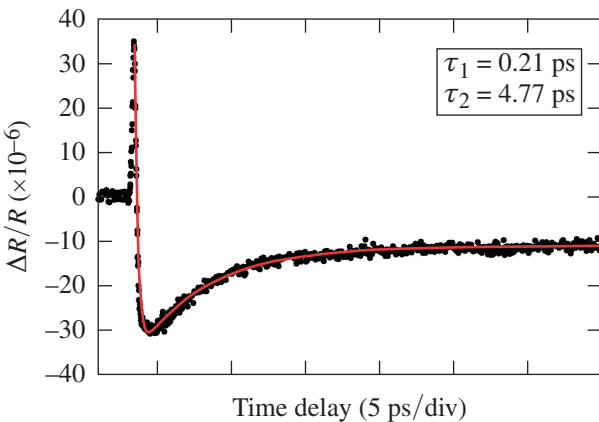
Figure 1

Normalized reflectivity transient change $\Delta R/R$ (black circles) measured in a one-color, pump–probe spectroscopy setup for an as-grown CMgT:In sample. The solid red line is the best fit to the trapping and relaxation model and the corresponding fitting parameters are listed in the inset.

E26356JR

During the course of our two-color pump–probe studies performed on both CMgT:In and CMgT:Ge samples, we consistently observed the presence of weak but very regular oscillations on the relaxation part of $\Delta R/R$ waveforms when traced in a time-delay range of the order of a nanosecond. These oscillations can be satisfactorily interpreted within the propagating strain-pulse model, introduced by Thomsen et al.[10] and Wu et al.[11] The high-energy and high-fluence femtosecond pump pulses incident on the crystal surface introduce electronic as well as thermal stress and generate a strain transient (lattice discontinuity) that propagates with a velocity of sound v_s into the sample at the direction orthogonal to the surface, locally altering its optical properties; namely, the refractive index of the crystal. The time-delayed probe beam penetrating the crystal is partially reflected from this traveling discontinuity and interferes with the part of the probe light reflected from the crystal surface, resulting in the regular oscillations observed on top of the $\Delta R/R$ photoresponse signal, interpreted as CAP's. CAP propagation was dispersionless with the constant propagation velocity corresponding to the speed of sound in our CMgT, (111) oriented crystal. The intrinsic lifetime of CAP's was estimated to be as long as 10 ns or more.

1. R. B. James *et al.*, in *Semiconductors for Room-Temperature Radiation Detector Applications*, Semiconductors and Semimetals, Vol. 43, edited by T. E. Schlesinger and R. B. James (Academic Press, San Diego, 1995), Chap. 9, pp. 336–383.

2. C. Szeles *et al.*, IEEE Trans. Nucl. Sci. **49**, 2535 (2002).

3. A. Mycielski *et al.*, J. Alloys Compd. **423**, 163 (2006).

4. A. S. Cross *et al.*, Nucl. Instrum. Methods Phys. Res. A **624**, 649 (2010).

5. A. Hossain *et al.*, J. Cryst. Growth **379**, 34 (2013).

6. J.-H. Yang *et al.*, Phys. Rev. B **79**, 245202 (2009).

7. D. Wang *et al.*, Appl. Phys. Lett. **90**, 211905 (2007).

8. J. E. Toney, T. E. Schlesinger, and R. B. James, Nucl. Instrum. Methods Phys. Res. A **428**, 14 (1999).

9. J. Serafini *et al.*, Semicond. Sci. Technol. **31**, 045006 (2016).

10. C. Thomsen *et al.*, Phys. Rev. B **34**, 4129 (1986).

11. S. Wu *et al.*, Phys. Rev. B **76**, 085210 (2007).

High-Efficiency, Large-Aperture Fifth-Harmonic Generation of 211-nm Pulses in Ammonium Dihydrogen Phosphate Crystals for Fusion Diagnostics

I. A. Begishev, M. Romanofsky, S. Carey, R. Chapman, G. Brent, M. J. Shoup III, J. D. Zuegel, and J. Bromage

Laboratory for Laser Energetics, University of Rochester

High-energy ultraviolet (UV) sources are required to probe hot dense plasmas from fusion experiments by using Thomson scattering resulting from the lower self-generated background from the plasma in the 180- to 230-nm spectral region.[1] The fifth-harmonic generation (5HG) of a neodymium laser with a 211-nm wavelength fits that window. Recently[2] we demonstrated 30%-efficient, joule-class fifth-harmonic conversion of 1053-nm pulses using a cesium lithium borate (CLBO) crystal, but larger crystals are necessary for increased UV energy. Also, the extremely hygroscopic property of CLBO crystals requires that they be kept under high (~120°C) temperature. Ammonium dihydrogen phosphate (ADP) crystals, which can be grown to much larger sizes, should be considered as an alternative way of generating a high-energy beam at 211 nm.

For cascade 5HG, however, ADP has a significant limitation: phase-matching conditions for sum–frequency generation are not met at room temperature. Noncritical phase-matching conditions could be reached by cooling ADP crystals to –70°C. This is not trivial, especially for large-aperture crystals, because a definite temperature must be strictly stabilized and maintained across the entire crystal. Any holder that keeps a crystal in the vacuum chamber and maintains a crystal temperature through thermal conductive contact provides some gradient of temperature through a crystal.

The most-effective way to stabilize an entire crystal under low temperature is a two-chamber cryostat, where the internal chamber keeps a crystal almost isolated from a holder but surrounded by 1 atm of helium gas. The internal chamber is held in the high-vacuum external chamber to minimize heating. The cross section of the designed and fabricated two-chamber cryostat is shown in Fig. 1. "Cold flow" travels down from the liquid nitrogen tank through two hollow cylinders to the internal chamber; it then reaches the $65 \times 65 \times 10$-mm ADP crystal through the helium. As soon as the temperature of the crystal (or the internal chamber wall, depending on which temperature sensor is chosen as the control) approaches a chosen set point temperature, the heaters on the wall of the lower cylinder begin working to maintain that temperature through a temperature stabilization loop. A high-performance cryogenic temperature controller is used to monitor and control temperature within the internal chamber to better than 0.01°C resolution. Each of the two heaters mounted on the cryostat is controlled by a proportional-integral-derivative feedback loop. The feedback continually adjusts the output power to the heaters in order to keep the chosen temperature constant. The system has high thermal mass and reaches a target temperature of 200 K in about 36 h.

This experiment is shown in Fig. 2. Some portion of the energy must be saved at the fundamental frequency (20% in an ideal-case plane wave without any type of

E28200JR
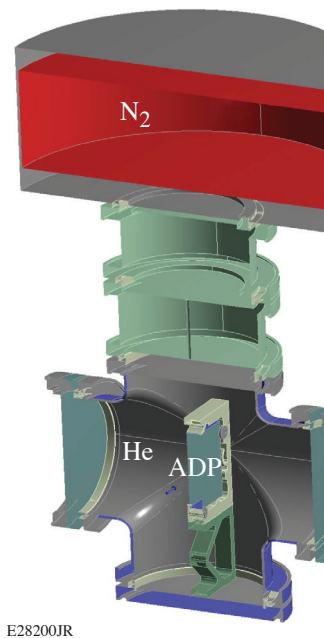
Figure 1
The cross section of the internal chamber, filled with helium (He), with the crystal (ADP) and liquid nitrogen tank (N$_2$).

absorption and Fresnel reflections), untouched through the first two crystals to mix with the 4ω beam. We have chosen the cascade $o_1 e_1 \longrightarrow e_2 : o_2 o_2 \longrightarrow e_4 : o_1 o_4 \longrightarrow e_5$, which allows the energy distribution between o and e waves to be changed by polarization rotation with a half-wave plate (HWP). The first frequency doubler was a Type-II deuterated potassium dihydrogen phosphate (DKDP) crystal ($30 \times 30 \times 27$ mm). A second frequency doubler, a Type-I KDP crystal ($30 \times 30 \times 15.5$ mm), was used to convert $2\omega \longrightarrow 4\omega$.

An Nd:YLF laser was optimized to produce square pulses with a flattop, square beam profile (1053 nm, 1 to 2.8 ns, 12×12 mm, ≤ 1.5 J, ≤ 5 Hz). The fused-silica prism separates the harmonic beams in space. The input and output beam energies were measured using identical cross-calibrated pyroelectric energy meters. All beam profiles were recorded.
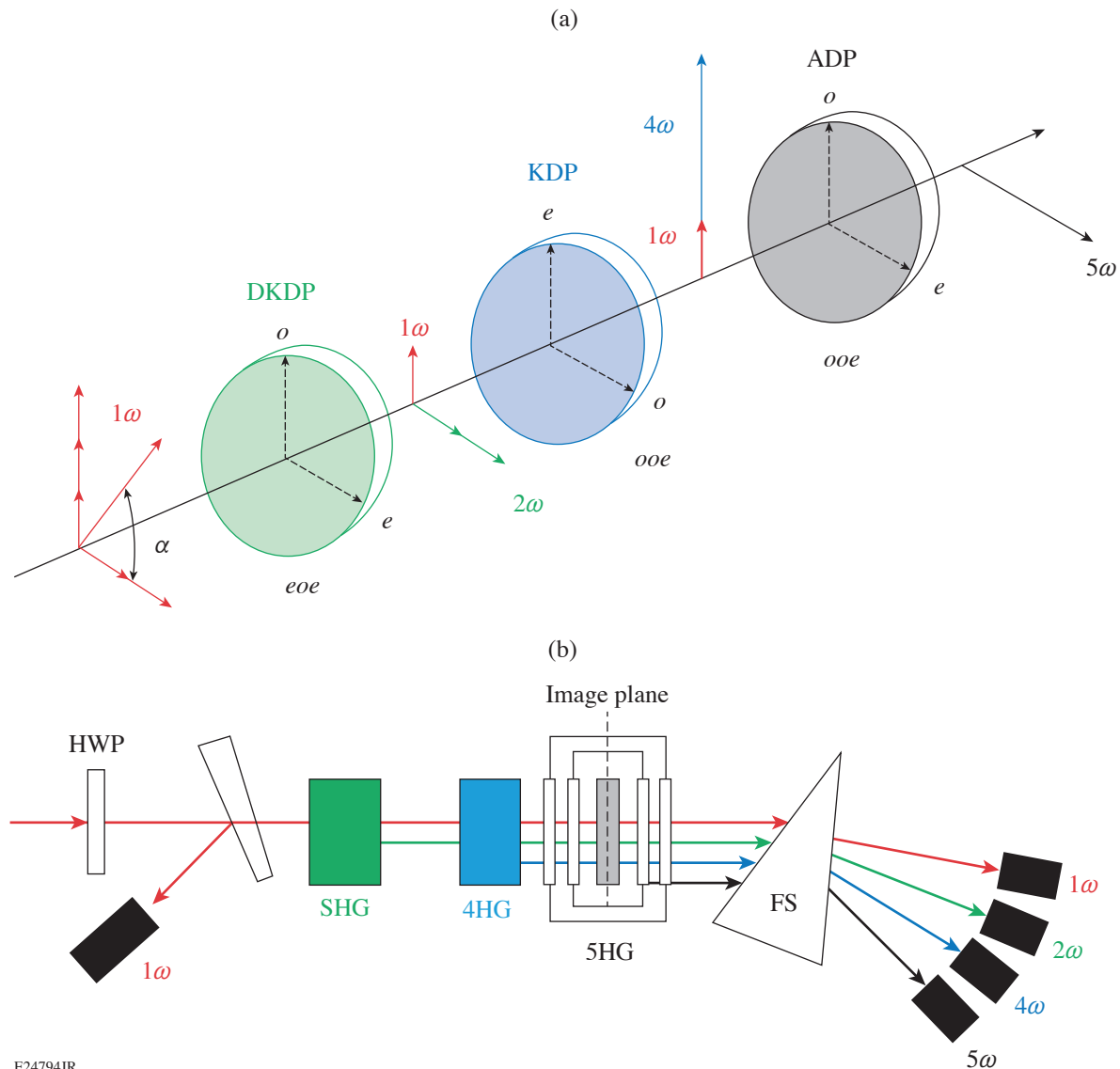
Figure 2
Experiment: (a) The orientation of the crystal axes and polarizations. The angle (α) of the 1ω polarization was set using a half-wave plate for optimal conversion, e: extraordinary, o: ordinary. (b) Setup. HWP: half-wave plate; SHG: second-harmonic generator; 4HG: fourth-harmonic generator; 5HG: fifth-harmonic generator; FS: fused-silica wedge.

Accurate tuning of the experimental parameters allowed for total conversion efficiency from the fundamental to the fifth harmonic, including surface losses and absorption, of 26% (Fig. 3). Temperature acceptance of 5HG is extremely narrow and less than 0.4 K (FWHM). Angular acceptance was measured at 200 K and is 8 mrad external (FWHM).
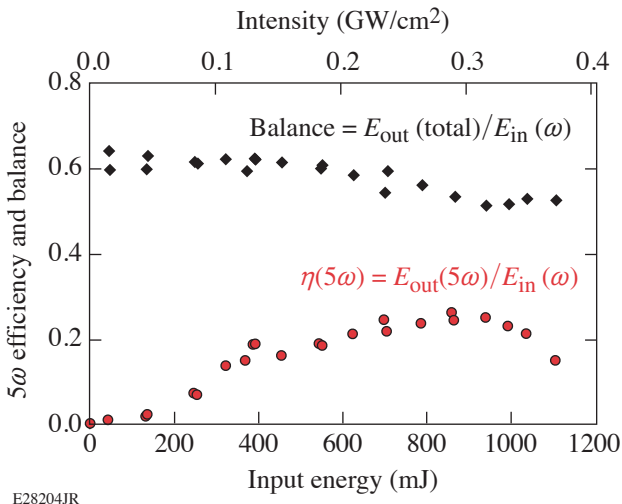
Figure 3
Fifth-harmonic efficiency and energy balance measured as a function of input-pulse energy and intensity.

E28204JR

1. J. S. Ross *et al.*, Rev. Sci. Instrum. **81**, 10D523 (2010).

2. I. A. Begishev *et al.*, Opt. Lett. **43**, 2462 (2018).

Interaction of Short Laser Pulses with Model Contamination Microparticles on a High Reflector

K. R. P. Kafka and S. G. Demos

Laboratory for Laser Energetics, University of Rochester

Contamination in the optical components of large-aperture laser systems is a well-known problem originating from the handling, installation, and operational environment of these large components. The main problems associated with contamination particles are that they can facilitate laser-induced damage (LID) during operation of the system by creating (a) localized absorption and damage of the host optic and (b) intensification (hot spots) of the propagating beam, giving rise to damage in downstream optical components. Previous studies on this issue have focused on identifying the origin of contamination[1] and understanding the interaction of nanosecond laser pulses with the contamination particles.[2,3] These studies have highlighted that contamination can originate from various sources (including ejected debris from LID of adjacent parts, target materials, and the optics themselves) and therefore can involve various types of materials. Depending on the type of contamination particle (metal, transparent, etc.), its interaction with the laser pulse varies and can be characterized by three main effects: (1) particle removal, (2) secondary contamination of the host surface by fragments of the original contamination particle, and (3) LID of the host surface. Particle removal or ejection is often desirable (frequently referred to as "laser cleaning"[4]), but LID and secondary contamination degrade the performance of the optic.

The effectiveness of contamination particles to accelerate LID in optical components in the short-pulse (picosecond to femtosecond) regime has so far remained uninvestigated. Furthermore, direct translation of the knowledge attained for nanosecond-pulse systems is not warranted since short-pulse systems typically employ reflective optical elements and operate at higher laser peak intensities by many orders of magnitude. This work investigates the interaction of 10-ps and 0.6-ps laser pulses with microparticles located on the surface of a multilayer dielectric mirror in order to understand and assess the risk of contamination-induced damage in short-pulse laser systems. Irradiation with one laser pulse caused particles to eject from the surface with an onset fluence in the range 5× to 100× below the particle-free, laser-induced damage threshold (LIDT) of the mirror. Morphological analysis showed, however, that the ejection process always generated ablation craters and/or secondary contamination, both of which can degrade the performance of the optic during subsequent pulses. Ejection and damage mechanisms are discussed for each particle type.

Four different particle materials (one metal, one glass, and two polymers) were used as representative contaminants in this experiment. All four species have similar ≈40-μm diameters, while three are spherical in shape. Although contaminant particles in an actual laser system would have a broad distribution of sizes and irregular shapes, these controlled variables of size and shape enable one to more directly compare and contrast the mechanisms and resulting surface modifications. The particles were used to intentionally contaminate 2-in.-diam commercially available multilayer dielectric mirrors that exhibit high reflection at our 1053-nm laser wavelength at angles of incidence from 0° to 45°.

A dry powder of particles was dispersed onto the mirror sample. The sample was then placed in an experimental setup for short-pulse laser irradiation of individual particles. Laser pulse durations of 0.6 or 10 ps were selected for this work. Beam profile and energy were recorded for each pulse to measure the beam-normal peak fluence of the 300-μm-diam (e^{-2}) Gaussian beam. Isolated contaminant particles were positioned to within 20 μm of the laser peak location and then irradiated by a single pulse. Subsequently, the morphologies of the irradiated sites were analyzed.

The fluences of median (50% probability) ejection (F_E) and median LID (F_{th}), displayed in Fig. 1, are organized by contaminant particle type. Noting the logarithmic scale, these data show that the onset of particle ejection always occurs at fluences significantly lower (in the range 1% to 20%) than F_0, the LIDT of the pristine (noncontaminated) mirror. The ejection fluence of the glass and steel did not vary significantly with pulse duration, whereas each of the two polymers showed a factor of 3 between F_E at the two pulse durations.
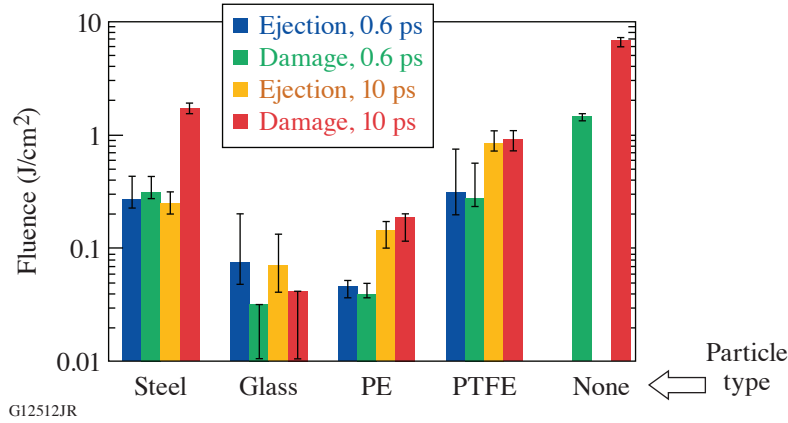
Figure 1
Median ejection and LID fluences. Error bars show the observed range from 0% to 100% probability, except for glass, where all tested fluences caused LID and a large lower bound was artificially added.

The morphological data and analysis for each of the eight tests (two pulse durations, four materials) were subsequently analyzed. Figure 2 displays the subset of this data set that shows the morphologies generated with stainless steel particles. These images show three representative laser fluences: (1) below, (2) just above, and (3) well above the particle ejection fluence. Slightly below the F_E of steel [Figs. 2(a) and 2(d)], a large number of submicrometer particles are observed on the mirror without ejection of the main particle. As fluence is increased to F_E [Figs. 2(b) and 2(e)], the main particle is ejected. This ejection was measured to occur at the same fluence for both pulse durations, consistent with the linear absorption (not dependent on intensity) of metals such as steel. At higher fluences [Figs. 2(c) and 2(f)], in addition to surface contamination by microparticles, LID is observed in sickle shapes on the laser-incident side. This suggests the formation of an interference pattern (from the directly incident beam and the beam reflected from the particle) exceeding the onset of damage initiation, especially exemplified in the 0.6-ps interaction. Under exposure to 10-ps pulses, a film of secondary contamination is observed to form [in Fig. 2(c)]. These observations together may suggest that 0.6-ps interactions bring a greater risk of LID, but 10-ps interactions bring a greater risk of secondary contamination.
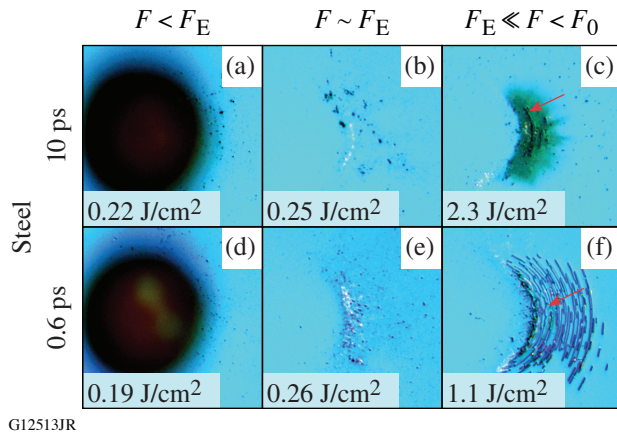
Figure 2
Optical microscopy of one-pulse–irradiated steel particle sites, organized by row (pulse duration) and column (relative fluence). Red arrows indicate ablation of the mirror. The laser is incident from the right at a 45° angle of incidence and s polarization.

Although all particle ejections left a residue of particles, films, and/or coating ablation at fluences far below the pristine LIDT, future work seeks to employ this knowledge to develop protocols of laser cleaning for optics in short-pulse, high-powered laser systems and could help devise self-cleaning protocols using the laser itself at lower operating fluences.

1. J. Bude *et al.*, Opt. Express **25**, 11,414 (2017).

2. M. J. Matthews *et al.*, J. Opt. Soc. Am. B **30**, 3233 (2013).

3. S. G. Demos *et al.*, Opt. Express **24**, 7792 (2016).

4. W. Zapka, W. Ziemlich, and A. C. Tam, Appl. Phys. Lett. **58**, 2217 (1991).
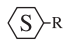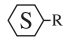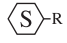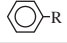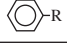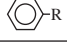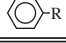
Evaluation of Laser-Induced–Damage Threshold in Saturated and Unsaturated Nematic Liquid Crystals Between 600 fs and 1.5 ns at 1053 nm
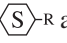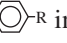
T. Z. Kosc, A. A. Kozlov, S. Papernov, K. R. P. Kafka, S. G. Demos, and K. L. Marshall

Laboratory for Laser Energetics, University of Rochester

A wide-ranging series of liquid crystal (LC) materials, which included compounds with saturated (cyclohexane) and unsaturated (benzene) carbon rings (Table I), were selected to explore the effect of varying degrees of π-electron delocalization and electron density on their laser-induced–damage threshold (LIDT). This work provides baseline measurements on the damage threshold of LC's as a function of their chemical structure, and it extends the currently limited available knowledge at subnanosecond pulse lengths. This information provides insight into the damage-initiation mechanisms in LC's and guidance for the possible implementation of future applications in high-power and/or peak intensity systems. Furthermore, this work can provide insight into the design of new materials such as polymer and glassy LC materials.

Table I: Nematic liquid crystals used in this study.

		Name	Supplier	Absorption Edge
$\langle S \rangle$-R		1550C	Dabrowski[^]	294 nm
$\langle S \rangle$-R		MLC-2037	Merck	306 nm
$\langle S \rangle$-R $\langle \bigcirc \rangle$-R		ZLI-1646	Merck	324 nm
$\langle \bigcirc \rangle$-R		PPMeOB/PPPOB	LLE[*]	345 nm
$\langle \bigcirc \rangle$-R		5CB	EMB	377 nm
$\langle \bigcirc \rangle$-R		E7	EMB	385 nm

Materials are designated as saturated $\langle S \rangle$-R and unsaturated $\langle \bigcirc \rangle$-R in the first column. Note that ZLI-1646 has a mixture of compound types. Transmission measurements were performed on a Perkin Elmer Lambda-900 spectrophotometer. LC materials were in the isotropic state during measurement. Here, the absorption edge is defined at $T = 98\%$.
[^]Isothiocyanate compound synthesized by M. Dabrowski, University of Warsaw.
[*]A 60/40 mixture of two phenyl benzoate ester compounds used on the OMEGA laser and synthesized at LLE.

Both 1-on-1 (single shot per test site) and *N*-on-1 (up to ten shots at 0.1 Hz, with the fluence ramped until damage occurs) damage testing were performed to determine the corresponding LIDT. Because the LC mesophase is fluid, a test site is considered damaged upon any visual change, as observed with an *in-situ* microscope system. The difference between pre-exposure and post-

exposure images is used to identify such changes. Damage-induced changes (tiny spot or bubble-like features) were observed as a change in scattered light in a micron-scale area and typically redissolved or migrated on a time scale dependent on laser fluence and fluid viscosity. The number density and size of these features increased with increasing fluence above the damage threshold. Additional details on sample preparation and testing protocol are found in Ref. 1.

Damage-threshold data were acquired at six pulse lengths (τ): 600 fs, 2.5 ps, 10 ps, 50 ps, 100 ps, and 1.5 ns at 1053 nm. Both the 1-on-1 and N-on-1 LIDT values are plotted in Fig. 1 as a function of each material's UV-absorption edge. Brackets identify the saturated, unsaturated, and mixed materials. In this study, data for saturated and unsaturated materials are fairly easily differentiated, and the partially saturated material behaves more like a fully saturated material (at least under 1053-nm irradiation). Damage thresholds of three common LC materials (E7, 5CB, and ZLI-1646), which were reported in 1988 (using nanosecond laser pulses at 1053 nm) (Ref. 2), were remeasured and found to be higher. This increase is attributed to significant improvements in the chemical purity of commercial LC compounds. Early measurements of the conjugated compound 5CB and its saturated analog ZLI-S-1185 (Ref. 3) are extended in the present work by exploring additional materials and pulse durations from subpicosecond to nanosecond. Of special significance are the data at 1.5 ns, where the LIDT values of saturated LC's approach those of bare fused silica.[4]
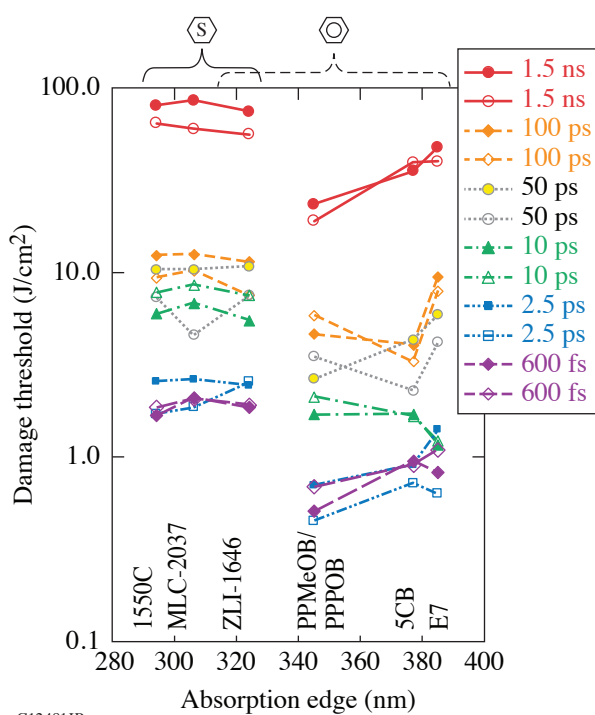
Figure 1

The 1-on-1 (open symbols) and N-on-1 (closed symbols) damage thresholds plotted as a function of the UV absorption edge. Materials with completely saturated or mostly saturated carbon rings have absorption edges <330 nm, with correspondingly higher damage thresholds.

G12481JR

The N-on-1 LIDT results exhibit a power dependence on the pulse length τ^x where $x \sim 0.5$, as shown in Fig. 2. A similar pulse-length dependence is observed in both dielectrics[4] and biological materials,[5] although in both cases the $\tau^{0.5}$ dependence extends only into the range of tens of picoseconds. This pulse-length dependence is attributed to thermal diffusion effects that govern the damage-initiation process, especially that of defects or defect states, which leads to free electrons and ionization of the material. In the range of tens of picoseconds, multiphoton ionization starts to contribute to electron production, and in the subpicosecond range, multiphoton ionization becomes the dominant process. At this time, we consider the fact that LC damage thresholds at pulse lengths <50 ps still follow the $\tau^{0.5}$ trend reasonably well as coincidental.
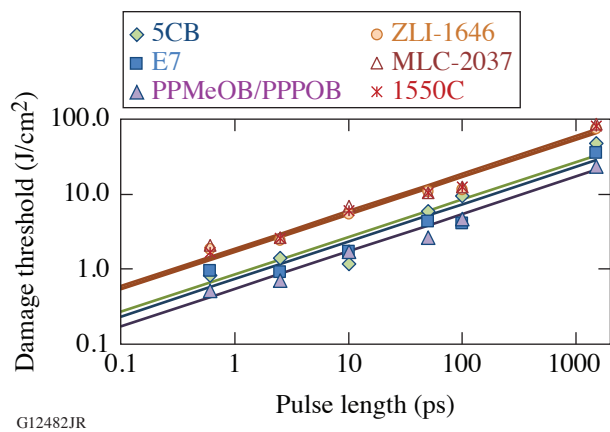
Figure 2
N-on-1 LIDT values for saturated and unsaturated LC materials are shown as a function of pulse length. A fit based on $\tau^{0.5}$ is shown for each material. R^2 values range between 0.91 (E7) and 0.97 (PPMeOB/PPPOB, 1550C, and ZLI-1646).

The absorption mechanisms, which lead to laser-induced damage, are largely dependent on the electronic structure of the material, intrinsic (LC orientation and domain boundaries) and extrinsic (impurities, substrate defects or inclusions) defects, and the laser parameters. The electronic structure in LC materials is generally known, involving a singlet ground state (S0) and excited singlet (S1, S2,…Sn) and triplet states.[6,7] The absorption spectra measurements suggest that, under 1053-nm laser irradiation, the unsaturated materials require three-photon absorption for the S0 $\longrightarrow$ S1 transition, while the saturated materials require four-photon absorption. This difference in the order of the absorption process required to generate excited-state electrons is clearly captured by the difference in the damage threshold between the two types of materials, where the saturated materials have 2× to 3× higher damage threshold across all pulse lengths tested.

This research has reported damage-threshold fluences for a series of saturated and unsaturated nematic LC materials for pulse lengths between 600 fs and 1.5 ns at 1053 nm. Saturated materials always have higher damage resistance, although the pulse-length–dependent behavior varies somewhat for the two different types of material. Damage mechanisms are still under investigation, but current results point toward the presence of both multiphoton absorption and excited-state absorption.

1. T. Z. Kosc *et al.*, Proc. SPIE **10447**, 104471G (2017).

2. S. D. Jacobs *et al.*, J. Opt. Soc. Am. B **5**, 1962 (1988).

3. M. Guardalben *et al.*, in *Laser Induced Damage in Optical Materials: 1988*, Natl. Inst. Stand. Technol. (U.S.), Spec. Publ. 775 (U.S. Government Printing Office, Washington, DC, 1989), pp. 462–469.

4. B. C. Stuart *et al.*, Phys. Rev. B **53**, 1749 (1996).

5. A. Oraevsky *et al.*, IEEE J. Sel. Top. Quantum Electron. **2**, 801 (1997).

6. R. Sander, V. Herrmann, and R. Menzel, J. Chem. Phys. **104**, 4390 (1996).

7. G. E. O'Keefe *et al.*, Liq. Cryst. **21**, 225 (1996).

Mechanisms Governing Laser-Induced Damage in Absorbing Glasses Under Exposure to Nanosecond Pulses

S. G. Demos,[1] B. N. Hoffman,[1] C. W. Carr,[2] D. A. Cross,[2] R. A. Negres,[2] and J. D. Bude[2]

[1]Laboratory for Laser Energetics, University of Rochester
[2]Lawrence Livermore National Laboratory

Significant progress has been made during the past 15 years in understanding the mechanisms of laser-induced damage in transparent optical materials and mirrors. Above a threshold laser fluence, defect structures initiate plasma formation that leads to exposure of the material to high localized pressures followed by an explosive boiling process that involves ejection of superheated material, the launching of a shock wave, and stresses that result in mechanical damage of the surrounding "cold" material.[1] The dynamics and ensuing relaxation pathway are typically manifested as a microscopic crater on the surface or a microscopic void formed in the bulk of the material, depending on the location of damage initiation.

In contrast, laser-induced damage in absorbing dielectric materials under nanosecond laser pulses has received far less attention. Such absorbing materials are typically used as optical filters to attenuate the laser light for various applications including laser safety, sensor protection, and attenuation of stray beams in high-power laser systems such as at the National Ignition Facility. In addition, nominally transparent optical materials (such as glasses) operating in a high-radiation environment can develop color centers, thereby becoming absorbing at the operational wavelength.

Early work suggested that nonlinear absorption plays an important part in laser damage to absorbing optical glasses[2] and that damage occurred at either the surface or internally.[3] Past damage-morphology studies of such glasses under relevant excitation conditions indicated that material modifications are manifested with a typical "melted-surface" morphology[4] but such observations were often observed at fluences where the calculated surface temperature reached during the laser pulse was well below the melting point of the glass. Other reports suggested that the damage morphology changes as a function of the laser beam size and repetition rate.[5] These previous results indicate that key issues regarding laser-induced damage in absorbing glasses remain unclear.

The current study was designed to investigate the dominant mechanisms of laser-induced damage in absorbing optical materials under irradiation with 355-nm pulses having a temporal duration of the order of a nanosecond. A wide array of diagnostics tools was employed to enable one to monitor beam propagation inside the material, quantifying changes in the optical properties of the material, and capturing time-resolved transient material modifications with adequate spatial and temporal resolution. The results suggest that, in addition to linear absorption, excited-state absorption is a key mechanism contributing to enhanced energy deposition. In addition, there are two competing damage-initiation mechanisms: the first through self-focusing activated by a transient, fluence-dependent change of the refractive index; the second through melting of the material as a result of the increase of its temperature.

Figure 1(a) demonstrates a typical example of the first observed damage mechanism, showing the beam intensity profiles along the center of the beam at the exit surface of a 4-mm-thick, Ce^{3+}-doped silica glass sample for four different input laser fluences (0.8 J/cm^2, 6.4 J/cm^2, 8.3 J/cm^2, and 11 J/cm^2, respectively). At a lower peak fluence (<2 J/cm^2), the beam profile remains mostly unchanged. A significant narrowing of the beam is observed, however, at the sample's exit surface at higher fluences. These results clearly demonstrate a self-focusing behavior of the propagating beam into the material that strongly depends on the laser fluence.

(a)

(b)

G11077JR
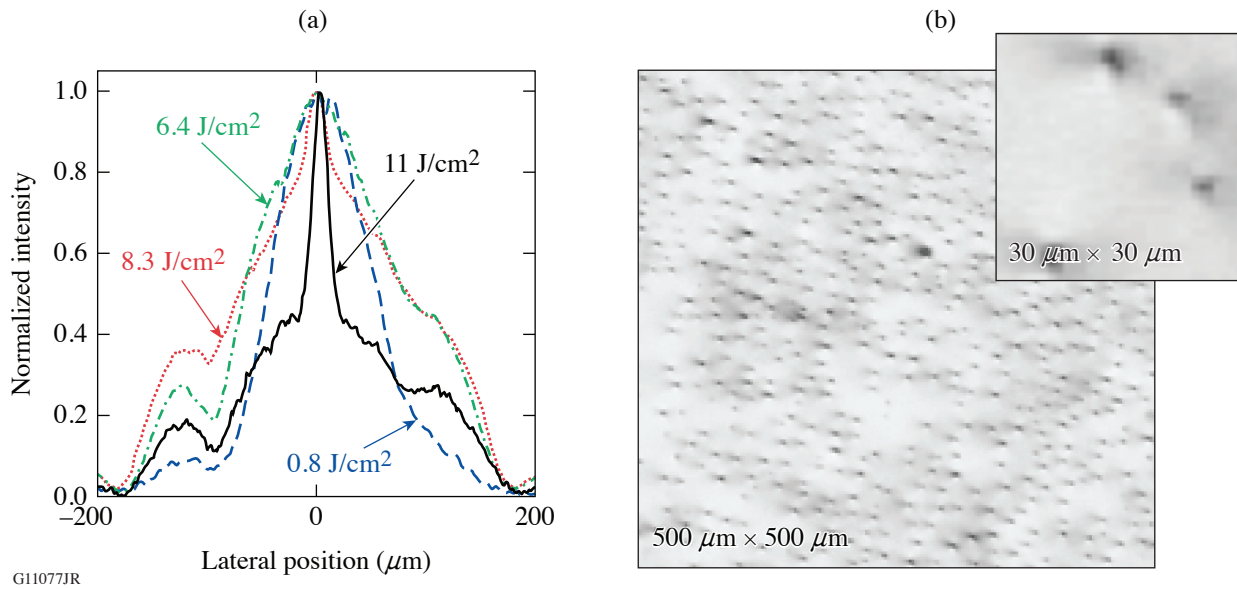
Figure 1

(a) The intensity profile along the middle of the laser beam at the output surface of a 4-mm-thick, Ce^{3+}-doped silica glass sample for different laser (peak) fluences. (b) Images of filamentation-induced damage in Ce^{3+}-doped silica 1.25 mm below the input surface under exposure to ≈ 20-J/cm^2, 351-nm, 5-ns flat-in-time pulses.

The same material was exposed to single pulses having a beam diameter of the order of 1 cm at various average laser fluences. The entire volume of the sample exposed to the laser beam was subsequently imaged at different depths, starting from the input surface and into the bulk in increments of 250 μm. Figure 1(b) represents a typical image at a depth of 1.25 mm below the surface from a section of the sample that was exposed to a fluence of ≈ 21 J/cm^2. This image demonstrates the presence of numerous filament damage sites with a diameter of ~2 to 3 μm. This is better demonstrated in the high-magnification inset. The filaments at this fluence are observed to start from a depth of ~500 μm and extend to a depth of ~1750 μm. The highest density of filament damage sites is observed ~1 mm below the surface for all fluences used in these experiments. An examination of individual filaments reveals that their length is ~750 μm.

A detailed investigation of the dynamics of this self-focusing behavior reveals that it arguably originates from a change of the index of refraction following the transition of electrons to a higher excited state. This modulation of the refractive index arises from the difference in the polarizability between the ground and excited states of the impurity ions and even transient defects formed during the excitation process. The relaxation time of this change of the refractive index is the same as the lifetime of the excited state; therefore, it can be much longer than the laser pulse (of the order of 100 ns for Ce^{3+}-doped silica glass). For large beams, the modulation of the refractive index leads to beam breakup and the formation of filaments as shown in Fig. 1(b). The filaments are located over a narrow depth zone (~2 mm) since the self-focusing mechanism is counteracted by the attenuation of the laser beam as it propagates inside the material.

The second damage-initiation mechanism in absorbing glasses is associated with heating of the material near the surface, resulting from the nonradiative relaxation following laser-energy deposition. This can support above-melting temperatures, which introduces nonreversible material modifications (damage). The dominant damage-initiating mechanism for a specific material and irradiation conditions depends on the material's electronic and thermophysical properties.

To understand this dual behavior of laser damage in absorbing glasses, we need to consider that there is a laser-induced damage threshold (LIDT) associated with the material surface reaching above melting temperature ($LIDT_{melt}$), as well as an analogous laser fluence for damage initiation via self-focusing ($LIDT_{focus}$). The experimentally observed damage behavior of a specific material and excitation condition is governed by the mechanism with the lowest threshold. The change in the damage mechanism

with beam size can arise from the thermomechanical properties of the material and the fact that the peak surface temperature can be a function of the laser spot size. For small beams, the flow of energy (such as via heat diffusion and/or electron transport) reduces the peak temperature, thereby increasing the effective $LIDT_{melt}$ value. On the other hand, for large beams, there is no (or not significant) energy flow, which leads to the generation of higher local temperatures for the same laser fluence. Consequently, a larger beam size promotes a higher localized temperature in the material for the same laser fluence. In materials with similar $LIDT_{melt}$ and $LIDT_{focus}$, experimentation with different laser beam spot sizes can lead to different observables because of the change in the governing damage-initiation mechanisms. For similar reasons, the local temperature can be a function of the pulse repetition rate.

1. S. G. Demos *et al*., Optica **2**, 765 (2015).

2. Yu. A. Demochko, I. F. Usol'tsev, and V. M. Shaposhnikov, Sov. J. Quantum Electron. **9**, 1556 (1979).

3. R. A. Miller and N. F. Borrelli, Appl. Opt. **6**, 164 (1967).

4. P. K. Whitman *et al*., Proc. SPIE **3578**, 681 (1999).

5. J.-H. Han *et al*., Acta Phys. Sin. **60**, 28106 (2011).

Tritium Extraction from Water

W. T. Shmayda,[1] C. R. Shmayda,[2] and G. Torres[3]

[1]Laboratory for Laser Energetics, University of Rochester
[2]Torion Plasma, Inc.
[3]Nuclear Sources and Services, Inc.

Tritiated water production is ubiquitous in facilities that handle tritium gas. Sources range from decontamination efforts, to the deliberate conversion of elemental tritium, to tritiated water in processes that strive to reduce emissions to the environment, to gaseous effluents, to the environment. At low concentrations, ranging from a few μCi/L to mCi/L, high throughputs are required to process the high-volume, low-activity water. Combined electrolysis and catalytic exchange (CECE) shows promise by offering high throughput, reliability, economic viability, and facile coupling to isotopic separation systems, if necessary. This summary will discuss the features of a CECE facility based on a 7-m^3/h throughput alkaline electrolysis cell.

As of 2018, there are 451 nuclear reactors operating in 31 countries with an additional 59 reactors currently under construction. All of these nuclear power stations have chronic releases of tritium that can be measured in the surrounding groundwater. In the U.S., for example, concentrations between 20 nCi/L and 0.1 μCi/L have been observed. The dose to an individual drinking 4.4 L of 1 μCi/L of water every day for a year is equivalent to only 30% of the annual dose received from natural background radiation. While the scientific community understands that the chronic release of tritium to the groundwater is not dose relevant, the public is far more sensitive to the issue. Even in locations where the ground water activity is below the EPA maximum contaminant level of 4 mrem per year, land owners have successfully sued nuclear power stations over the contamination. Therefore, chronic tritium release to the groundwater remains an imminent concern for any operator of a nuclear power station. Newly constructed fission or fusion plants require robust strategies to mitigate the release of tritium to the environment to help alleviate public backlash and limit legal liabilities.

The CECE technology has been under development for several years in national laboratories[1–6] but has seen limited commercial deployment. The process provides an elegant, compact, and powerful option to concentrate tritium activities in water. The system comprises a liquid phase catalytic column (LPCE) integrated with an electrolysis cell. A schematic of the system is seen in Fig. 1. The electrolysis cell provides a constant supply of elemental tritiated gas to the bottom of the LPCE column. As the gas is directed up the column, a counter flow of clean water is added to the top of the column. The isotopic exchange of the tritium from the rising elemental gas to the descending water has the effect of "washing" the tritium to the bottom of the column. Clean hydrogen gas is emitted from the top of the column, while the majority of the tritium is contained in the water at the bottom. The tritiated feed stock water can be combined with the tritiated water leaving the column to collect in a tank. This water is used to feed the electrolysis cell to create more elemental gas. If the molar feed rate of the clean water at the top of the column and the tritiated feed stock water at the bottom of the column are equal to the molar rate of release of clean hydrogen from the top of the column, the system will remain in balance with all of the tritium concentrating in the water in the bottom tank.

It can be shown that the height of a packed column depends on the isotopic separation factor in the electrolyzer (α_{el}), the isotopic separation factor (α_{col}) in the column, and the concentration at the top of the column (y_t); λ is the ratio of the molar gas
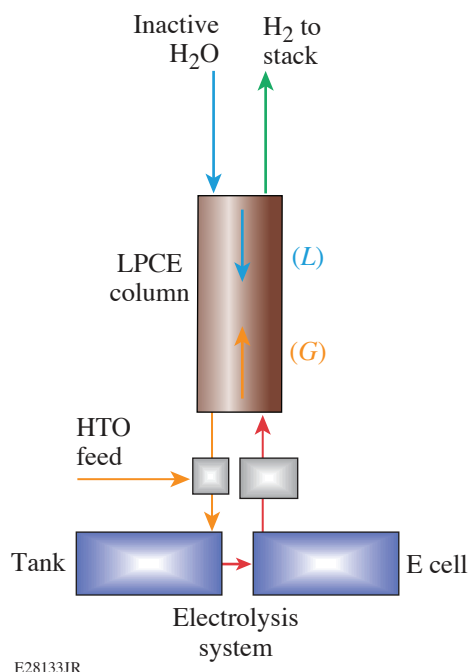
Figure 1
Schematic of the combined electrolysis and catalytic exchange system.

E28133JR

flow up the column (G) to the molar flow rate of water down the column (L) ($\lambda = G/L$); and the height-equivalent theoretical plate (HETP) for the catalyst according to the relation[7]

$$h = \text{HETP} * \frac{\ln\left(\dfrac{x_{el}}{\alpha_{el} * y_t} * \dfrac{\alpha_{col} - \lambda}{\alpha_{col} - 1}\right)}{\ln\left(\dfrac{\alpha_{col}}{\lambda}\right)}. \tag{1}$$

The quantities α_{el}, α_{col}, and HETP are fixed when operating at a fixed temperature with a particular catalyst. For a given gas-to-liquid molar ratio, the height of a column is determined by two parameters: the concentration of the electrolyte, x_{el}, and the concentration of the effluent at the top of the column, y_t. Both parameters are at the discretion of the end user.

Figure 2 illustrates the column-height dependence on those two parameters for fixed λ. It is more economical to operate at a higher λ because there will be less counter-flowing water that must to be electrolyzed back into elemental gas. For a chosen column height, the trade-off will be to operate at the highest possible λ within a prescribed emission discharge limit at the column top.

If the CECE system is being used to concentrate tritiated water for long-term storage or to reduce volume as the first step in tritium recovery, then the column height is selected for the maximum decontamination factor. Assuming the activity at the top of the column approaches zero, then in steady state, tritium balance requires that the amount of tritium introduced to the system ($L_f * x_f$) must equal the amount drawn as concentrate ($L_c * x_c$), where L_f is the molar feed rate into the electrolysis system at a concentration of x_f and L_c is the rate at which the concentrate is extracted from the system at a concentrate of x_c. It follows that the rate of concentrate draw is inversely proportional to the ratio of the feed activity to the concentrate activity:

$$L_c = \frac{x_f}{x_c} * L_f. \tag{2}$$
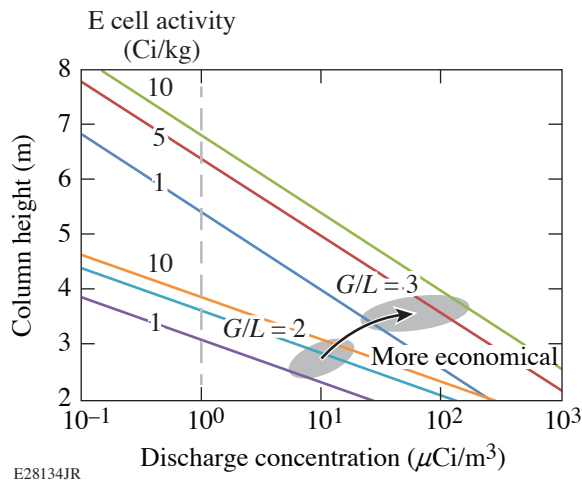
Figure 2

Column-height dependence on the discharge concentration and the gas-to-liquid molar ratio.

E28134JR

As an example, assume a feed concentration of 100 μCi/kg is delivered to the system operating at 90% efficiency, at a gas-to-liquid molar ratio of 2 ($\lambda = 2$) and driven by a 21-m^3/h electrolyzer. In steady state, this system will accept 418 U.S. barrels per year (66,480 L) and produce 3.3 L of concentrate at 2 Ci/L for a volume reduction of ~20,000. In this example, a column height of 3.9 m would result in an emission of 0.17 Ci per year and a net activity collection efficiency of 98%. Increasing the column height by an additional 0.7 m would reduce the effluent activity by a factor of 10. At these concentrations, a portion of the electrolyzed gas can be diverted to an isotope separation system for tritium recovery.

The use of nuclear power will continue to grow in the world driven by the need for carbon neutral energy systems. Whether the reactors are fission or fusion based, it will be incumbent on the operators to reduce tritium releases to appease the public perception. CECE systems similar to one described above provide an economical and robust form of tritium concentration and recovery. The experience developed in an industrial environment attests to the simplicity and efficacy of the systems. Options to recover tritium from light water over a broad range of activities and throughputs using the small footprint of the CECE technology indicate that this technology will become an important effluent mitigation tool in the future.

1. I. A. Alekseev *et al*., Fusion Sci. Technol. **41**, 1097 (2002).

2. J. P. Butler *et al*., in the *Proceedings of the Sixth International Congress on Catalysis*, edited by G. C. Bond, P. B. Wells, and F. C. Tompkins (Imperial College, London, 1977), Vol. 2, pp. 747–756.

3. J. P. Butler *et al*., U.S. Patent No. 4,228,034 (14 October 1980).

4. I. Cristescu *et al*., Fusion Sci. Technol. **41**, 1087 (2002).

5. L. Geens *et al*., Commission of the European Communities (CEC), Luxembourg, Report EUR-11551 (1988).

6. A. Perevezentsev *et al*., Fusion Sci. Technol. **41**, 1107 (2002).

7. A. Bruggeman *et al*., in *Management of Gaseous Wastes from Nuclear Facilities*, IAEA-SM-245/52 (IAEA, Vienna, Austria, 1980), pp. 157–173.

Distribution of Tritium in the Near Surface of Stainless-Steel 316

M. Sharpe,[1] C. Fagan,[1,2] and W. T. Shmayda[1]

[1]Laboratory for Laser Energetics, University of Rochester
[2]Department of Chemistry, University of Rochester

The interaction and subsequent retention of tritium in stainless steel impacts many activities and procedures at LLE, ranging from protium contamination of the DT fuel supply to decontamination procedures for items fielded in OMEGA. The adsorption of tritium onto the surface of stainless steel represents the first step in the overall retention and permeation of tritium through stainless steel. Understanding the distribution of tritium in the surface region is necessary in determining how tritium responds to an exposure of tritium gas. This knowledge can help determine the effectiveness of barrier materials deposited on stainless-steel surfaces and various surface treatments designed to reduce tritium absorption. Measurement of the near-surface concentrations that develop after storage help quantify the classical observation of tritium migration to steel surfaces after surface decontamination.[1]

There are three regions of interest regarding tritium retention in stainless steel: the surface, the near surface, and the bulk metal. Each region has different chemistry and structures, causing various quantities of tritium to bind in each region. The bulk metal is comprised of a regular lattice of metal atoms, where tritium binds in the interstitial spaces between the metal atoms. The "near surface" represents the transition between the regular metal lattice and the native metal oxide. The surface of stainless steel contains several monolayers of water molecules, which are bound to the metal oxide by a hydroxide layer.

Measuring the tritium concentrations in each region requires three different techniques, each specifically designed to probe the tritium content in that region. Tritium bound to the steel's surface was measured by immersion in a zinc chloride ($ZnCl_2$) solution. This technique has been effective at removing surface-bound tritium without etching into the metal oxide.[2,3] The tritium concentrations in the near surface were measured by dissolving the metal in diluted mixtures of hydrochloric and nitric acid.[4,5] The residual tritium was determined by heating the samples to elevated temperatures.

The migration of tritium from the bulk to the surface was measured by removing surface tritium with an $ZnCl_2$ wash and an acid etched after storing the sample for several days. This removal and storage sequence was repeated several times to monitor how much tritium had migrated to the surface. Such an experiment mimics the effectiveness of decontamination procedures used to clean steel surfaces exposed to tritium gas.

The total tritium contained in the stainless-steel 316 (SS316) samples was 180 ± 20 MBq (4.9 ± 0.5 mCi). The results are shown in Fig. 1 as a function of the storage time for each sample. Six different sets of SS316 samples are included in this figure. Each set was charged with tritium on a different date. These data show negligible, if any, loss of tritium over the 70-day storage period in a dry environment. Two samples contained significantly more tritium than observed on average. This apparent higher activity is most likely a result of cross contamination during sampling.

The combination of the $ZnCl_2$ wash and acid etching provides the distribution of tritium on the surface and in the near surface ($<10 \ \mu$m). The concentration profiles determined from these measurements are shown in Fig. 2. Nine different samples were used. Each sample was stored from 33 to 233 days between charging and measurement. The concentration profiles show that the adsorbed water layers contain large concentrations of tritium. These concentrations decrease by a factor of 10^7 over an $\sim$5-μm
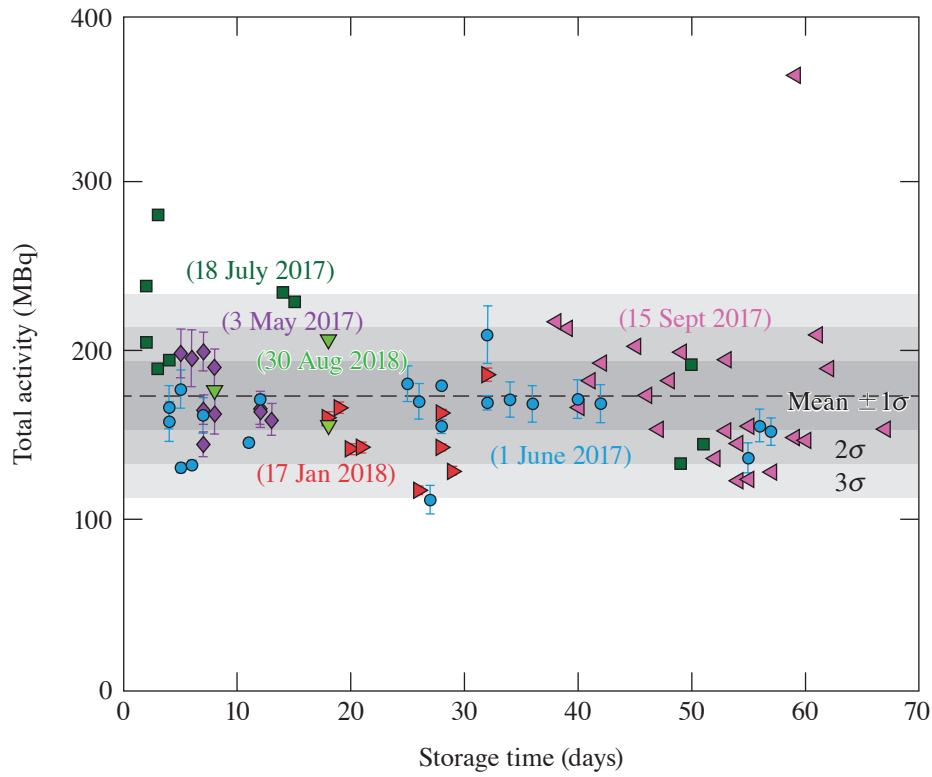
E28123JR1

Figure 1
Summary of total tritium inventories from six different sets of samples. Each set was charged with tritium on a different date.
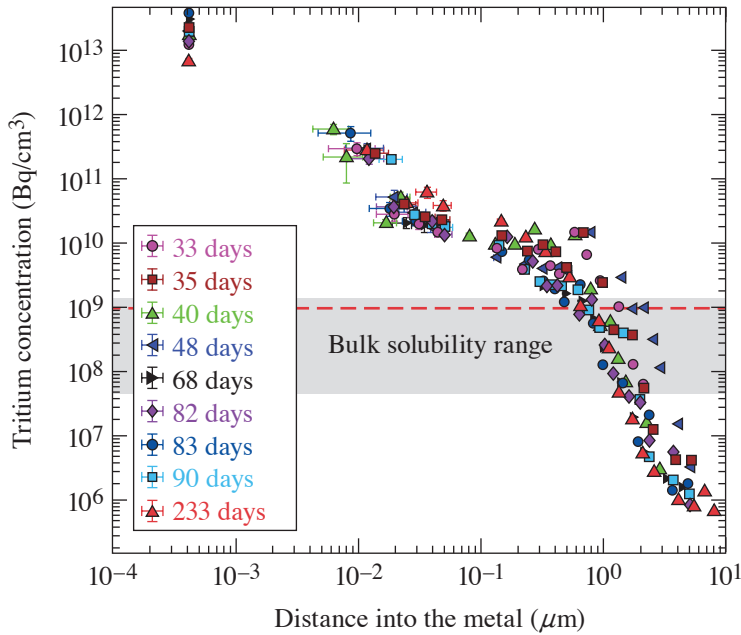
Figure 2
Tritium concentration profiles in the near surface of SS316, as measured using a ZnCl$_2$ wash, followed by acid etching. Shown in the figure are the results of nine different samples, stored from 33 to 233 days prior to measurement.

E28123JR2

depth into the metal. Figure 2 also shows the mean and range of hydrogen isotope solubilities in SS316 at 25°C from higher temperature data reported in the literature.[6]

The measured concentration profiles in the near surface of SS316 indicate several things: First, ~30% of the surface is occupied by tritium. Second, the distribution of tritium in the near surface does not change during the 33 to 233 days of storage. This is striking since tritium migration is expected, given the observed concentration gradient and the diffusivity of tritium in SS316 reported in the literature. Tritium appears to be in a quasi-equilibrium state. Finally, comparing the measured concentrations with the reported solubility of tritium in SS316 shows the measured concentrations at depths less than ~1 μm exceed the reported solubilities. These higher concentrations are attributed to the storage capacity of the metal oxide.

Thermal desorption, acid etching, and $ZnCl_2$ wash measurements show the distribution of tritium to be fixed over the measured time period with 40±20% residing in the bulk metal, 42±9% in the near surface, and 21±5% in the adsorbed water.

Tritium migration from the SS316 surface was measured for several samples. Figure 3 presents activity as a function of storage interval, where each interval was between 2 and 4 days. Tritium migrating to the surface decreases after each successive cleaning and storage period, suggesting a depletion of tritium in the near-surface region and an inability to resupply the surface. Perturbing the quasi-equilibrium concentration profiles (shown in Fig. 2) by removing surface tritium concentrations cause some of the tritium to migrate back to the surface from the underlying subsurface in order to re-establish the equilibrium between the surface and the subsurface.
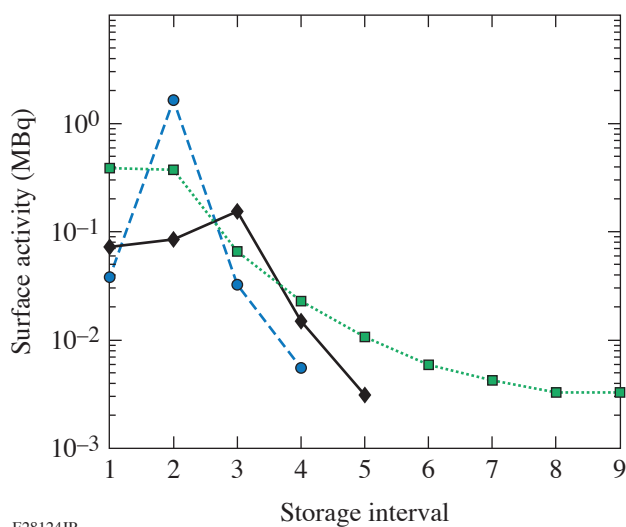
Figure 3
Surface activity for three SS316 samples, measured after the surfaces were cleaned using acid etching and then stored for 2 to 4 days.

E28124JR

1. R. A. Surette and R. G. C. McElroy, Fusion Technol. **14**, 1141 (1988).

2. Y. Tanaka *et al.*, Mater. Trans. **49**, 805 (2008).

3. M. D. Sharpe *et al.*, Fusion Eng. Des. **130**, 76 (2018).

4. T. Hirabayashi and M. Saeki, J. Nucl. Mater. **120**, 309 (1984).

5. R.-D. Penzhorn *et al.*, J. Nucl. Mater. **353**, 66 (2006).

6. M. Sharpe, W. T. Shmayda, and W. U. Schröder, Fusion Sci. Technol. **70**, 97 (2016).

Electrochemical Synthesis of Copper Nanoparticles on Hydroxyapatite Coatings for Antibacterial Implants

R. Ghosh,[1] S. Westgate,[1] M. Z. Yates,[1,2] O. Swart,[3] and B. L. Miller[3]

[1]Department of Chemical Engineering, University of Rochester
[2]Laboratory for Laser Energetics, University of Rochester
[3]Department of Dermatology, University of Rochester

The coating of metals with thin ceramic layers is used to reduce the rate of corrosion, add a thermal insulating barrier, or enhance biological activity, among other applications. In this study, coatings of the calcium phosphate ceramic hydroxyapatite (HA) were applied to titanium, and then copper nanoparticles were added to provide antibacterial activity. Synthetic HA has a similar chemical composition to the natural HA found in the mineral component of bone tissue. Coatings of HA on titanium are known to enhance the rate under which an orthopedic or dental implant integrates with surrounding bone. In implant surgery, prophylactic antibiotics are typically used to reduce the potential for post-surgical bone infection. However, the use of antibiotics is undesirable because of the development of resistant strains of bacteria. Metal nanoparticles, such as those reported here, offer a route to provide antibacterial activity without the risk of creating antibiotic-resistant strains of bacteria.

In the present study, a method called cathodic electrolytic deposition was used to synthesize nanoscale HA coatings.[1] Our previous work demonstrated a novel two-stage approach to synthesize silver-hydroxyapatite composite coatings.[2] The cathodic electrolytic process was used in the first stage to synthesize HA on titanium. The HA-coated titanium was then used as the cathode in a second-stage reaction to electrochemically reduce silver ions in solution. The process produced an HA coating decorated with silver nanoparticles, and the silver particles were shown to impart antibacterial activity. While silver is known to be a potent antimicrobial agent, it does pose a risk of toxicity to mammalian cells at high concentrations. In the present study, a similar two-stage synthesis approach was used to create composite copper–hydroxyapatite (Cu–HA) coatings. Copper was chosen because it has the potential for antibacterial activity while being less toxic to other healthy cells.

Figure 1 shows electron microscopy images of Cu–HA coatings produced using varying concentrations of Cu salt in the electrolyte solution used during the second-stage reaction. The HA crystals are visible as nanoscale rods in all images. At the highest Cu salt concentrations, the metallic copper is deposited as a mixture of nanoparticles and larger dendrite structure, as seen in Figs. 1(a) and 1(b). At lower Cu salt concentrations, the number of dendrites declines and, primarily, Cu nanoparticles are synthesized, as seen in Figs. 1(c) and 1(d). The presence of HA was confirmed using x-ray diffraction, and metallic Cu and copper oxide were confirmed on the surface using x-ray photoelectron microscopy.

A series of Cu–HA coatings was made having varying copper content, and the growth of the bacteria *E. coli* and *S. aureus* was measured in the presence of these coatings. It was found that the number of bacteria colony forming units declined with increasing copper content in the coatings. With the highest measured copper content of 6.6 at. %, the number of colony-forming units remaining after 8 h of cell culture declined 78% for *E. coli* and 83% for *S. aureus*.

The results show that the copper nanoparticles are effective at killing a fraction of the bacteria but do not provide a means to completely sterilize an infected surface. Compared to our prior work,[2] copper is less effective than silver in killing bacteria. Copper offers the advantage, however, of less toxicity than silver toward healthy cells. The composite coatings synthesized here
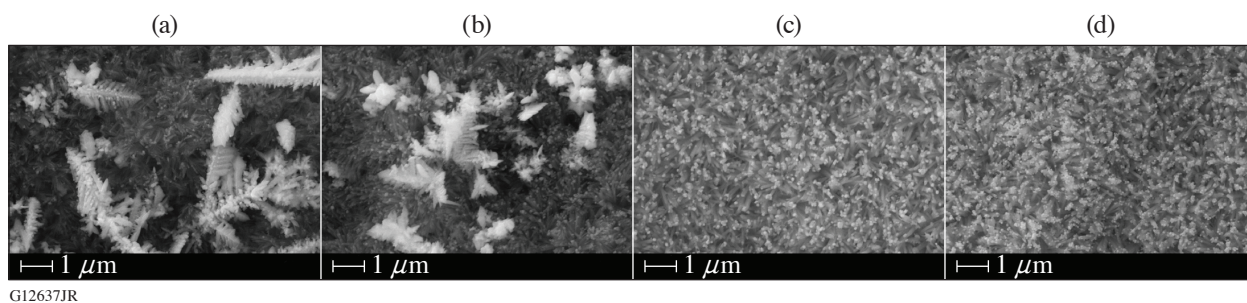
Figure 1
SEM images of Cu–HA composite coatings formed by an electrochemical copper reduction reaction using 12.8-mA/cm^2 current applied for 7 min with a CuSO$_4$ concentration in the electrolyte of (a) 0.625 mM, (b) 0.5 mM, (c) 0.375 mM, and (d) 0.25 mM.

may, therefore, offer a lower-risk route to reducing or eliminating the need for prophylactic antibiotic use in orthopedic implant surgery. In an otherwise sterile surgical environment, the number of bacteria present is expected to be low. Copper on the surface of the implant may reduce the likelihood that any bacteria present develop into a bone infection at the implant surface.

1. I. Zhitomirsky, Adv. Colloid Interface Sci. **97**, 279 (2002).

2. C. Fu *et al.*, Surf. Coat. Technol. **301**, 13 (2016).

Silver-Hydroxyapatite Composite Coatings with Enhanced Antimicrobial Activities Through Heat Treatment

X. Zhang,[1] W. Chaimayo,[2] C. Yang,[1] J. Yao,[1] B. L. Miller,[2] and M. Z. Yates[1,3]

[1]Department of Chemical Engineering, University of Rochester
[2]Department of Dermatology, University of Rochester
[3]Laboratory for Laser Energetics, University of Rochester

Ceramic coatings find applications in corrosion protection, thermal insulation, altering wetting, electrical insulation, and enhancing chemical or biochemical surface properties. This study focuses on the electrochemical synthesis of nanoscale coatings of the ceramic hydroxyapatite (HA), a calcium phosphate with the stoichiometric formula $Ca_{10}(PO_4)_6(OH)_2$. The HA coating was synthesized from an aqueous electrolyte solution using a process called cathodic electrolytic deposition.[1] After forming the coating on a titanium cathode, a second cathodic electrochemical reaction was used to reduce silver ions from an electrolyte solution and deposit metallic silver nanoparticles onto the HA coating. The resulting silver-hydroxyapatite (Ag-HA) composite coating was investigated for its ability to kill bacteria. Coatings of HA on titanium find commercial application in dental and orthopedic implant applications, where the HA layer is known to enhance the rate of integration of metallic implants with surrounding bone tissue. One of the most serious complications of implant surgery is infection of the bone. The coatings show promise in lowering the chance of infection without the use of antibiotics that create antibiotic-resistant strains of bacteria.

Figure 1 shows electron microscopy images of the HA coating on titanium before and after electrochemical reduction of silver. The HA grows on the surface as nanoscale rod-shaped crystals, as seen in Fig. 1(a). The metallic silver nanoparticles can be seen in Fig. 1(b) as spherical nanoparticles that form preferentially on the tips of the HA nanocrystals. Although HA is known to be an electrically insulating material, our previous results show that HA can conduct electricity if the applied potential is high enough.[2] The fact that metallic silver forms on the tips of the HA indicates that electrons are passing through the HA crystals in

(a)   (b)

T2609JR
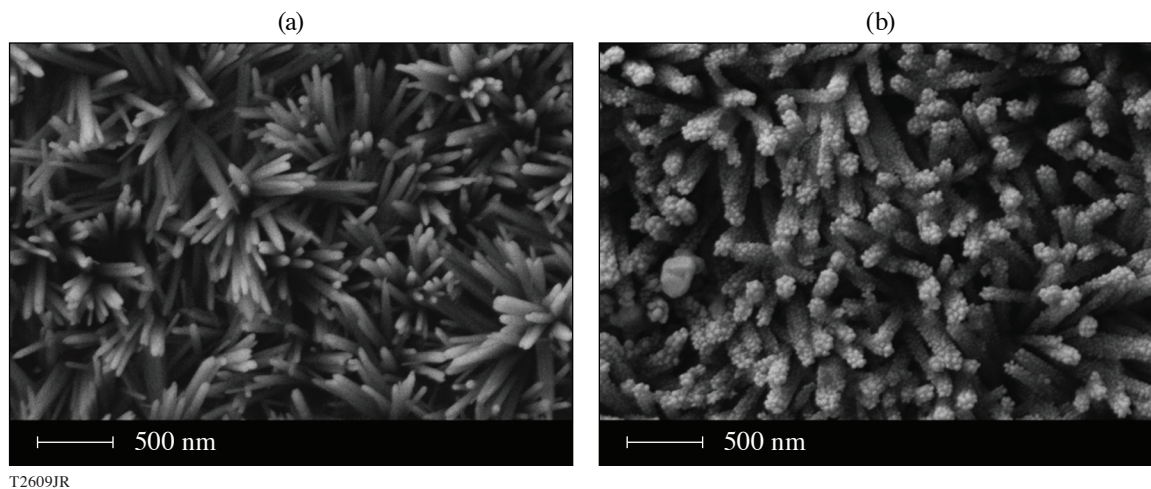
Figure 1
Scanning electron microscope (SEM) images of Ag-HA coating (a) before and (b) after electrochemical deposition of Ag nanoparticles.

order to electrochemically reduce silver cations (Ag^+) in solution to metallic silver (Ag^0). The HA crystal phase was confirmed with x-ray diffraction, and the metallic silver on the surface was confirmed with x-ray photoelectron spectroscopy.

Composite Ag-HA coatings, similar to those shown in Fig. 1, were found by our group to kill bacteria.[3] However, the effectiveness of the coating in killing bacteria varied significantly from sample to sample. The antibacterial activity of silver is related to the dissolution of silver ions into solution. It was postulated that the release of silver ions would be enhanced by the formation of silver oxide, which undergoes the following reactions:

$$Ag_2O + H_2O \longrightarrow 2AgOH \tag{1}$$

$$AgOH \longrightarrow Ag^+ + OH^- \tag{2}$$

To test this hypothesis, the Ag-HA coatings were heated in air at 170°C for 8 h to form an oxide layer. The formation of silver oxide on the surface after heating was confirmed using x-ray photoelectron spectroscopy. Next, the growth of *Escherichia coli* (*E. coli*) was monitored in the presence of HA and Ag-HA coatings before and after the heat treatment.

Light scattering was used to characterize the relative number of bacteria versus time, as shown in Fig. 2. The reported optical density is proportional to the number of bacteria in the sample. The results demonstrate that heat treatment enhances the antibacterial activity and reduces the variation in antibacterial activity from sample to sample. The results demonstrate a simple route to form coatings that may simultaneously enhance integration of implants with surrounding bone tissue while reducing the likelihood of post-surgical bone infection.
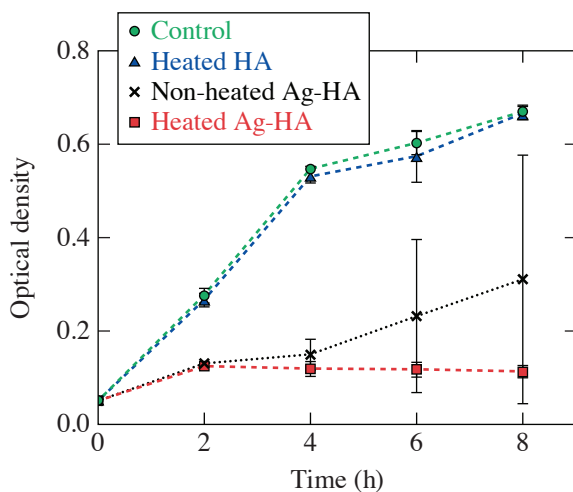
Figure 2
The growth of *E. coli* when exposed to HA and Ag-HA coatings measured by light scattering. Data points indicate the mean value, and error bars indicate standard deviation.

T2610JR

1. I. Zhitomirsky, Adv. Colloid Interface Sci. **97**, 279 (2002).

2. C. Fu *et al*., Chem. Mater. **27**, 1164 (2015).

3. C. Fu *et al*., Surf. Coat. Technol. **301**, 13 (2016).

Terahertz Time-Domain Spectroscopy of Graphene Nanoflakes Embedded in a Polymer Matrix

A. Koroliov,[1,#] G. Chen,[1] K. M. Goodfellow,[1] A. N. Vamivakas,[1] Z. Staniszewski,[2] P. Sobolewski,[2] M. El Fray,[2] A. Łaszcz,[3] A. Czerwinski,[3] C. P. Richter,[4] and R. Sobolewski[1,3]

[1]University of Rochester
[2]Polymer Institute, West Pomeranian University of Technology, Poland
[3]Institute of Electron Technology, Poland
[4]University of Iceland, Iceland
[#]Present address: Center for Physical Sciences and Technology, Vilnius, Lithuania

Polymer nanocomposites are prepared by including a nanofiller (carbon, ceramic, metal/metal oxide, and/or others) in a polymer matrix to alter (or improve) its properties, such as mechanical, electrical, and optical properties, barrier properties, flame resistance, etc.[1] Recently, a great deal of interest has been focused on carbon nanofillers and, in particular, graphene. Graphene is a 2-D nanomaterial consisting of sheets of carbon atoms bonded by sp^2 bonds in a hexagonal configuration: its unique mechanical, electrical, thermal, and optical properties have been extensively studied.[2] These properties have been leveraged in the development of a wide range of different graphene–polymer nanocomposites,[3] using a variety of fabrication methods and polymer types, for numerous structural and functional applications,[4] including, e.g., biomedical devices,[5] biosensing,[6] and gas barrier membranes.[7]

Here we report the use of a THz time-domain spectroscopy (THz-TDS) to characterize graphene nanofiller dispersion within multiblock copolyester nanocomposite materials. Both the copolymer matrix and the nanocomposites were developed to serve as construction materials for extracorporeal heart-assist devices in the context of the Polish Artificial Heart Program.[8] The test samples used were processed using the same compression molding process as the prototype pneumatic membrane. To our knowledge, this is the first time that the dispersion of graphene nanoplatelets within a nanocomposite—prepared at an industrially relevant scale and using an economically viable process—has been studied by the THz-TDS method. Consequently, this work serves as an important proof of concept of THz-TDS of nanocomposites within the product development chain.

Two different neat copolymers were prepared, with different hard to soft segment ratios, resulting in a more elastic material with 40 wt% of hard segments (PET-DLA 4060) and a stiffer copolyester with 60 wt% of hard segments (PET-DLA 6040). Additionally, nanocomposites with the same hard to soft segment ratios but with 1 wt% of a commercial graphite nanoplatelet nanofiller (Graphene Supermarket, Grade A0-3) were prepared via *in-situ* polymerization.[9,10]

The THz-TDS system, used to measure the THz-range transmission spectra of both the neat copolymers and graphene nanocomposite samples, was based on a commercial, low-temperature–grown GaAs (LT-GaAs) photoconductive antenna emitter and detector from TeraVil Ltd, Vilnius, Lithuania.[11] The emitter and detector were excited and probed, respectively, by 100-fs-wide pulses, with an 800-nm wavelength and a 76-MHz repetition rate, generated by a femtosecond Ti:sapphire laser. The spectral range of the spectrometer was ~4 THz, with maximum amplitude at ~0.5 THz. The sample was placed directly between the emitter and detector, and measurements were taken at room temperature. To reduce the influence of water absorption, the THz emitter, detector, and sample holder were placed inside a Plexiglas® box that was purged with dry nitrogen, ensuring that the humidity during the measurement was below 5%.

For each sample, we first performed a reference run with no sample inside the spectrometer to confirm the performance of the system. Next, we took two measurements: one of a graphene nanocomposite and the other of a corresponding neat copolymer specimen. To get better results and reduce noise, each set of measurements consisted of at least ten averages. Our measurements were focused on two different sample types: nominally a 0.3-mm-thick, elastic PET-DLA 4060 copolymer ("thin sample") and a 0.9-mm-thick, stiffer PET-DLA 6040 copolymer ("thick sample"). For both sample types, the nanofiller content was the same, i.e., 1 wt%. Since our further analysis crucially depends on the sample thickness, all measurements were repeated several times at different spots of the test sample.

Figure 1(a) presents time-domain signals transmitted through dry nitrogen (the reference measurement), the thin and thick neat copolymer, and the corresponding 1-wt% graphene–polymer nanocomposite samples, respectively, while Fig. 1(b) presents the corresponding power spectra of our time-domain signals obtained by means of fast Fourier transformation. We note that while both copolymers absorb THz radiation, as compared to the dry-nitrogen reference signal, adding graphene flakes to the polymer matrix substantially reduces the bandwidth of the power spectrum, obviously because of the extra absorption of THz radiation by nanoflakes. The cutoff frequencies for the thin copolymer sample and the corresponding 1-wt% graphene-polymer nanocomposite are ~3.1 THz and 2.9 THz, respectively, while for the thick copolymer and the 1-wt% graphene–polymer nanocomposite, they are 2.25 THz and 1.75 THz, respectively.
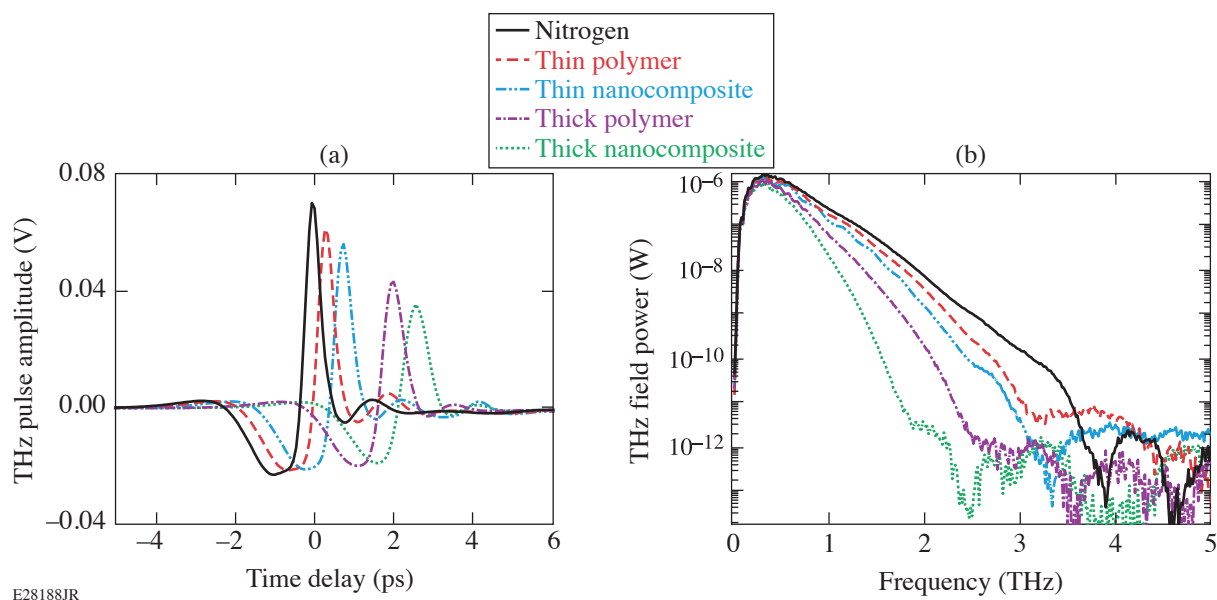
Figure 1
(a) Time-resolved transient signals for the tested thin and thick polymers and 1-wt% graphene nanocomposite samples and the empty spectrometer (nitrogen). (b) The corresponding power spectra showing absorption of the samples. Note: The thin samples consist of the PET-DLA 4060 copolymer, while the thick ones consist of PET-DLA 6040.

Using Fresnel equations, the THz-TDS approach allowed us to find the complex index of refraction $\hat{n}(\omega) = n(\omega) + i\kappa(\omega)$ and the dielectric function $\hat{\varepsilon}(\omega) = \varepsilon_1(\omega) + i\varepsilon_2(\omega)$, as well as the complex $\hat{\sigma}(\omega)$ of our graphene nanocomposite samples. The $\hat{\sigma}(\omega)$ spectrum was, subsequently, fitted using the Drude–Smith model.[12] The excellent fit confirmed applicability of the Drude–Smith approach to modeling the carrier transport in our graphene–polymer nanocomposites, indicating that our nanofiller flakes were fully isolated in the polymer matrix. The high quality and uniformity of the dispersion were implied by the high value of the conductivity and moderate effective dielectric constant retained by the graphene nanoflakes.

In summary, the THz-TDS method probes the dielectric properties of the sample in an almost cm^2 cross-section beam path, thereby providing "global" information regarding the dispersion of graphene and its *in-situ* electronic quality. Because it is a nondestructive testing method, it holds great potential for monitoring any nanofiller dispersion in a polymer matrix throughout the product-development chain: after polymer nanocomposite synthesis, following processing into a given prototype, and even after product testing.

1. D. R. Paul and L. M. Robeson, Polymer **49**, 3187 (2008).

2. Y. Zhu *et al.*, Adv. Mater. **22**, 3906 (2010).

3. J. R. Potts *et al.*, Polymer **52**, 5 (2011).

4. K. Hu *et al.*, Prog. Polym. Sci. **39**, 1934 (2014).

5. M. Silva, N. M. Alves, and M. C. Paiva, Polym. Adv. Technol. **29**, 687 (2018).

6. P. Sobolewski, M. Piwowarczyk, and M. E. Fray, Macromol. Biosci. **16**, 944 (2016).

7. Y. Cui, S. I. Kundalwal, and S. Kumar, Carbon **98**, 313 (2016).

8. M. El Fray and M. Czugala, WIREs Nanomed. Nanobi. **4**, 322 (2012).

9. Z. Staniszewski and M. El Fray, Polimery **61**, 482 (2016).

10. Z. Staniszewski *et al.*, Eur. Polym. J. **107**, 189 (2018).

11. A. Geižutis *et al.*, Opt. Mater. **30**, 786 (2008).

12. N. V. Smith, Phys. Rev. B **64**, 155106 (2001).

Tunable UV Upgrade on OMEGA EP

B. E. Kruschwitz, J. Kwiatkowski, C. Dorrer, M. Barczys, A. Consentino, D. H. Froula, M. J. Guardalben, E. M. Hill,
D. Nelson, M. J. Shoup III, D. Turnbull, L. J. Waxer, and D. Weiner

Laboratory for Laser Energetics, University of Rochester

Controlled experiments are necessary to test and refine simulation tools for the mitigation of cross-beam energy transfer (CBET) in direct-drive laser-driven inertial confinement fusion using wavelength detuning.[1–3] To this end, experiments have been proposed at the Omega Laser Facility that feature a wavelength-tunable UV beam coupled into the target chamber of the 60-beam OMEGA laser (via the P9 port). The new capability is referred to as the tunable OMEGA P9 (TOP9) beam. These experiments will characterize the interaction of the tunable beam with one or more fixed-wavelength beams from the 60-beam OMEGA Laser System as a function of wavelength detuning, polarization, and interaction angle. The top-level requirements for the tunable UV beam are dictated by the experimental needs and are listed in Table I.

Table I: Top-level system requirements for the tunable UV beam for CBET mitigation experiments.

Parameter	Minimum requirement	Goal
Wavelength-tuning range	350.2 to 353.4 nm	
Wavelength step size	≤0.1 nm	
UV power on target	0.1 TW (351 nm to 352.6 nm) 0.01 TW (350.2 nm to 353.4 nm)	0.5 TW for pulses ≤1 ns 0.1 TW for pulses ≤2.5 ns (full tuning range)
Polarization	(1) linear, direction rotatable over 2π (2) random (distributed polarization rotator)	

An OMEGA EP beamline[4] was chosen in order to leverage both the short- and long-pulse capabilities of the OMEGA EP beamline, as illustrated in Fig. 1. The TOP9 system utilizes the short-pulse optical parametric chirped-pulse–amplification (OPCPA) front end to take advantage of the spectrally broad gain in the optical parametric amplification (OPA) process. For the TOP9 system, the OPCPA front end is converted into a tunable OPA system by replacing the chirped broadband seed laser with a tunable narrowband laser.[5] The pulses are then injected into the OMEGA EP beamline for amplification to the >100-J level. The TOP9 system also takes advantage of the existing long-pulse UV infrastructure of the OMEGA EP beamline, with the frequency-conversion crystals (FCC's) providing frequency tripling, and suites of laser diagnostics characterizing the laser performance at each stage.

A beam transport system (see Fig. 2) was designed and built to transport the UV beam through the shield wall between the OMEGA EP and OMEGA Laser Bays, where it is directed into the P9 port of the OMEGA target chamber and focused to target. The OMEGA EP periscope features a retractable lower mirror to intercept the TOP9 beam after the FCC. A vacuum image relay limits beam degradation caused by diffraction and reduces the UV beam path in air. A new platform was built onto the north-end mirror structure in the OMEGA Target Bay to support the image relay and other associated optics, including an insertable distributed polarization rotator or a rotatable half-wave plate, the combination satisfying the system's polarization control requirements.
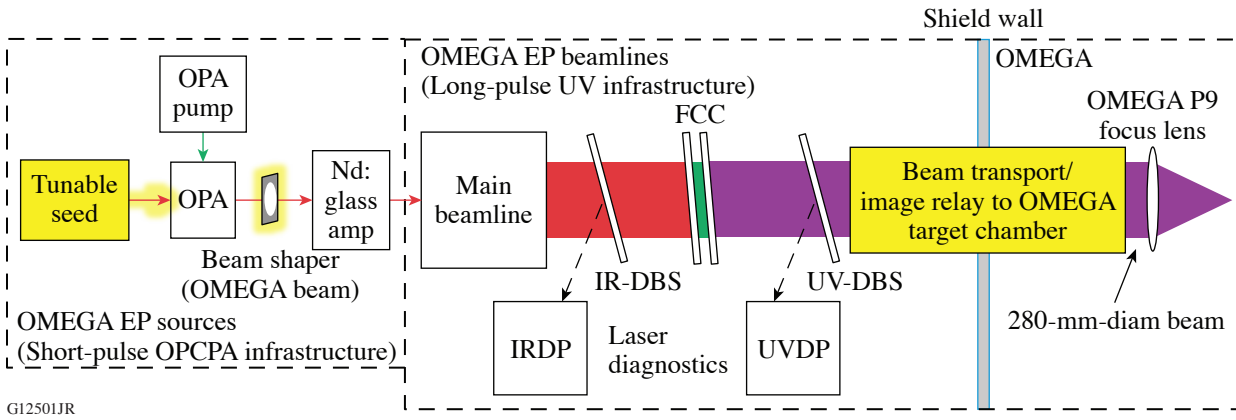
Figure 1
High-level diagram of the TOP9 OMEGA EP beam with upgraded elements highlighted in yellow. (OPA: optical parametric amplification; OPCPA: optical parametric chirped-pulse amplification; IR-DBS: infrared diagnostic beam splitter; IRDP: infrared diagnostics package; FCC: frequency-conversion crystals; UV-DBS: ultraviolet diagnostic beam splitter; UVDP: ultraviolet diagnostics package).
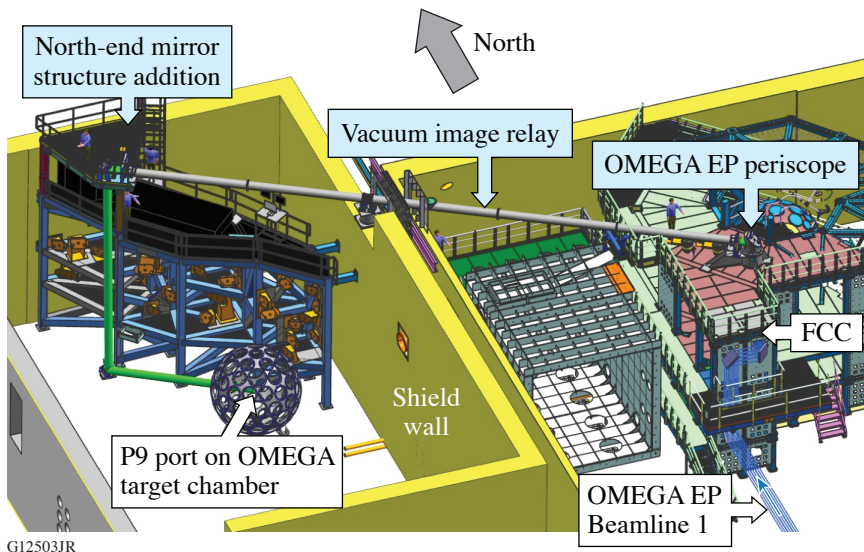
Figure 2
Solid-model drawing of the TOP9 transport system with key features indicated.

The performance envelope (plotted in Fig. 3) defines the range of pulse durations and energies that can be delivered with the tunable UV beam; it was developed based on consideration of a number of limiting effects. For short-duration pulses, the UV power is limited by concerns over small-scale self-focusing caused by the nonlinear Kerr effect in the transmissive optical materials (ΣB), comprising the TOP9 transport system and final optics.[6] For longer-duration pulses, the performance is limited by the development of transverse stimulated Brillouin scattering (SBS) in the optics.[7] Shots to the OMEGA EP target chamber allow for higher energies as a result of a larger beam size available, fewer transmissive optics in the transport path, and proximity to the target chamber.

The TOP9 beam has been commissioned to the OMEGA target chamber. The full-beam small-signal net gain as a function of wavelength was measured using a series of shots to a full-aperture calorimeter at the output of the transport spatial filter. The laser system produces the required 1ω energy at the extreme wavelengths by pumping up to 9 of the 11 main amplifier disks that are available in the OMEGA EP beamline. Longitudinal chromatic aberration in the beamline was measured and found to be corrected to $<\lambda/20$ by OMEGA EP's diffractive color-correcting injection lens. Near-field beam quality has been measured to be consistent with standard OMEGA EP performance.
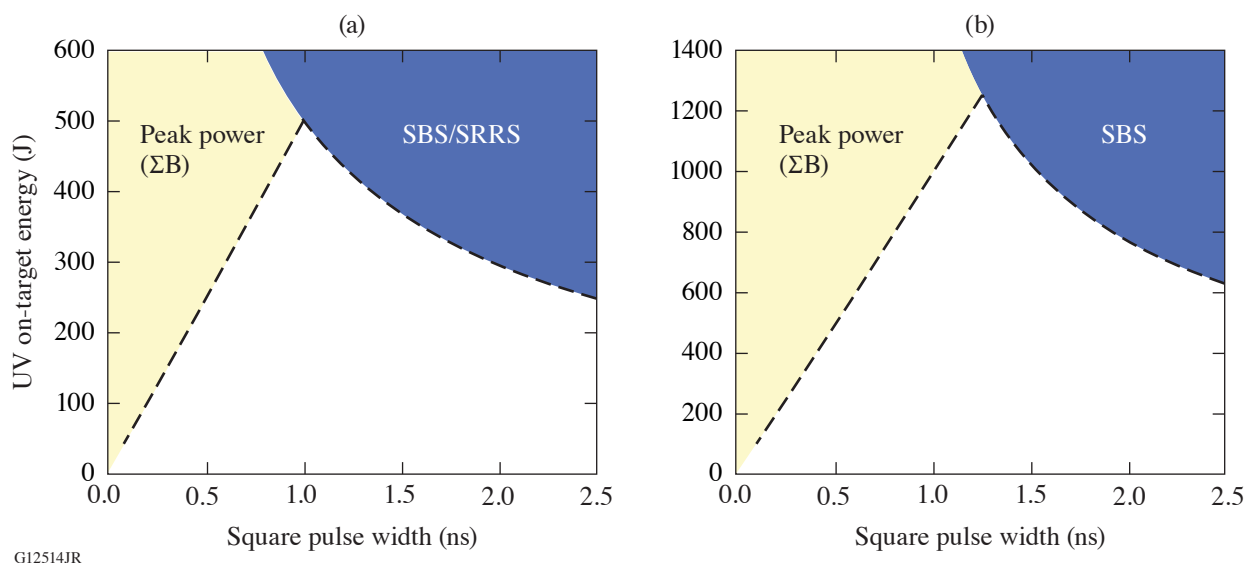
Figure 3

Performance envelope (maximum on-target energy versus square-pulse duration) for tunable UV shots to (a) the OMEGA target chamber (28-cm-diam round beam) and (b) the OMEGA EP target chamber (36-cm-sq beam). SRRS: stimulated rotational Raman scattering.

Pulse shaping is yet another active area of development. To maintain stability, the OPA is operated in saturation, which renders the creation of arbitrary pulse shapes difficult. Current pulse shapes are square at the output of the front-end OPA stages and tend to be distorted because of gain saturation in the downstream Nd:glass amplifiers and nonlinear frequency conversion. Nevertheless, arbitrary pulse shaping has been demonstrated in a laboratory prototype,[5] and it is a goal to provide arbitrarily shaped pulses with tailored ramps, steps, and other features that are currently available with the standard front ends of both OMEGA and OMEGA EP.

Construction of the tunable UV system was completed in May 2018, and commissioning of the system to the OMEGA target chamber was completed in June 2018. To date, the system has performed well in four experimental campaigns that studied CBET and other laser–plasma interactions, and it will enable future experiments that will advance the effort to mitigate CBET.

1. I. V. Igumenshchev *et al.*, Phys. Plasmas **19**, 056314 (2012).

2. J. A. Marozas *et al.*, Phys. Plasmas **25**, 056314 (2018).

3. D. Turnbull *et al.*, Plasma Phys. Control. Fusion **60**, 054017 (2018).

4. J. H. Kelly *et al.*, J. Phys. IV France **133**, 75 (2006).

5. C. Dorrer *et al.*, Opt. Express **25**, 26,802 (2017).

6. A. E. Siegman, Lasers (University Science Books, Mill Valley, CA, 1986), pp. 385–386.

7. J. R. Murray *et al.*, J. Opt. Soc. Am. B **6**, 2402 (1989).

In-Tank, On-Shot Characterization of the OMEGA Laser System Focal Spot

L. J. Waxer, K. A. Bauer, E. C. Cost, M. Heimbueger, J. H. Kelly, V. Kobilansky, S. F. B Morse, D. Nelson, R. Peck, R. Rinefierd, S. Sampat, M. J. Shoup III, D. Weiner, G. Weselak, and J. Zou

Laboratory for Laser Energetics, University of Rochester

The success of inertial confinement fusion experiments conducted on LLE's OMEGA 60-beam laser depends on the uniform illumination of the target. For these experiments, not only is the focal-spot intensity (i.e., power/unit area) of each beam tightly controlled, but the overall on-target, beam-to-beam intensities must be carefully balanced. Simulations indicate that the root-mean-square (rms) intensity balance on target should be <1% (Ref. 1). Depending on the amount of overlap between the beams, this requirement implies that the focal-spot intensities of each of OMEGA's 60 beams must achieve an rms balance of 2% to 3%.

To meet this specification, much attention has been paid to the power balancing (i.e., energy/unit time) of each of OMEGA's 60 beams at the laser output.[2] Through a balancing of gains, losses, and frequency conversion, OMEGA now consistently delivers an rms power balance that meets the 2% to 3% specification. As stated above, however, the quantity of importance to experiments is the *on-target intensity* balance. To characterize the intensity balance, one must also measure the on-shot focal spot of each beam at the target. Up until now, OMEGA has had the ability to characterize the on-shot focal spot of four beams (one at a time) at an equivalent target plane (ETP) located upstream of the target chamber. The ETP provides a detailed analysis of a single-beam focal spot, but it cannot provide an assessment of intensity balance on target. In addition, since the ETP pickoff is upstream of the target chamber, any effects caused by nonlinearities in the final focusing optics (located on the target chamber) are not characterized.

To characterize actual on-shot conditions, LLE has built a full-beam-in-tank (FBIT) diagnostic that measures the OMEGA focal spot at the center of the target chamber (TCC). The FBIT diagnostic picks off a full-aperture, low-energy sample of the beam after it has been transmitted through most of the final optics assembly. Specifically [see Fig. 1(a)], the standard plane-parallel, antireflective (AR)-coated vacuum window is replaced with an uncoated window with a small wedge (7.5 arcmin). The 3.7% reflection from the back surface of this wedge provides a low-energy sample of the main beam. This sample beam creates a sequence of forward-going replica beams, each having an intensity that is $(0.037)^2$ times that of the previous replica.

As shown in Fig. 1(b), each of the replicas comes to a focus at a different location in the target chamber. This provides a region near the TCC, where one of the replicas can be intercepted and delivered to a camera. The OMEGA target chamber contains several ports for instruments that are used to diagnose a particular experiment. Six of these ports contain ten-inch–manipulator (TIM) platforms that provide a flexible means to insert different diagnostics into the target chamber while maintaining vacuum conditions. The FBIT diagnostic uses TIM's to insert a pickoff optic, imaging optics, and a charge-coupled–device (CCD) camera into the target chamber to capture one of the beam replicas from the wedged vacuum window.

(a)

DPP   FL   VW DS

37 arcmin

7.5 arcmin

G12529JR

(b)

Four uncoated reflections:
$500 \text{ J} \times (0.037)^4 = 0.94 \text{ mJ}$

Two uncoated reflections:
$500 \text{ J} \times (0.037)^2 = 680 \text{ mJ}$

Four-wedge reflections
Two-wedge reflections
Main beam (0 reflections)
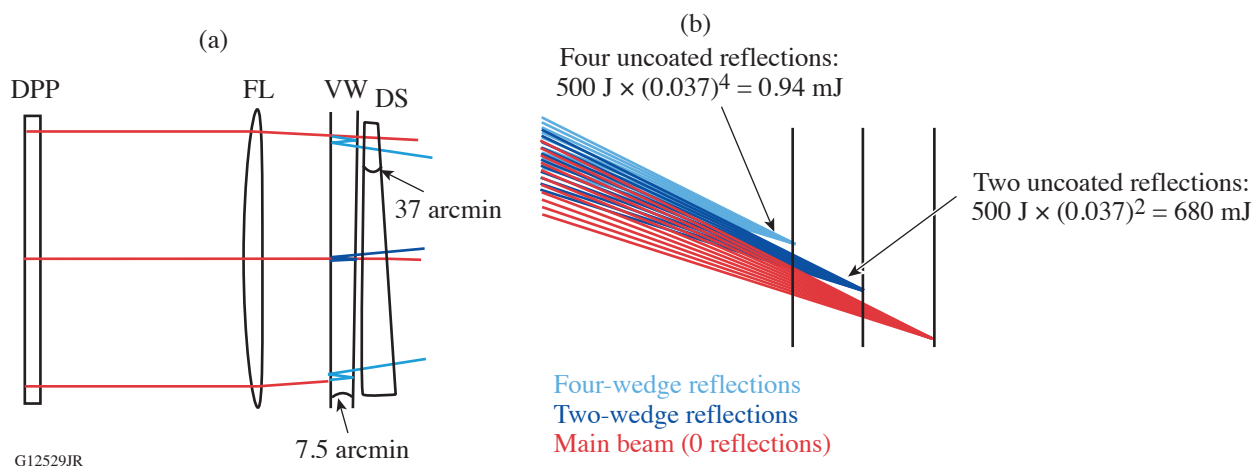
Figure 1

(a) Diagram of the final optics assembly used for the full-beam-in-tank (FBIT) diagnostic. For clarity, wedges are exaggerated and some of the reflections have been omitted. (b) The uncoated wedged vacuum window creates a series of replicas of the main beam. Each is reduced in intensity by 0.037^n, where n is the number of reflections in the wedge. Each replica focuses at a different location in the target chamber. DPP: distributive phase plate, FL: focus lens, VW: vacuum window, DS: debris shield.

One of the key requirements for any focal-spot diagnostic is that it does not introduce significant optical distortions so that the measured focal spot is an accurate representation of the actual spot. The wedged vacuum window provides an excellent method for sampling the beam near the target, but a focusing beam that makes multiple passes through a wedged optic is significantly aberrated. To mitigate this, the aberrations from the wedge are compensated by introducing an opposing wedge (37 arcmin) in the debris shield [see Fig. 1(a)]. In addition to the wavefront introduced by four passes through the wedged vacuum window, there are also manufacturing errors that will further degrade the focal-spot quality. With four reflections from the vacuum window surfaces, a high-quality reflected and transmitted wavefront is required. The achieved reflected and transmitted wavefront for the vacuum window was of the order of 0.06 waves ($\lambda = 632.8$ nm), which results in minimal additional distortion of the focal spot from manufacturing. Figure 2(a) shows a simulated focal spot for a diffraction-limited input. Included in this simulation are the measured reflected and transmitted wavefront of a manufactured wedged vacuum window and the measured transmitted wavefront of a manufactured compensating debris shield, showing that the system can be built with minimal distortion to the incoming beam (the yellow circle represents 12× the diffraction limit, which roughly corresponds to the OMEGA focal-spot size). Figure 2(b) shows an on-shot measurement of the OMEGA focal spot made by the FBIT diagnostic. The measured focal spot is significantly more aberrated than the spot predicted from just the aberrations of the FBIT itself. To ensure that the FBIT diagnostic will provide an accurate measurement of the focal spot, we have characterized each of the wedged vacuum window/debris-shield combinations. Figure 2(c) shows the predicted focal spot for a diffraction-limited input to the combination with the largest measured aberrations. While this predicts significantly more degradation to the focal-spot quality, this effect is still overwhelmed by the system aberrations [see Fig. 2(d)].

We have presented the design and implementation of an on-shot, on-target focal-spot diagnostic for the OMEGA Laser System. To our knowledge, this is the first diagnostic capable of measuring the on-shot focal spot of a large laser system inside the target chamber. The diagnostic makes use of an uncoated, wedged vacuum window to create reduced energy replicas of the main beam. One of these replicas is captured by a TIM-based instrument and relay imaged to a CCD camera. We have measured on-shot far fields and near fields and are working to characterize at least 30 beams during this fiscal year. These data will provide an estimate of the on-shot laser uniformity on target.
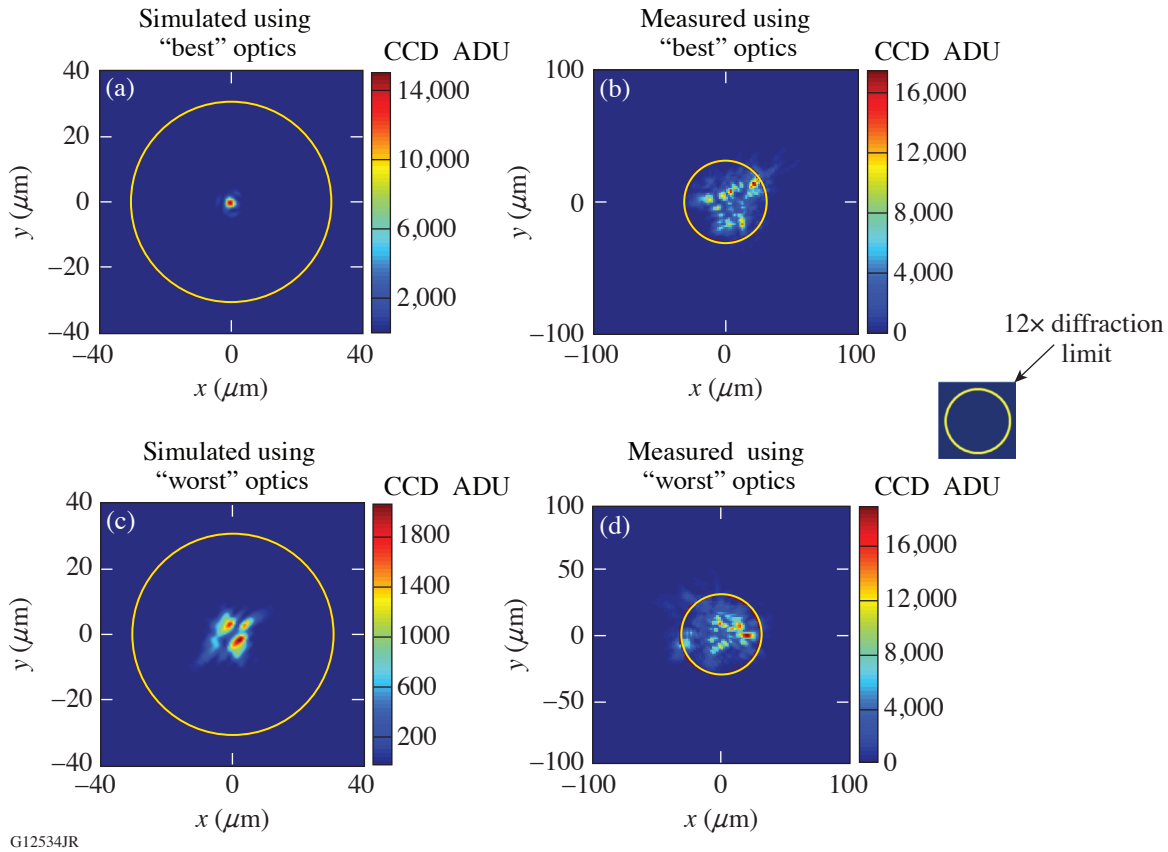
Figure 2

(a) Predicted FBIT-measured focal spot using the wedged vacuum window/wedged debris-shield combination with the "best" optical quality (using a diffraction-limited input to the final optics assembly). (b) FBIT measurement of the on-shot OMEGA focal spot using this combination of optics to generate the replica beam. (c) Predicted FBIT-measured focal spot using the wedged vacuum window/wedged debris-shield combination with the "worst" optical quality (using a diffraction-limited input to the FBIT). (d) FBIT measurement of the on-shot OMEGA focal spot using this "worst" combination of optics to generate the replica beam. The yellow circle represents a 12× diffraction-limited focal-spot size. ADU: Analog-to-digital units.

1. V. N. Goncharov *et al.*, Plasma Phys. Control. Fusion **59**, 014008 (2017).

2. S. Sampat *et al.*, Appl. Opt. **57**, 9571 (2018).

Comparison of On-Shot, In-Tank, and Equivalent-Target-Plane Measurements of the OMEGA Laser System Focal Spot

K. A. Bauer, M. Heimbueger, S. Sampat, L. J. Waxer, E. C. Cost, J. H. Kelly, V. Kobilansky, J. Kwiatkowski, S. F. B. Morse, D. Nelson, D. Weiner, G. Weselak, and J. Zou

Laboratory for Laser Energetics, University of Rochester

Target-physics simulations indicate that on-target uniformity of the OMEGA Laser System[1] of the order of 1% rms is required for each 100-ps interval of a cryogenic target implosion pulse shape.[2] Current laser diagnostic systems on OMEGA, located upstream of the target chamber, characterize the on-shot energy and temporal profile of all 60 beams at the output of the laser. In addition, there is the capability to characterize both the UV near field and the equivalent-target-plane (ETP) focal spot of a single beam. These two diagnostics use a 4% pickoff beam, located upstream of the final optics assembly, near the output of the frequency-conversion crystals. Combining the data from all of these diagnostics suggests that the beam-to-beam uniformity is sufficient to nearly meet this requirement.[3] Conversely, the results from implosion experiments suggest that the on-target uniformity is worse than the diagnostics measure. To resolve this discrepancy, we have recently developed the full-beam-in-tank (FBIT) diagnostic, which is capable of measuring the on-shot, on-target focal spot of multiple beams inside the OMEGA target chamber.[4] FBIT has the ability to directly characterize the on-shot near field and far field of multiple beams in the target chamber. FBIT uses a small sample of the full-energy beam inside the target chamber to analyze the beam separately from the light that hits the target. The main portion of the beam crosses target chamber center (TCC) and is terminated at a calorimeter in the opposing port so the on-target fluence (J/cm^2) of the beam can be calculated. Since FBIT directly measures the focal spot in the target chamber, we can analyze the fluence of each beam, which can be used in combination with data from OMEGA temporal diagnostics to investigate intensity (power per unit area) balance.

To meet the uniformity requirements for target implosion experiments, a smoothed far-field focal spot, with a size comparable to that of the target, is necessary. A distributed phase plate (DPP),[5] a distributed polarization rotator (DPR),[6] and smoothing by spectral dispersion (SSD)[7,8] all contribute to meeting the uniformity specifications. Using FBIT, we can study the individual effects on the focal spot of each of these in turn.

Figure 1 shows the evolution of the OMEGA focal spot as the single-beam uniformity improves. First we show the raw OMEGA far-field spot [Fig. 1(a)]; then a DPP is inserted at the input to the focus lens [Fig. 1(b)], which redistributes the spatial phase of the beam, effectively reducing the coherence across the beam. Next, SSD modulation is applied in one dimension [Fig. 1(c)], followed by both dimensions [Fig. 1(d)]. Finally, the DPR is added to the system [Fig. 1(e)] to increase the smoothing on target.

These images show the on-shot effect of each optic on the focal spot in the target chamber, measurements that were previously unavailable prior to FBIT. Images of multiple beamlines that include 2-D SSD and a DPR show similar results (Fig. 1 data were taken in Beamline 56). We can fit the azimuthal average of the beam profiles of each beamline to estimate the width of the profile, an example of which is shown in Fig. 2. The fit shows $1/e$ R_0 values of approximately 360 μm, which is very close to the designed spot size of the DPP's.

G12523JR
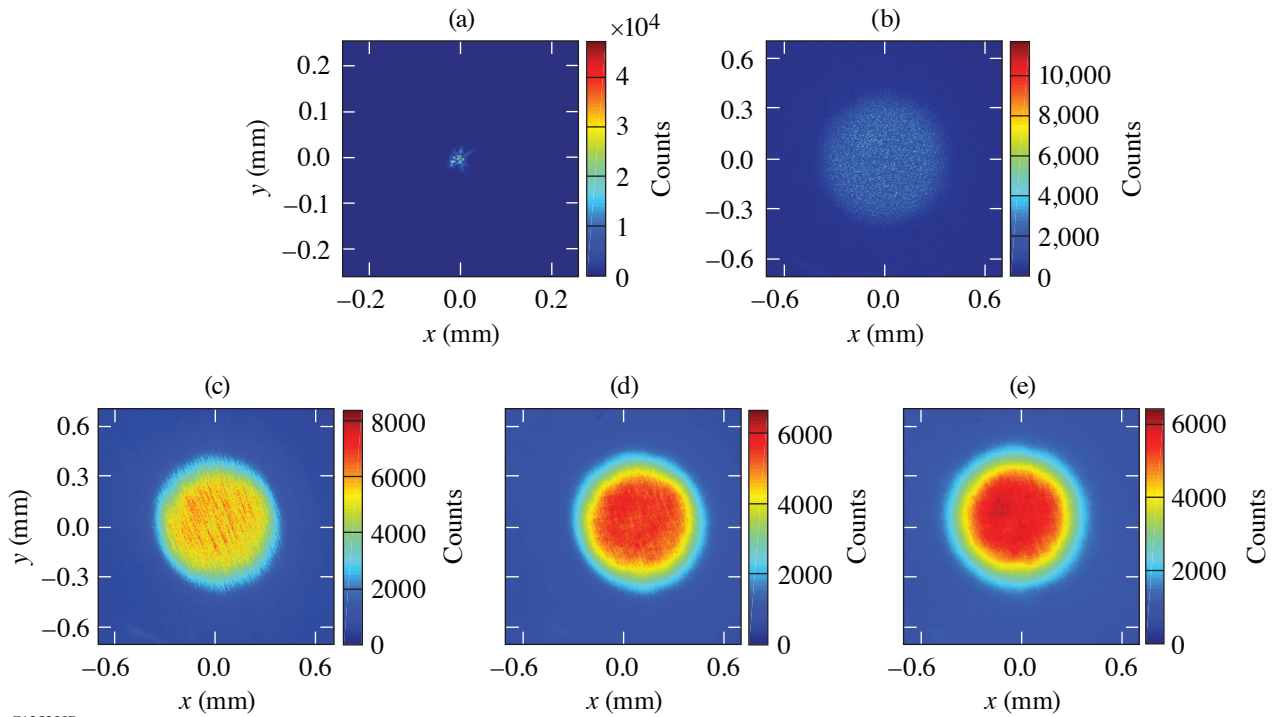
Figure 1
Evolution of the SSD focal spot, as seen from FBIT: (a) raw OMEGA far-field focal spot; (b) OMEGA far-field focal spot with a DPP; (c) focal spot with a DPP and 1-D SSD modulation; (d) focal spot with a DPP and 2-D SSD modulation; (e) focal spot with a DPP, 2-D SSD, and a DPR. Note that (a) is plotted on a different spatial scale to better show the far-field spot.

G12597JR
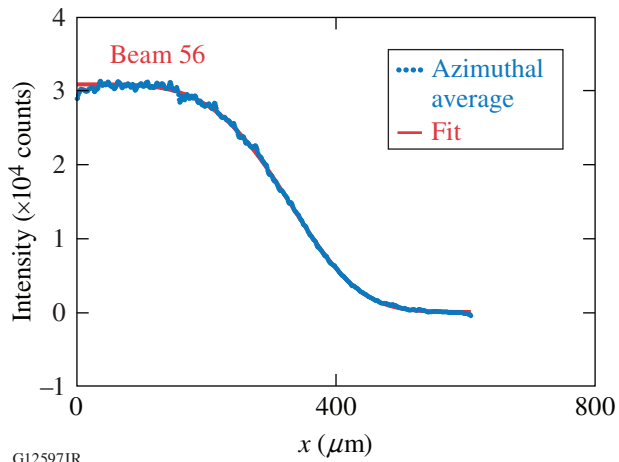
Figure 2
A super-Gaussian fit is used on the azimuthal average of the DPP far-field focal spot with 2-D SSD and a DPR.

We demonstrate the wide array of data that the new FBIT diagnostic is able to obtain. We can compare the focal spot from multiple beamlines easily within a shot cycle, analyze the SSD kernel, and characterize the effect of polarization smoothing on the focal spot. Using this data, we can more effectively understand the limitations of other diagnostics in the OMEGA Laser System and improve existing simulations of the laser performance on target. The preliminary data shown in Ref. 9 suggest that the upstream diagnostics compare closely with results found by using the FBIT diagnostic.

1. T. R. Boehly *et al*., Opt. Commun. **133**, 495 (1997).

2. S. Skupsky and R. S. Craxton, Phys. Plasmas **6**, 2157 (1999).

3. S. Sampat *et al*., Appl. Opt. **57**, 9571 (2018).

4. L. J. Waxer *et al*., Proc. SPIE **10898**, 108980F (2019).

5. *LLE Review Quarterly Report* **33**, 1, Laboratory for Laser Energetics, University of Rochester, Rochester, NY, LLE Document No. DOE/DP/40200-65 (1987).

6. *LLE Review Quarterly Report* **45**, 1, Laboratory for Laser Energetics, University of Rochester, Rochester, NY, LLE Document No. DOE/DP40200-149 (1990).

7. S. P. Regan *et al*., J. Opt. Soc. Am. B **17**, 1483 (2000).

8. S. P. Regan *et al*., J. Opt. Soc. Am. B **22**, 998 (2005).

9. K. A. Bauer *et al*., Proc. SPIE **10898**, 108980G (2019).

Power Balance on the OMEGA 60-Beam Laser

S. Sampat, T. Z. Kosc, K. A. Bauer, M. H. Romanofsky, A. L. Rigatti, J. Kwiatkowski, R. D. Dean, W. R. Donaldson,
L. J. Waxer, R. Moshier, and J. H. Kelly

Laboratory for Laser Energetics, University of Rochester

Lasers that have multiple output beams can generate those beams by one of several methods: aperture division, amplitude division, and temporal division (multiplexing). The generated beams are often further amplified, frequency converted, and/or conditioned depending on the ultimate application. Inequalities in amplification, frequency conversion, or conditioning can lead to differences in the outputs of each of the beams, for which it can be difficult to compensate. This issue is termed "beam imbalance." For a multibeam laser, however, the quantification of the balance of the output beams is often the parameter used to assess laser performance. Balancing is performed by measuring the output properties such as energy, power, and/or intensity.

Energy balance requires that each beam's output have the same total energy without regard to either the spatial distribution or the temporal shape. Power balance requires that, in addition to energy balance, the instantaneous spatially integrated temporal shapes of the output beams match over some averaging time. A typical pulse shape used for cryogenic target implosion experiments on OMEGA is shown in Fig. 1(a). Typical beam-to-beam variations of the output pulse shape are shown in Fig. 1(b).

G12187JR
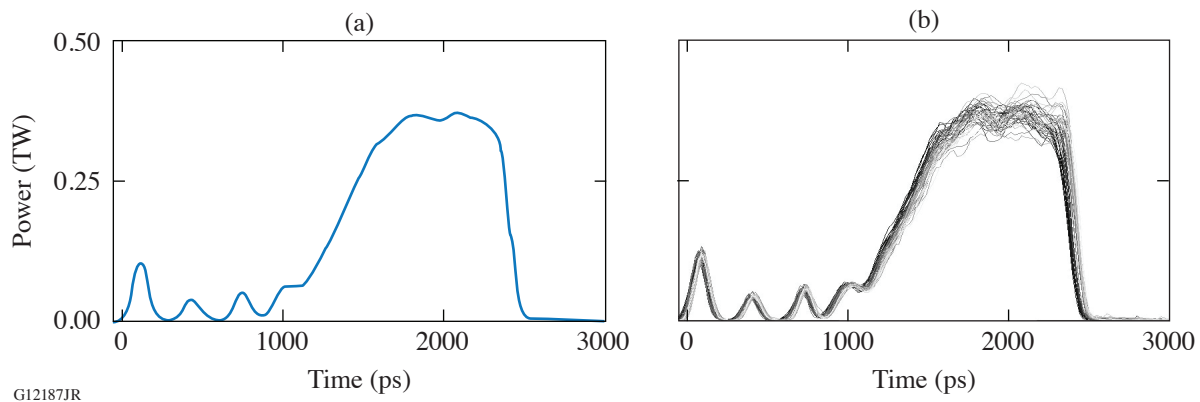
Figure 1

(a) Typical pulse shape used for cryogenic target implosion experiments on OMEGA containing three pickets followed by a drive. (b) The depicted pulse shape has an energy imbalance of 3.5% across 60 beams; the picket and drive have a power imbalance of 2.5% and 3.5% rms, respectively.

The power-balance requirement on OMEGA, as defined by an rms energy computation across 60 beams, is predicated on inertial confinement fusion target-physics simulations that indicate that a less than 1% rms power imbalance is required over any 100-ps interval of the pulse.[1] The near-term goal is to improve the first picket power balance to 1% rms imbalance while simultaneously reducing the drive imbalance. Power balance is sensitive to several factors that are less significant when assessing system energy balance. Given OMEGA's architecture that uses a single "seed" beam to generate 60 beams via splitting and subsequent amplification, choosing the appropriate amplifiers to compensate for any incidental losses on the system is paramount.

Since OMEGA's beamlines consist of amplifiers with varying degrees of saturation, a particular beam's square pulse distortion (SPD) can be significantly impacted by improper management of a saturating amplifier's gain.

A graphic with a simulation of this phenomenon is shown in Fig. 2. In Figs. 2(a) and 2(b), the black curve represents an IR pulse at the input of a different saturating amplifier. The blue and green curves are the pulse at the output of that amplifier. In both cases, a positive voltage offset has been applied to the amplifier's nominal voltage, thereby increasing its linear gain. Figure 2(a) shows the effect of increasing linear gain on the pulse shape in an amplifier where F_{out}/F_{sat} is low and, therefore, the pulse shape is not significantly affected. On OMEGA, disk amplifier stages E and F operate under this regime. Figure 2(b) shows the effect of increasing linear gain in a heavily saturated amplifier. Here, the effect of a voltage change is expected to have a stronger impact on pulse shape. On OMEGA, the stage-D amplifiers operate under this heavily saturated regime.

G12527JR
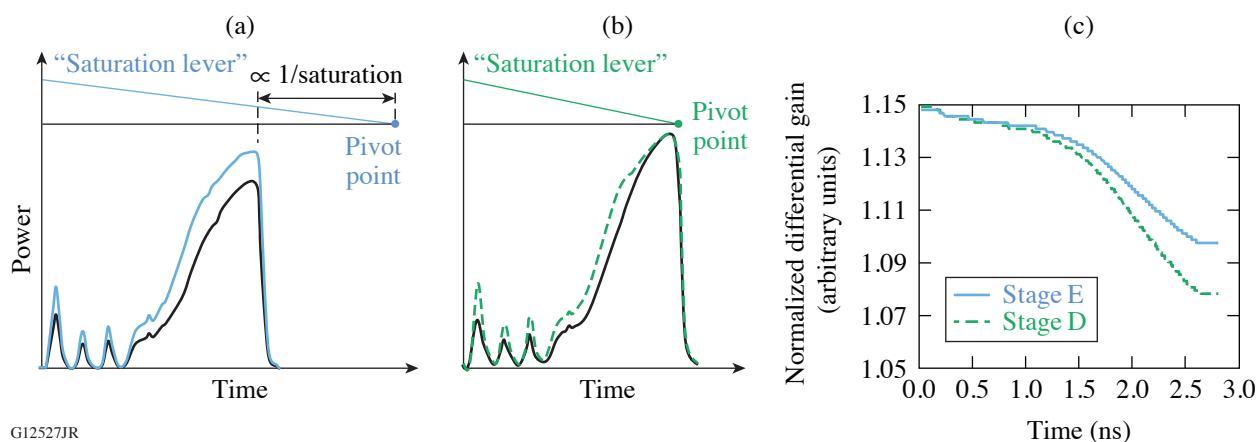
Figure 2
[(a),(b)] The black curve shows the same pulse simulated at the output of the stage-E disk and stage-D rod amplifiers, respectively. The blue and green curves show the change in the pulse shape resulting from a positive offset applied to the amplifier's operating voltage. (a) A uniform decrease in pulse power. (b) The effect of saturation results in a pronounced change in pulse power at the beginning of the pulse and almost no change at the back end of the pulse that experiences saturated gain. (c) A direct measure of the change in pulse shape showing the ratio of the nominal pulse to the gain-reduced pulse.

The "saturation lever" is a visual depiction of the aforementioned effect of operating in different saturation regimes and how gain manipulation of different saturating amplifiers can result in a more-pronounced effect on SPD and, thereby, power balance on the system. The location of the saturation lever pivot point with respect to the back of the pulse is dependent exclusively on the ratio of the output fluence to the saturation fluence of any given amplifier. In Fig. 2, vertical displacement of the end opposing the pivot point of the saturation lever represents a positive change in the amplifier's flash-lamp capacitor bank voltage.

Recent target-physics simulations have suggested that temporal simultaneity in the arrival of the ramp on the drive portion of the pulse shape [$t \sim 1400$ ps in Fig. 1(b)] governs implosion dynamics to a large degree. This region of the pulse can be manipulated by systematically adjusting the gain of the stage-D rod amplifiers, which affects the SPD more than the stage-E and -F amplifiers. This effort is currently being simulated in Miró and is planned for experimental testing in the near future.

1. V. N. Goncharov *et al.*, Plasma Phys. Control. Fusion **59**, 014008 (2017).

FY19 Q1 Laser Facility Report

J. Puth, M. Labuzeta, D. Canning, and B. E. Kruschwitz

Laboratory for Laser Energetics, University of Rochester

During the first quarter (Q1) of FY19, the Omega Laser Facility conducted 331 target shots on OMEGA and 204 target shots on OMEGA EP for a total of 535 target shots (see Tables I and II). OMEGA averaged 11 target shots per operating day, averaging 94.4% Availability and 98.0% Experimental Effectiveness.

OMEGA EP was operated extensively during Q1 of FY19 for a variety of user experiments. OMEGA EP averaged 8.5 target shots per operating day, averaging 93.8% Availability and 92.9% Experimental Effectiveness.

Table I: OMEGA Laser System target shot summary for Q1 FY19.

Laboratory/ Program	Planned Number of Target Shots	Actual Number of Target Shots	ICF	Shots in Support of ICF	Non-ICF
CEA	16.5	18	—	—	18
HED	99	112	—	—	112
LBS	5.5	7	—	—	7
LLE	82.5	75	—	75	—
LLNL	5.5	8	8	—	—
NLUF	38.5	46	—	—	46
Calibration	0	65	—	65	—
Total	247.5	331	8	140	183

Table II: OMEGA EP Laser System target shot summary for Q1 FY19.

Laboratory/ Program	Planned Number of Target Shots	Actual Number of Target Shots	ICF	Shots in Support of ICF	Non-ICF
HED	63	86	—	—	86
LBS	7	8	—	—	8
LLE	21	23	—	23	—
LLNL	7	15	15	—	—
NLUF	49	56	—	—	56
NRL	7	10	10	—	—
Calibration	0	6	—	6	—
Total	154	204	25	29	150

Sub-aperture short-pulse beam operation has been activated on OMEGA EP. This modifies the nominally *f*/2 square beam (measured along the diagonal) to an *f* number that suits a given experimental objective. Circular *f*/6, *f*/8, and *f*/10 profiles are currently available and additional profiles could be realized with modest effort. Kinematic nesting of the apodizers enables rapid shot-to-shot configuration from one *f* number to another. Energy limits are naturally decreased proportional to beam area. This capability has been successfully employed to investigate wakefield electron acceleration and plasma lens concepts.

Experimental Validation of Low-Z Ion-Stopping Formalisms Around the Bragg Peak in High-Energy-Density Plasmas

J. A. Frenje,[1] R. Florido,[2] R. C. Mancini,[3] T. Nagayama,[4] P. E. Grabowski,[5] H. G. Rinderknecht,[6] H. Sio,[1] A. Zylstra,[7] M. Gatu Johnson,[1] C. K. Li,[1] F. H. Séguin,[1] R. D. Petrasso,[1] V. Yu. Glebov,[6] and S. P. Regan[6]

[1]Plasma Science and Fusion Center, Massachusetts Institute of Technology
[2]iUNAT– Departamento de Física, Universidad de Las Palmas de Gran Canaria, Spain
[3]Physics Department, University of Nevada, Reno
[4]Sandia National Laboratories
[5]Lawrence Livermore National Laboratory
[6]Laboratory for Laser Energetics, University of Rochester
[7]Los Alamos National Laboratory

An understanding of the DT-α energy deposition and heating of a high-energy-density (HED) plasma is critical for determining the ignition threshold in hot-spot–ignition experiments. This requires a fundamental understanding of the DT-α stopping around the Bragg peak, where the ion velocity (v_i) is similar to the average velocity (v_{th}) of the thermal plasma electrons for a wide range of electron (T_e) and ion temperatures (T_i), and electron number densities (n_e). Ion stopping in HED plasmas has, therefore, been subject to extensive analytical and numerical studies for decades,[1–3] but a theoretical treatment of ion stopping especially around the Bragg peak remains a difficult problem. The consensus is that the ion stopping at $v_i \gg v_{th}$ is treated well by the Born approximation because the interaction between the fast ions and plasma electrons is small, resulting in small energy transfers compared to the kinetic energy of the ions. At $v_i < v_{th}$, the ion stopping is harder to characterize but generally described by collisional theories that treat two-body collisions and large-angle scattering between the ions and plasma electrons. At ion velocities near v_{th}, the Born approximation breaks down because scattering is no longer weak and collisional theories make it difficult to provide a complete, self-consistent picture of the ion stopping because of the dynamic dielectric response of the plasma electrons. Rigorous quantum mechanical treatments based on convergent kinetic theories[1] attempt to rectify these challenges by utilizing the strengths of the different approaches applied to the different regimes; however, it is not clear how best to combine them and quantify their errors. Precise measurements of the ion stopping around the Bragg peak are therefore essential to guide the theoretical efforts.

Although numerous efforts have been made to theoretically describe the behavior of ion stopping in HED plasmas, only a limited set of experimental data exists to test these theories. In addition, most of these experiments used only one particle with a distinct velocity in the high-velocity ion-stopping regime ($v_i > v_{th}$) and, therefore, did not simultaneously probe the detailed characteristics of the Bragg peak below and above v_{th}. To the best of our knowledge, only two experiments have attempted to simultaneously probe the low- and high-velocity side of the Bragg peak,[4,5] but the limitation of these experiments was that the HED plasma conditions could not be characterized to the level required for experimental validation of various ion-stopping formalisms. The work described here significantly advances previous efforts by providing the first accurate experimental validation of ion-stopping formalisms around the Bragg peak.

The experiments reported herein were carried out on OMEGA, where eight D^{3}He gas-filled, thin-glass capsules were symmetrically imploded with 60 laser beams, delivering up to 12.0 kJ to the capsule in a 1-ns square pulse. These capsules were also filled with a small amount of argon for a time- and space-resolved measurement of the electron-temperature and electron-number-density profiles.[6]

For accurate experimental validation of the ion stopping around the Bragg peak, the energy loss ($-\Delta E_i$) of DD tritons (DD-t), DD protons (DD-p), $D^3He-\alpha$ ($D^3He-\alpha$), and D^3He protons (D^3He-p), while traversing the well-characterized HED-plasma conditions, were simultaneously measured. Examples of measured spectra of DD-t, DD-p, $D^3He-\alpha$, and D^3He-p are shown in Fig. 1 for shot 75699. The vertical arrows in Fig. 1 indicate the median energy for each measured spectrum, and by contrasting these energies to the average-birth energies (vertical dashed lines), $-\Delta E_i$ was determined to an accuracy of ~10% and used to assess the ion stopping in the HED plasma. (See Ref. 7 for more details about these measurements.)

U2472JR
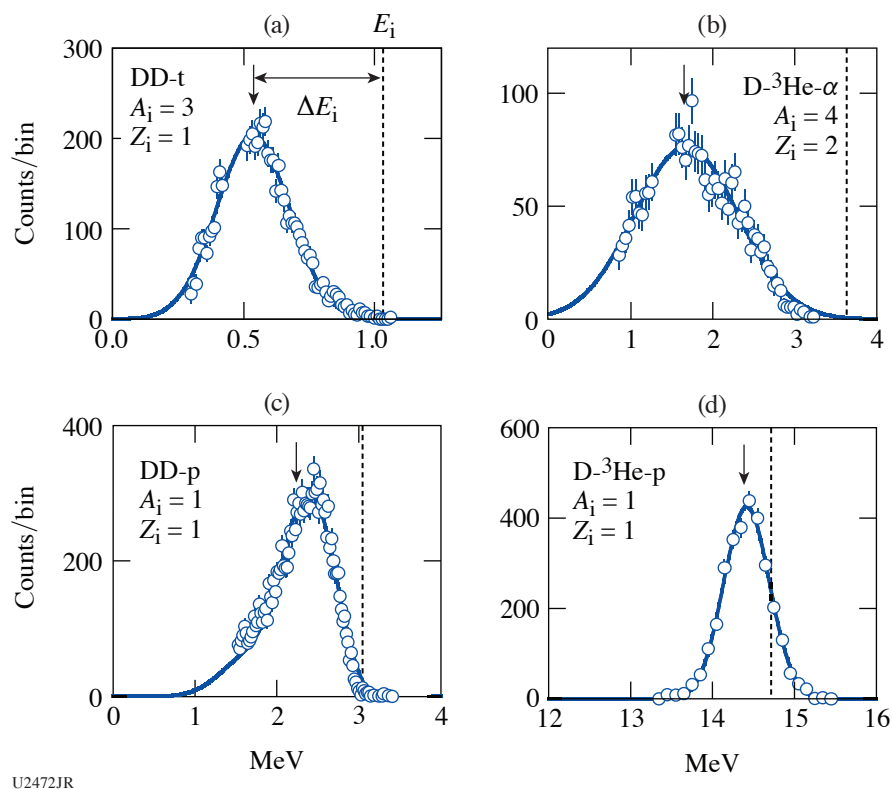
Figure 1
Measured spectra of DD-t, $D^3He-\alpha$, DD-p, and D^3He-p for shot 75699. These fusion products are produced by the reactions: $D + D \longrightarrow t$ (1.01 MeV) + p (3.02 MeV) and $D + {}^3He \longrightarrow {}^4He$ (3.71 MeV) + p (14.63 MeV), where the energies in the parentheses are the fusion-product birth energies (at zero ion temperature).

To illustrate the measured energy loss of fusion products with different initial energy (E_i), charge (Z_i), and mass (A_i) passing through an HED plasma, the energy-loss data must be presented in the form of $-\Delta E_i / Z_i^2$ versus E_i / A_i. Figure 2 shows the $-\Delta E_i / Z_i^2$ versus E_i / A_i for shots conducted in this study. The solid curves in Fig. 2 were obtained by integrating the Brown–Preston–Singleton (BPS) plasma stopping-power function, describing only the ion–electron Coulomb interaction. Clearly, the data demonstrate that the BPS formalism is providing a good description of the ion stopping for these HED plasma conditions, except for the stopping of DD-t at $v_i \sim 0.3 v_{th}$. At this velocity, the BPS formalism systematically underpredicts DD-t energy loss for all shots. This observation cannot be explained by the inclusion of ion–ion Coulomb scattering in the modeling because ion-stopping theories based on multi-ion component response predict that the contribution of the ion–ion Coulomb scattering to the total DD-t plasma-stopping power is ~10% at $v_i \sim 0.3 v_{th}$. This points to the idea that the contribution from the ion–ion component to the total ion stopping at this velocity could, in fact, be larger than predicted by theories. This is certainly plausible

since all theories ignore the ion–ion nuclear elastic scattering, which is more strongly weighted toward large-angle scattering than Coulomb scattering. To explain the data at $v_i \sim 0.3 v_{th}$, the total ion stopping must be increased by $\sim$20%, possibly a result of ion–ion nuclear elastic scattering. This postulation, if correct, would have an impact on our understanding of DT-α heating of the fuel ions in an ignition experiment.
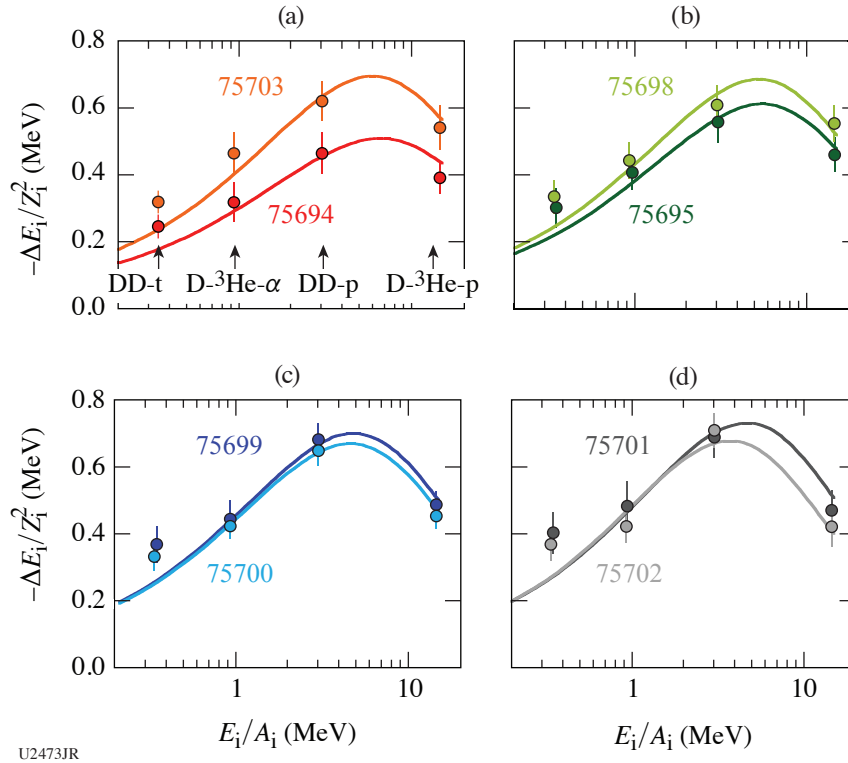
Figure 2

The measured and predicted ion stopping $\left(-\Delta E_i \big/ Z_i^2\right)$ as a function of $E_i \big/ A_i$ for all shots. The data set is contrasted to BPS predictions (considering only ion–electron Coulomb interactions).

1. L. S. Brown, D. L. Preston, and R. L. Singleton, Jr., Phys. Rep. **410**, 237 (2005).

2. C.-K. Li and R. D. Petrasso, Phys. Rev. Lett. **70** 3059 (1993); **114**, 199901(E) (2015).

3. G. Maynard and C. Deutsch, J. Phys. France **46**, 1113 (1985).

4. D. G. Hicks *et al.*, Phys. Plasmas **7**, 5106 (2000).

5. J. A. Frenje *et al.*, Phys. Rev. Lett. **115**, 205001 (2015).

6. T. Nagayama *et al.*, Phys. Plasmas **21**, 050702 (2014).

7. J. A. Frenje *et al.*, Phys. Rev. Lett. **122**, 015002 (2019).

Probing Fuel-Ion Species Dynamics in Shock-Driven Inertial Confinement Fusion Implosions Using Multiple Reaction Histories

H. Sio,[1] J. A. Frenje,[1] A. Le,[2] S. Atzeni,[3] T. J. T. Kwan,[2] M. Gatu Johnson,[1] G. Kagan,[2] C. Stoeckl,[4] C. K. Li,[1] C. E. Parker,[1] C. J. Forrest,[4] V. Yu. Glebov,[4] N. V. Kabadi,[1] A. Bose,[1] H. G. Rinderknecht,[4] P. A. Amendt,[5] D. T. Casey,[5] R. C. Mancini,[6] W. T. Taitano,[2] B. Keenan,[2] A. N. Simakov,[2] L. Chacón,[2] S. P. Regan,[4] T. C. Sangster,[4] E. M. Campbell,[4] F. H. Séguin,[1] and R. D. Petrasso[1]

[1]Plasma Science and Fusion Center, Massachusetts Institute of Technology
[2]Los Alamos National Laboratory
[3]Dipartimento SBAI, Università degli Studi di Roma "La Sapienza," Italy
[4]Laboratory for Laser Energetics, University of Rochester
[5]Lawrence Livermore National Laboratory
[6]Physics Department, University of Nevada, Reno

Strong shocks are ubiquitous in inertial confinement fusion (ICF) and many astrophysical plasmas,[1] and the experimental results described in this work may provide new insights into phenomena in these fields. ICF produces thermonuclear fusion in the laboratory by imploding a spherical target filled with light-ion fuel, and capsule compression begins with launching strong shock(s) into the central gas during the shock phase. During this time, sharp gradients at the shock front are expected to drive temperature and density differences between the different fuel-ion (D, T, and ^{3}He) populations. These multi-ion effects that may impact and modify plasma conditions are not modeled in average-ion-fluid codes but are simulated in kinetic-ion simulations.

In contrast with previous studies that relied on time-integrated measurements, this work[2] presents time-resolved observation of fuel-ion species dynamics in ICF implosions using DT and D^{3}He reaction histories (Fig. 1). These reaction histories were measured with a particle x-ray temporal diagnostic (PXTD),[3] which captures the relative timing between these reaction histories with unprecedented precision (~10 ps). These time-resolved measurements are contrasted with average-ion-fluid *DUED* and multi-ion *LSP* simulations. The difference between the measured fusion reaction histories during the shock phase is consistent with rapidly changing fuel-ion composition caused by a strong shock in the central gas of an ICF target.
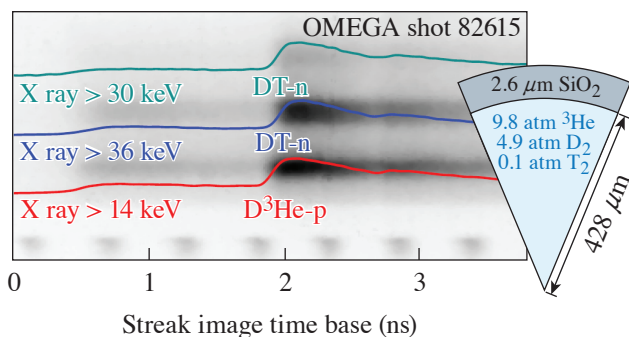
Figure 1
PXTD streak image on OMEGA shot 82615. The target is a thin-glass capsule filled with D^{3}He and a trace of T$_2$. PXTD measured both the x-ray emissions as well as the D^{3}He and DT reaction histories from the implosion.

This experiment uses an exploding-pusher platform,[4] which is simple and ideal for studying the multi-ion dynamics during the shock phase in an ICF implosion. The reason for this is that shock-phase plasma conditions (temperature, density, ion mean-free-path, shock strength) are similar in all these implosions. These exploding-pusher targets are 860 μm in diameter with a 2.7-μm-thick SiO_2 shell. The gas-fill density is 2.2 mg/cm^3, with an atomic fuel composition of 49.6% D, 49.7% ^{3}He, and 0.7% T. These targets are driven symmetrically by 60 laser beams on the OMEGA Laser System with a total energy of 14.4 kJ using a 0.6-ns-sq pulse shape. These implosions are hydrodynamic-like, with $\lambda_{ii}/R_{burn} \sim 3$, where λ_{ii} is the ion mean free path and R_{burn} is the fuel radius at peak burn.

The primary measurements in this experiment are the absolute DT and D^{3}He reaction histories, which are simultaneously measured with the PXTD (Fig. 1). This is done by measuring the time-arrival histories of the monoenergetic 14.1-MeV DT-n and 14.7-MeV D^{3}He-p as they escape the implosion. Since all measurements are made with the same diagnostic, the relative timing uncertainty between the DT and D^{3}He reaction histories is ~10 ps (versus ~40 to 50 ps, with the standard method of cross-timing between two stand-alone diagnostics). This innovation is crucial to capturing the relative timing between different nuclear burns with sufficiently high precision to enable meaningful comparison between measurements and simulations. In comparison with the average-ion-fluid *DUED*[5] simulation (Fig. 2), a significantly higher D^{3}He reaction rate is observed relative to DT at the onset of the shock burn. This is observed on all four shots, and higher-than-expected ion temperature alone early in time in the fuel cannot explain this observation.

U2475JR
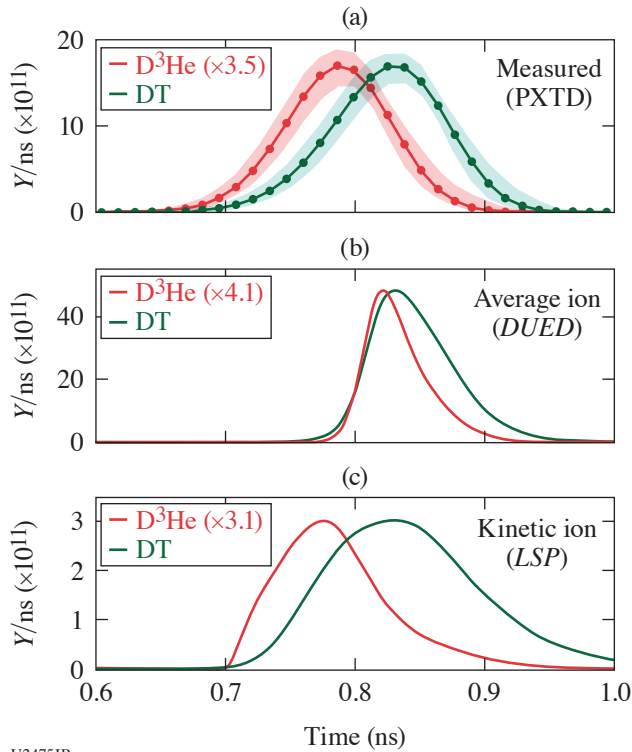
Figure 2

Absolute D^{3}He (red) and DT (blue) reaction histories measured by PXTD and simulated by *DUED* and *LSP*, for OMEGA shot 82615. The magnitudes of the D^{3}He histories are scaled to match the DT histories for clarity in each case. Uncertainties in the PXTD data are indicated by the shaded regions.

The measured timing difference is consistent, however, with ion-species separation driven by sharp pressure gradients at the shock front in the implosion. The dominant terms driving the D and ^{3}He ions forward relative to the T ions are from the ion pressure gradient (barodiffusion,[6] which accelerates the lighter D ions ahead) and the electron pressure gradient (electrodiffusion,[7] which accelerates the higher-charge ^{3}He ions ahead).

Fuel-ion–species separation is also observed in a kinetic-ion *LSP*[8] simulation, which, unlike the average-ion-fluid code *DUED*, treats the D, T, and ^{3}He ion population separately. During shock convergence, fuel-ion–species separation has already developed between the D, T, and ^{3}He ions, with the T ions lagging behind the shock front. This led to a depletion of T ions on the central fuel region when the shock rebounds, delaying the DT burn relative to the D^{3}He burn. Qualitatively, *LSP* simulations clearly demonstrate how fuel-ion–species separation that developed during shock propagation and rebound manifest as a timing differential between reaction histories (Fig. 2).

In summary, the time-resolved DT and D^{3}He reaction rates in hydrodynamic-like shock-driven implosions cannot be explained by average-ion simulations and is attributed to ion-species separation between the D, T, and ^{3}He ions during shock convergence and rebound. At the onset of the shock burn, the ^{3}He/T fuel ratio in the burn region inferred from the measured reaction histories is much higher as compared to the initial ^{3}He/T gas-fill ratio. Since T and ^{3}He have the same mass but a different charge, these results indicate that the charge-to-mass ratio plays an important role in driving fuel-ion–species separation during strong shock propagation. It is unclear how these multi-ion effects affect implosion performance during the deceleration and compression phase since existing experimental results have been mixed. A planned upgrade to the PXTD diagnostic (the cryoPXTD) will provide improved nuclear and x-ray data for these implosion experiments, as well as time-resolved electron temperature measurement for the OMEGA cryogenic program. Future work includes quantifying these effects in very hydrodynamic shock-driven implosions; in very kinetic implosions; in the ablative phase of compressive implosions; and in astrophysical settings such as SN 1987a (Ref. 1), where nonequilibrium kinetic effects and signatures (such as temperature differences between ion species) could be present.

1. S. Q. Park *et al*., Astrophys. J. **610**, 378 (2004).

2. H. Sio *et al*., Phys. Rev. Lett. **122**, 035001 (2019).

3. H. Sio *et al*., Rev. Sci. Instrum. **87**, 11D701 (2016).

4. M. J. Rosenberg *et al*., Phys. Rev. Lett. **112**, 185001 (2014).

5. S. Atzeni *et al*., Comput. Phys. Commun. **169**, 15 (2005).

6. P. Amendt *et al*., Phys. Rev. Lett. **105**, 115005 (2010).

7. G. Kagan and X.-Z. Tang, Phys. Plasmas **19**, 082709 (2012).

8. D. R. Welch *et al*., Comput. Phys. Commun. **164**, 183 (2004).

Publications and Conference Presentations

Publications

R. Aboushelbaya, A. F. Savin, L. Ceurvorst, J. Sadler, P. A. Norreys, A. S. Davies, D. H. Froula, A. Boyle, M. Galimberti, P. Oliveira, B. Parry, Y. Katzir, and K. Glize, "Single-Shot Frequency-Resolved Optical Gating for Retrieving the Pulse Shape of High Energy Picosecond Pulses," Rev. Sci. Instrum. **89**, 103509 (2018).

F. Albert, N. Lemos, J. L. Shaw, P. M. King, B. B. Pollock, C. Goyon, W. Schumaker, A. M. Saunders, K. A. Marsh, A. Pak, J. E. Ralph, J. L. Martins, L. D. Amorim, R. W. Falcone, S. H. Glenzer, J. D. Moody, and C. Joshi, "Betatron X-Ray Radiation in the Self-Modulated Laser Wakefield Acceleration Regime: Prospects for a Novel Probe at Large Scale Laser Facilities," Nucl. Fusion **59**, 032003 (2019).

L. Berzak Hopkins, S. LePape, L. Divol, A. Pak, E. Dewald, D. D. Ho, N. Meezan, S. Bhandarkar, L. R. Benedetti, T. Bunn, J. Biener, J. Crippen, D. Casey, D. Clark, D. Edgell, D. Fittinghoff, M. Gatu-Johnson, C. Goyon, S. Haan, R. Hatarik, M. Havre, D. Hinkel, H. Huang, N. Izumi, J. Jaquez, O. Jones, S. Khan, A. Kritcher, C. Kong, G. Kyrala, O. Landen, T. Ma, A. MacPhee, B. MacGowan, A. J. Mackinnon, M. Marinak, J. Milovich, M. Millot, P. Michel, A. Moore, S. R. Nagel, A. Nikroo, P. Patel, J. Ralph, H. Robey, J. S. Ross, N. G. Rice, S. Sepke, V. A. Smalyuk, P. Sterne, D. Strozzi, M. Stadermann, P. Volegov, C. Weber, C. Wild, C. Yeamans, D. Callahan, O. Hurricane, R. P. J. Town, and M. J. Edwards, "Toward a Burning Plasma State Using Diamond Ablator Inertially Confined Fusion (ICF) Implosions on the National Ignition Facility (NIF)," Plasma Phys. Control. Fusion **61**, 014023 (2019).

E. G. Blackman and J. A. Tarduno, "Mass, Energy, and Momentum Capture from Stellar Winds by Magnetized and Unmagnetized Planets: Implications for Atmospheric Erosion and Habitability," Mon. Not. R. Astron. Soc. **481**, 5146 (2018).

A. Casner, C. Mailliet, G. Rigon, S. F. Khan, D. Martinez, B. Albertazzi, T. Michel, T. Sano, Y. Sakawa, P. Tzeferacos, D. Lamb, S. Liberatore, N. Izumi, D. Kalantar, P. Di Nicola,

J. M. Di Nicola, E. Le Bel, I. Igumenshchev, V. Tikhonchuk, B. A. Remington, J. Ballet, E. Falize, L. Masse, V. A. Smalyuk, and M. Koenig, "From ICF to Laboratory Astrophysics: Ablative and Classical Rayleigh–Taylor Instability Experiments in Turbulent-Like Regimes," Nucl. Fusion **59**, 032002 (2019).

Y. H. Ding, A. J. White, S. X. Hu, O. Certik, and L. A. Collins, "*Ab Initio* Studies on the Stopping Power of Warm Dense Matter with Time-Dependent Orbital-Free Density Functional Theory," Phys. Rev. Lett. **121**, 145001 (2018).

C. Dorrer and S.-W. Bahk, "Spatio-Spectral Characterization of Broadband Fields Using Multispectral Imaging," Opt. Express **26**, 33,387 (2018).

C. Dorrer and R. J. Brown, "Stable Low-Repetition-Rate Time-Lens Picosecond Seed Source," IEEE Photonics Technol. Lett. **30**, 1854 (2018).

C. Dorrer and J. Qiao, "Direct Binary Search for Improved Coherent Beam Shaping and Optical Differentiation Wavefront Sensing," Appl. Opt. **57**, 8557 (2018).

R. P. Drake, "A Journey Through High-Energy-Density Physics," Nucl. Fusion **59**, 035001 (2019).

R. P. Drake and F. W. Doss, "Regimes of the Vishniac–Ryu Decelerating Shock Instability," Astrophys. J. **868**, 23 (2018).

K. Engelhorn, T. J. Hilsabeck, J. Kilkenny, D. Morris, T. M. Chung, A. Dymoke-Bradshaw, J. D. Hares, P. Bell, D. Bradley, A. C. Carpenter, M. Dayton, S. R. Nagel, L. Claus, J. Porter, G. Rochau, M. Sanchez, S. Ivancic, C. Sorce, and W. Theobald, "Sub-Nanosecond Single Line-of-Sight (SLOS) X-Ray Imagers," Rev. Sci. Instrum. **89**, 10G123 (2018) (invited).

R. K. Follett, J. G. Shaw, J. F. Myatt, V. N. Goncharov, D. H. Edgell, D. H. Froula, and J. P. Palastro, "Ray-Based Modeling of Cross-Beam Energy Transfer at Caustics," Phys. Rev. E **98**, 043202 (2018).

W. Fox, J. Matteucci, C. Moissard, D. B. Schaeffer, A. Bhattacharjee, K. Germaschewski, and S. X. Hu, "Kinetic Simulation of Magnetic Field Generation and Collisionless Shock Formation in Expanding Laboratory Plasmas," Phys. Plasmas **25**, 102106 (2018).

L. Gao, B. F. Kraus, K. W. Hill, M. Bitter, P. Efthimion, M. B. Schneider, A. G. MacPhee, D. B. Thorn, J. Kilkenny, J. Ayers, R. Kauffman, H. Chen, and D. Nelson, "Absolute Calibration of a Time-Resolved High Resolution X-Ray Spectrometer for the National Ignition Facility," Rev. Sci. Instrum. **89**, 10F125 (2018) (invited).

M. Gatu Johnson, B. D. Appelbe, J. P. Chittenden, J. Delettrez, C. Forrest, J. A. Frenje, V. Yu. Glebov, W. Grimble, B. M. Haines, I. Igumenshchev, R. Janezic, J. P. Knauer, B. Lahmann, F. J. Marshall, T. Michel, F. H. Séguin, C. Stoeckl, C. Walsh, A. B. Zylstra, and R. D. Petrasso, "Impact of Asymmetries on Fuel Performance in Inertial Confinement Fusion," Phys. Rev. E **98**, 051201(R) (2018).

M. Gatu Johnson, J. Katz, C. Forrest, J. A. Frenje, V. Yu. Glebov, C. K. Li, R. Paguio, C. E. Parker, C. Robillard, T. C. Sangster, M. Schoff, F. H. Séguin, C. Stoeckl, and R. D. Petrasso, "Measurement of Apparent Ion Temperature Using the Magnetic Recoil Spectrometer at the OMEGA Laser Facility," Rev. Sci. Instrum. **89**, 10I129 (2018).

V. Yu. Glebov, M. J. Eckart, C. J. Forrest, G. P. Grim, E. P. Hartouni, R. Hatarik, J. P. Knauer, A. S. Moore, S. P. Regan, T. C. Sangster, D. J. Schlossberg, and C. Stoeckl, "Testing a Cherenkov Neutron Time-of-Flight Detector on OMEGA," Rev. Sci. Instrum. **89**, 10I122 (2018).

M. G. Gorman, A. L. Coleman, R. Briggs, R. S. McWilliams, D. McGonegle, C. A. Bolme, A. E. Gleason, E. Galtier, H. J. Lee, E. Granados, M. Śliwa, C. Sanloup, S. Rothman, D. E. Fratanduono, R. F. Smith, G. W. Collins, J. H. Eggert, J. S. Wark, and M. I. McMahon, "Femtosecond Diffraction Studies of Solid and Liquid Phase Changes in Shock-Compressed Bismuth," Sci. Rep. **8**, 16927 (2018).

P.-A. Gourdain, A. B. Sefkow, and C. E. Seyler, "The Generation of Warm Dense Matter Using a Magnetic Anvil Cell," IEEE Trans. Plasma Sci. **46**, 3968 (2018).

E. C. Hansen, D. H. Barnak, P.-Y. Chang, R. Betti, E. M. Campbell, J. R. Davies, J. P. Knauer, J. L. Peebles, S. P. Regan, and A. B. Sefkow, "Optimization of Laser-Driven Cylindrical Implosions on the OMEGA Laser," Phys. Plasmas **25**, 122701 (2018).

E. C. Hansen, P. Hartigan, A. Frank, A. Wright, and J. C. Raymond, "Simulating Radiative Magnetohydrodynamical Flows with ASTROBEAR: Implementation and Applications of Non-Equilibrium Cooling," Mon. Not. R. Astron. Soc. **481**, 3098 (2018).

D. R. Harding, M. J. Bonino, W. Sweet, M. Schoff, A. Greenwood, N. Satoh, M. Takagi, and A. Nikroo, "Properties of Vapor-Deposited and Solution-Processed Targets for Laser-Driven Inertial Confinement Fusion Experiments," Matter and Radiation at Extremes **3**, 312 (2018).

S. X. Hu, V. N. Goncharov, P. B. Radha, S. P. Regan, and E. M. Campbell, "Microphysics Studies for Direct-Drive Inertial Confinement Fusion," Nucl. Fusion **59**, 032011 (2019).

G. Kagan, O. L. Landen, D. Svyatskiy, H. Sio, N. V. Kabadi, R. A. Simpson, M. Gatu Johnson, J. A. Frenje, R. D. Petrasso, R. C. Shah, T. R. Joshi, P. Hakel, T. E. Weber, H. G. Rinderknecht, D. Thorn, M. Schneider, D. Bradley, and J. Kilkenny, "Inference of the Electron Temperature in Inertial Confinement Fusion Implosions from the Hard X-Ray Spectral Continuum," Contrib. Plasma Phys. **59**, 181 (2019).

A. Krygier, F. Coppari, G. E. Kemp, D. B. Thorn, R. S. Craxton, J. H. Eggert, E. M. Garcia, J. M. McNaney, H.-S. Park, Y. Ping, B. A. Remington, and M. B. Schneider, "Developing a High-Flux, High-Energy Continuum Backlighter for Extended X-Ray Absorption Fine Structure Measurements at the National Ignition Facility," Rev. Sci. Instrum. **89**, 10F114 (2018).

G. A. Kyrala, J. E. Pino, S. F. Khan, S. A. MacLaren, J. D. Salmonson, T. Ma, L. Masse, R. Tipton, P. A. Bradley, J. R. Rygg, J. E. Field, R. Tommasini, J. E. Ralph, D. P. Turnbull, A. J. Mackinnon, L. R. Benedetti, D. K. Bradley, S. Nagel, P. M. Celliers, E. Dewald, T. R. Dittrich, L. Berzak Hopkins, N. Izumi, M. L. Kervin, J. Kline, C. Yeamans, R. Hatarik, D. Sayre, E. P. Hartouni, A. Pak, K. C. Chen, and D. E. Hoover, "Using a 2-Shock 1D Platform at NIF to Measure the Effect of Convergence on Mix and Symmetry," Phys. Plasmas **25**, 102702 (2018).

T.-G. Lee, M. Busquet, M. Klapisch, J. W. Bates, A. J. Schmitt, S. X. Hu, and J. Giuliani, "Radiative and Atomic Properties of C and CH Plasmas in the Warm-Dense-Matter Regime," Phys. Rev. E **98**, 043203 (2018).

J. D. Lindl, S. W. Haan, O. L. Landen, A. R. Christopherson, and R. Betti, "Progress Toward a Self-Consistent Set of 1D Ignition Capsule Metrics in ICF," Phys. Plasmas **25**, 122704 (2018).

O. M. Mannion, V. Yu. Glebov, C. J. Forrest, J. P. Knauer, V. N. Goncharov, S. P. Regan, T. C. Sangster, C. Stoeckl, and M. Gatu Johnson, "Calibration of a Neutron Time-of-Flight Detector with a Rapid Instrument Response Function for Measurements of Bulk Fluid Motion on OMEGA," Rev. Sci. Instrum. **89**, 10I131 (2018).

A. Pak, S. Kerr, N. Lemos, A. Link, P. Patel, F. Albert, L. Divol, B. B. Pollock, D. Haberberger, D. Froula, M. Gauthier, S. H. Glenzer, A. Longman, L. Manzoor, R. Fedosejevs, S. Tochitsky, C. Joshi, and F. Fiuza, "Collisionless Shock Acceleration of Narrow Energy Spread Ion Beams from Mixed Species Plasmas Using 1 μm Lasers," Phys. Rev. Accel. Beams **21**, 103401 (2018).

J. P. Palastro, J. G. Shaw, R. K. Follett, A. Colaïtis, D. Turnbull, A. V. Maximov, V. N. Goncharov, and D. H. Froula, "Resonance Absorption of a Broadband Laser Pulse," Phys. Plasmas **25**, 123104 (2018).

J. Peebles, A. V. Arefiev, S. Zhang, C. McGuffey, M. Spinks, J. Gordon, E. W. Gaul, G. Dyer, M. Martinez, M. E. Donovan, T. Ditmire, J. Park, H. Chen, H. S. McLean, M. S. Wei, S. I. Krasheninnikov, and F. N. Beg, "High-Angle Deflection of the Energetic Electrons by a Voluminous Magnetic Structure in Near-Normal Intense Laser-Plasma Interactions," Phys. Rev. E **98**, 053202 (2018).

N. R. Pereira, A. T. Macrander, C. Stoeckl, and E. O. Baronova, "On Evaluating X-Ray Imaging Crystals with Synchrotron Radiation," Rev. Sci. Instrum. **89**, 10G126 (2018).

K. Prestridge, "Experimental Adventures in Variable-Density Mixing," Phys. Rev. Fluids **3**, 110501 (2018).

S. P. Regan, V. N. Goncharov, T. C. Sangster, E. M. Campbell, R. Betti, J. W. Bates, K. Bauer, T. Bernat, S. Bhandarkar, T. R. Boehly, M. J. Bonino, A. Bose, D. Cao, L. Carlson, R. Chapman, T. Chapman, G. W. Collins, T. J. B. Collins, R. S. Craxton, J. A. Delettrez, D. H. Edgell, R. Epstein, M. Farrell, C. J. Forrest, R. K. Follett, J. A. Frenje, D. H. Froula, M. Gatu Johnson, C. R. Gibson, L. Gonzalez, C. Goyon, V. Yu. Glebov, V. Gopalaswamy, A. Greenwood, D. R. Harding, M. Hohenberger, S. X. Hu, H. Huang, J. Hund, I. V. Igumenshchev, D. W. Jacobs-Perkins, R. T. Janezic, M. Karasik,

J. H. Kelly, T. J. Kessler, J. P. Knauer, T. Z. Kosc, R. Luo, S. J. Loucks, J. A. Marozas, F. J. Marshall, M. Mauldin, R. L. McCrory, P. W. McKenty, D. T. Michel, P. Michel, J. D. Moody, J. F. Myatt, A. Nikroo, P. M. Nilson, S. P. Obenschain, J. P. Palastro, J. Peebles, R. D. Petrasso, N. Petta, P. B. Radha, J. E. Ralph, M. J. Rosenberg, S. Sampat, A. J. Schmitt, M. J. Schmitt, M. Schoff, W. Seka, R. Shah, J. R. Rygg, J. G. Shaw, R. Short, W. T. Shmayda, M. J. Shoup III, A. Shvydky, A. A. Solodov, C. Sorce, M. Stadermann, C. Stoeckl, W. Sweet, C. Taylor, R. Taylor, W. Theobald, D. P. Turnbull, J. Ulreich, M. D. Wittman, K. M. Woo, K. Youngblood, and J. D. Zuegel, "The National Direct-Drive Inertial Confinement Fusion Program," Nucl. Fusion **59**, 032007 (2019).

S. Sampat, T. Z. Kosc, K. A. Bauer, R. D. Dean, W. R. Donaldson, J. Kwiatkowski, R. Moshier, A. L. Rigatti, M. H. Romanofsky, L. J. Waxer, and J. H. Kelly, "Power Balancing the Multibeam OMEGA Laser," Appl. Opt. **57**, 9571 (2018).

A. M. Saunders, B. Lahmann, G. Sutcliffe, J. A. Frenje, R. W. Falcone, and T. Döppner, "Characterizing Plasma Conditions in Radiatively Heated Solid-Density Samples with X-Ray Thomson Scattering," Phys. Rev. E **98**, 063206 (2018).

E. M. Schiesser, S.-W. Bahk, J. Bromage, and J. P. Rolland "Gaussian Curvature and Stigmatic Imaging Relations for the Design of an Unobscured Reflective Relay," Opt. Lett. **43**, 4855 (2018).

A. Shimony, W. C. Wan, S. R. Klein, C. C. Kuranz, R. P. Drake, D. Shvarts, and G. Malamud, "Construction and Validation of a Statistical Model for the Nonlinear Kelvin–Helmholtz Instability Under Compressible, Multimode Conditions," Phys. Plasmas **25**, 122112 (2018).

P. T. Springer, O. A. Hurricane, J. H. Hammer, R. Betti, D. A. Callahan, E. M. Campbell, D. T. Casey, C. J. Cerjan, D. Cao, E. Dewald, L. Divol, T. Doeppner, M. J. Edwards, J. E. Field, C. Forrest, J. Frenje, J. A. Gaffney, M. Gatu-Johnson, V. Glebov, V. N. Goncharov, G. P. Grim, E. Hartouni, R. Hatarik, D. E. Hinkel, L. Berzak Hopkins, I. Igumenshchev, P. Knapp, J. P. Knauer, A. L. Kritcher, O. Landen, A. Pak, S. Le Pape, T. Ma, A. G. MacPhee, D. H. Munro, R. C. Nora, P. K. Patel, L. Peterson, P. B. Radha, S. P. Regan, H. Rinderknecht, C. Sangster, B. K. Spears, and C. Stoeckl, "A 3D Dynamic Model to Assess the Impacts of Low-Mode Asymmetry, Aneurysms and Mix-Induced Radiative Loss on Capsule Performance Across Inertial Confinement Fusion Platforms," Nucl. Fusion **59**, 032009 (2019).

C. Stoeckl, T. Filkins, R. Jungquist, C. Mileham, N. R. Pereira, S. P. Regan, M. J. Shoup III, and W. Theobald, "Characterization of Shaped Bragg Crystal Assemblies for Narrowband X-Ray Imaging," Rev. Sci. Instrum. **89**, 10G124 (2018).

J. D. Styron, C. L. Ruiz, K. D. Hahn, G. W. Cooper, G. A. Chandler, B. Jones, B. R. McWatters, C. J. Forrest, J. Vaughan, J. Torres, S. Pelka, J. Smith, and C. Weaver, "Average Neutron Time-of-Flight Instrument Response Function Inferred from Single D-T Neutron Events Within a Plastic Scintillator," Rev. Sci. Instrum. **89**, 10I119 (2018).

W. Theobald, C. Sorce, M. Bedzyk, S. T. Ivancic, F. J. Marshall, C. Stoeckl, R. C. Shah, M. Lawrie, S. P. Regan, T. C. Sangster, E. M. Campbell, T. J. Hilsabeck, K. Engelhorn, J. D. Kilkenny, D. Morris, T. M. Chung, J. D. Hares, A. K. L. Dymoke-Bradshaw, P. Bell, J. Celeste, A. C. Carpenter, M. Dayton, D. K. Bradley, M. C. Jackson, L. Pickworth, S. R. Nagel, G. Rochau, J. Porter, M. Sanchez, L. Claus, G. Robertson, and Q. Looker, "The Single-Line-of-Sight, Time-Resolved X-Ray Imager Diagnostic on OMEGA," Rev. Sci. Instrum. **89**, 10G117 (2018).

D. B. Thorn, F. Coppari, T. Döppner, M. J. MacDonald, S. P. Regan, and M. B. Schneider, "X-Ray Spectrometer Throughput Model for (Selected) Flat Bragg Crystal Spectrometers on Laser Plasma Facilities," Rev. Sci. Instrum. **89**, 10F119 (2018).

D. Turnbull, S.-W. Bahk, I. A. Begishev, R. Boni, J. Bromage, S. Bucht, A. Davies, P. Franke, D. Haberberger, J. Katz, T. J. Kessler, A. L. Milder, J. P. Palastro, J. L. Shaw, and D. H. Froula, "Flying Focus and Its Application to Plasma-Based Laser Amplifiers," Plasma Phys. Control. Fusion **61**, 014022 (2019).

M. P. Valdivia, F. Veloso, D. Stutman, C. Stoeckl, C. Mileham, I. A. Begishev, W. Theobald, M. Vescovi, W. Useche, S. P. Regan, B. Albertazzi, G. Rigon, P. Mabey, T. Michel, S. A. Pikuz, M. Koenig, and A. Casner, "X-Ray Backlighter Requirements for Refraction-Based Electron Density Diagnostics Through Talbot-Lau Deflectometry," Rev. Sci. Instrum. **89**, 10G127 (2018).

A. J. White, O. Certik, Y. H. Ding, S. X. Hu, and L. A. Collins, "Time-Dependent Orbital-Free Density Functional Theory for Electronic Stopping Power: Comparison to the Mermin-Kohn-Sham Theory at High Temperatures," Phys. Rev. B **98**, 144302 (2018).

K. M. Woo, R. Betti, D. Shvarts, O. M. Mannion, D. Patel, V. N. Goncharov, K. S. Anderson, P. B. Radha, J. P. Knauer, A. Bose, V. Gopalaswamy, A. R. Christopherson, E. M. Campbell, J. Sanz, and H. Aluie, "Impact of Three-Dimensional Hot-Spot Flow Asymmetry on Ion-Temperature Measurements in Inertial Confinement Fusion Experiments," Phys. Plasmas **25**, 102710 (2018).

M. Zaghoo, R. J. Husband and I. F. Silvera, "Striking Isotope Effect on the Metallization Phase Lines of Liquid Hydrogen and Deuterium," Phys. Rev. B **98**, 104102 (2018).

H. Zhang, R. Betti, R. Yan, D. Zhao, D. Shvarts, and H. Aluie, "Self-Similar Multimode Bubble-Front Evolution of the Ablative Rayleigh-Taylor Instability in Two and Three Dimensions," Phys. Rev. Lett. **121**, 185002 (2018).

X. Zhang and M. Z. Yates, "Controllable Synthesis of Hydroxyapatite-Supported Palladium Nanoparticles with Enhanced Catalytic Activity," Surf. Coat. Technol. **351**, 60 (2018).

Forthcoming Publications

H. Aluie, "Convolutions on the Sphere: Commutation with Differential Operators," to be published in GEM: International Journal on Geomathematics.

K. A. Bauer, M. Heimbueger, S. Sampat, L. J. Waxer, E. C. Cost, J. H. Kelly, V. Kobilansky, J. Kwiatkowski, S. F. B. Morse, D. Nelson, D. Weiner, G. Weselak, and J. Zou, "Comparison of On-Shot, In-Tank and Equivalent-Target-Plane Measurements of the OMEGA Laser System Focal Spot," to be published in Proceedings of SPIE.

R. L. Berger, C. A. Thomas, K. L. Baker, D. T. Casey, C. S. Goyon, J. Park, N. Lemos, S. F. Khan, M. Hohenberger, J. L. Milovich, D. J. Strozzi, M. A. Belyaev, T. Chapman, and A. B. Langdon, "Stimulated Backscatter of Laser Light from Big Foot Hohlraums on the National Ignition Facility," to be published in Physics of Plasmas.

W. A. Bittle, M. Bock, R. Boni, J. Kendrick, A. Sorce, and C. Sorce, "A Rate-Doubled 10-GHz Fiducial Comb Generator

for Precision Optical Timing Calibration," to be published in Review of Scientific Instruments.

J. Bromage, S.-W. Bahk, I. A. Begishev, C. Dorrer, M. J. Guardalben, B. N. Hoffman, J. B. Oliver, R. G. Roides, E. M. Schiesser, M. J. Shoup III, M. Spilatro, B. Webb, D. Weiner, and J. D. Zuegel, "Technology Development for Ultraintense All-OPCPA Systems," to be published in High Power Laser Science and Engineering.

A. R. Christopherson, R. Betti, and J. D. Lindl, "Thermonuclear Ignition and the Onset of Propagating Burn in Inertial Fusion Implosions," to be published in Physical Review E.

A. S. Davies, D. Haberberger, J. Katz, S. Bucht, J. P. Palastro, W. Rozmus, and D. H. Froula, "Picosecond Thermodynamics in Underdense Plasmas Measured with Thomson Scattering," to be published in Physical Review Letters.

J. R. Davies, D. H. Barnak, R. Betti, E. M. Campbell, V. Yu. Glebov, E. C. Hansen, J. P. Knauer, J. L. Peebles, and A. B. Sekfow, "Inferring Fuel Areal Density from Secondary Neutron Yields in Laser-Driven Magnetized Liner Inertial Fusion," to be published in Physics of Plasmas.

S. G. Demos, B. N. Hoffman, C. W. Carr, D. A. Cross, R. A. Negres, and J. D. Bude, "Mechanisms of Laser-Induced Damage in Absorbing Glasses with Nanosecond Pulses," to be published in Optics Express.

W. R. Donaldson and A. Consentino, "Co-Timing UV and IR Laser Pulses on the OMEGA EP Laser System," to be published in Proceedings of SPIE.

C. Dorrer, "Spatiotemporal Metrology of Broadband Optical Pulses," to be published in IEEE Journal on Selected Topics in Quantum Electronics.

D. E. Fratanduono, M. Millot, A. Fernandez Pañella, P. A. Sterne, G. W. Collins, D. G. Hicks, J. H. Eggert, T. R. Boehly, and P. M. Celliers, "Measurement of the Sound Speed in Dense Fluid Deuterium Along the Cryogenic Liquid Hugoniot," to be published in Physics of Plasmas.

J. A. Frenje, R. Florido, R. Mancini, T. Nagayama, P. E. Grabowski, H. Rinderknecht, H. Sio, A. Zylstra, M. Gatu Johnson, C. K. Li, F. H. Séguin, R. D. Petrasso, V. Yu. Glebov,

and S. P. Regan, "Experimental Validation of Low-Z Ion-Stopping Formalisms Around the Bragg Peak in High-Energy-Density Plasmas," to be published in Physical Review Letters.

D. H. Froula, J. P. Palastro, D. Turnbull, A. Davies, L. Nguyen, A. Howard, D. Ramsey, P. Franke, S.-W. Bahk, I. A. Begishev, R. Boni, J. Bromage, S. Bucht, R. K. Follett, D. Haberberger, G. W. Jenkins, J. Katz, T. J. Kessler, J. L. Shaw, and J. Vieira, "Flying Focus: Spatial and Temporal Control of Intensity for Laser-Based Applications," to be published in Physics of Plasmas (invited).

L. Gao, E. Liang, Y. Lu, R. K. Follett, H. Sio, P. Tzeferacos, D. H. Froula, A. Birkel, C. K. Li, D. Lamb, R. Petrasso, W. Fu, M. Wei, and H. Ji, "Mega-Gauss Plasma Jet Creation Using a Ring of Laser Beams," to be published in Astrophysical Journal Letters.

M. Gatu Johnson, B. D. Appelbe, J. P. Chittenden, A. Crilly, J. Delettrez, C. Forrest, J. A. Frenje, V. Yu. Glebov, W. Grimble, B. M. Haines, I. V. Igumenshchev, R. Janezic, J. P. Knauer, B. Lahmann, F. J. Marshall, T. Michel, F. H. Séguin, C. Stoeckl, C. Walsh, A. B. Zylstra, and R. D. Petrasso, "Impact of Imposed Mode 2 Laser Drive Asymmetry on Inertial Confinement Fusion Implosions," to be published in Physics of Plasmas.

V. Gopalaswamy, R. Betti, J. P. Knauer, N. Luciani, D. Patel, K. M. Woo, A. Bose, I. V. Igumenshchev, E. M. Campbell, K. S. Anderson, K. A. Bauer, M. J. Bonino, D. Cao, A. R. Christopherson, G. W. Collins, T. J. B. Collins, J. R. Davies, J. A. Delettrez, D. H. Edgell, R. Epstein, C. J. Forrest, D. H. Froula, V. Y. Glebov, V. N. Goncharov, D. R. Harding, S. X. Hu, D. W. Jacobs-Perkins, R. T. Janezic, J. H. Kelly, O. M. Mannion, A. Maximov, F. J. Marshall, D. T. Michel, S. Miller, S. F. B. Morse, J. Palastro, J. Peebles, P. B. Radha, S. P. Regan, S. Sampat, T. C. Sangster, A. B. Sefkow, W. Seka, R. C. Shah, W. T. Shmayda, A. Shvydky, C. Stoeckl, A. A. Solodov, W. Theobald, J. D. Zuegel, M. Gatu Johnson, R. D. Petrasso, C. K. Li, and J. A. Frenje, "Tripled Yield in Direct-Drive Laser Fusion Through Statistical Modeling," to be published in Nature.

R. J. Henchen, M. Sherlock, W. Rozmus, J. Katz, P. E. Masson-Laborde, D. Cao, J. P. Palastro, and D. H. Froula, "Measuring Heat Flux from Collective Thomson Scattering with Non-Maxwellian Distribution Functions," to be published in Physics of Plasmas (invited).

D. P. Higginson, J. S. Ross, D. D. Ryutov, F. Fiuza, S. C. Wilks, E. P. Hartouni, R. Hatarik, C. M. Huntington, J. Kilkenny, B. Lahmann, C. K. Li, A. Link, R. D. Petrasso, B. B. Pollock, B. A. Remington, H. G. Rinderknecht, Y. Sakawa, H. Sio, G. F. Swadling, S. Weber, A. B. Zylstra, and H.-S. Park, "Kinetic Effects on Neutron Generation in Moderately Collisional Interpenetrating Plasma Flows," to be published in Physics of Plasmas.

K. R. P. Kafka and S. G. Demos, "Interaction of Short Laser Pulses with Model Contamination Microparticles on a High Reflector," to be published in Optics Letters.

A. Kar, T. R. Boehly, P. B. Radha, D. H. Edgell, S. X. Hu, P. M. Nilson, A. Shvydky, W. Theobald, D. Cao, K. S. Anderson, V. N. Goncharov, and S. P. Regan, "Simulated Refraction-Enhanced X-Ray Radiography of Laser-Driven Shocks," to be published in Physics of Plasmas.

P. F. Knapp, M. R. Gomez, S. B. Hansen, M. E. Glinsky, C. A. Jennings, S. A. Slutz, E. C. Harding, K. D. Hahn, M. R. Weis, M. Evans, M. R. Martin, A. J. Harvey-Thompson, M. Geissel, I. C. Smith, D. E. Ruiz, K. J. Peterson, B. M. Jones, J. Schwarz, G. A. Rochau, D. B. Sinars, R. D. McBride, and P.-A. Gourdain, "Origins and Effects of Mix on Magnetized Liner Inertial Fusion Target Performance," to be published in Physics of Plasmas.

K. Kopp and S. G. Demos, "Microscopy with Ultraviolet Surface Excitation (MUSE) Enables Translation of Optical Biopsy Principles to Enhance Life Science Education," to be published in Proceedings of SPIE.

A. Koroliov, G. Chen, K. M. Goodfellow, A. N. Vamivakas, Z. Staniszewski, P. Sobolewski, M. El Fray, A. Łaszcz, A. Czerwinski, C. P. Richter, and R. Sobolewski, "Terahertz Time-Domain Spectroscopy of Graphene Nanoflakes Embedded in Polymer Matrix," to be published in Applied Sciences.

A. A. Kozlov, J. C. Lambropoulos, J. B. Oliver, B. N. Hoffman, and S. G. Demos, "Mechanisms of Picosecond Laser-Induced Damage in Common Multilayer Dielectric Coatings," to be published in Scientific Reports.

B. E. Kruschwitz, J. Kwiatkowski, C. Dorrer, M Barczys, A. Consentino, D. H. Froula, M. J. Guardalben, E. M. Hill, D. Nelson, M. J. Shoup III, D. Turnbull, L. J. Waxer, and D. Weiner, "Tunable UV Upgrade on OMEGA EP," to be published in Proceedings of SPIE.

S. LePape, L. Divol, A. MacPhee, J. McNaney, M. Hohenberger, D. Froula, V. Glebov, O. L. Landen, C. Stoeckl, E. Dewald, S. Khan, C. Yeamans, P. Michel, M. Schneider, J. Knauer, J. Kilkenny, and A. J. Mackinnon, "Optimization of High-Energy X Ray Production Through Laser–Plasma Interaction," to be published in High Energy Density Physics.

Y. Lu, P. Tzeferacos, E. Liang, R. K. Follett, L. Gao, A. Birkel, D. H. Froula, W. Fu, H. Ji, D. Lamb, C. K. Li, H. Sio, R. Petrasso, and M. S. Wei, "Numerical Simulation of Magnetized Jet Creation Using a Hollow Ring of Laser Beams," to be published in Physics of Plasmas.

A. Macrander, N. Pereira, C. Stoeckl, X. Huang, and E. Kasman, "Quartz Conditioning Crystal for X-Ray Rocking Curve Topography," to be published in the Journal of Applied Crystallography.

A. L. Milder, S. T. Ivancic, J. P. Palastro, and D. H. Froula, "Impact of Non-Maxwellian Electron Velocity Distribution Functions on Inferred Plasma Parameters in Collective Thomson Scattering," to be published in Physics of Plasmas.

R. Paul, S. X. Hu, and V. V. Karasiev, "Anharmonic and Anomalous Trends in the High-Pressure Phase Diagram of Silicon," to be published in Physical Review Letters.

M. J. Rosenberg, R. Epstein, A. A. Solodov, W. Seka, J. F. Myatt, P. A. Michel, M. A. Barrios, D. B. Thorn, M. Hohenberger, J. D. Moody, and S. P. Regan, "X-Ray Spectroscopy of Planar Laser–Plasma Interaction Experiments at the National Ignition Facility," to be published in Physics of Plasmas.

M. J. Rosenberg, D. B. Thorn, N. Izumi, D. Williams, M. Rowland, G. Torres, M. Haugh, P. Hillyard, N. Adelman, T. Schuler, M. A. Barrios, J. P. Holder, M. B. Schneider, K. B. Fournier, D. K. Bradley, and S. P. Regan, "Image-Plate Sensitivity to X Rays at 2 to 60 keV," to be published in Review of Scientific Instruments.

J. Serafini, A. Hossain, R. B. James, S. B. Trivedi, and R. Sobolewski, "Time-Resolved, Nonequilbrium Carrier and Coherent Acoustic Phonon Dynamics in (Cd,Mg)Te Single Crystals for Radiation Detectors," to be published in Semiconductor Science and Technology.

H. Sio, J. A. Frenje, A. Le, S. Atzeni, T. J. T. Kwan, M. Gatu Johnson, G. Kagan, C. Stoeckl, C. K. Li, C. E. Parker, C. J. Forrest, V. Glebov, N. V. Kabadi, A. Bose, H. G. Rinderknecht,

P. Amendt, D. T. Casey, R. Mancini, W. T. Taitano, B. Keenan, A. N. Simakov, L. Chacón, S. P. Regan, T. C. Sangster, E. M. Campbell, F. H. Seguin, and R. D. Petrasso, "Observations of Multiple Nuclear Reaction Histories and Fuel-Ion Species Dynamics in Shock-Driven Inertial Confinement Fusion Implosions," to be published in Physical Review Letters.

R. Sobolewski, "Optical Sensors," to be published in the Handbook of Superconducting Materials.

R. B. Spielman and D. B. Reisman, "On the Design of Magnetically Insulated Transmission Lines for Z-Pinch Loads," to be published in Matter and Radiation at Extremes.

D. Turnbull, S.-W. Bahk, I. A. Begishev, R. Boni, J. Bromage, S. Bucht, A. Davies, P. Franke, D. Haberberger, J. Katz, T. J. Kessler, A. L. Milder, J. P. Palastro, J. L. Shaw, and D. H. Froula, "Flying Focus and Its Application to Plasma-Based Laser Amplifiers," to be published in Plasma Physics and Controlled Fusion.

L. J. Waxer, K. A. Bauer, E. C. Cost, M. Heimbueger, J. H. Kelly, V. Kobilansky, S. F. B. Morse, D. Nelson, R. Peck, R. Rinefierd, S. Sampat, M. J. Shoup III, D. Weiner, G. Weselak, and J. Zou, "In-Tank, On-Shot Characterization of the OMEGA Laser System Focal Spot," to be published in Proceedings of SPIE.

B. Webb, M. J. Guardalben, C. Dorrer, S. Bucht, and J. Bromage, "Simulation of Grating Compressor Misalignment Tolerances and Mitigation Strategies for Chirped-Pulse–Amplification Systems of Varying Bandwidths and Beam Sizes," to be published in Applied Optics.

R. P. Young, C. C. Kuranz, D. Froula, J. S. Ross, and S. Klein, "Observation of Collisionless-to-Collisional Transition in Colliding Plasma Jets with Optical Thomson Scattering," to be published in Physics of Plasmas.

M. Zaghoo, T. R. Boehly, J. R. Rygg, P. M. Celliers, S. X. Hu, and G. W. Collins, "Breakdown of Fermi Degeneracy in the Simplest Liquid Metal," to be published in Physical Review Letters.

Conference Presentations

The following presentations were made at the CEA–NNSA Joint Diagnostic Meeting, Le Barp, France, 2–3 October 2018:

S. P. Regan, C. J. Forrest, W. Theobald, C. Sorce, C. Danly, I. V. Igumenshchev, V. N. Goncharov, F. J. Marshall, V. Yu. Glebov, T. C. Sangster, E. M. Campbell, P. Volegov, T. Murphy, C. Wilde, J. Kline, O. Landoas, T. Caillaud, B. Rosse, M. Briat, I. Thfoin, J. L. Bourgade, T. Dautremer, E. Barat, and J. D. Kilkenny, "OMEGA Neutron Imaging Project."

W. Theobald, "3-D Hot-Spot X-Ray Imaging for OMEGA DT Cryogenic Implosions."

The following presentations were made at the CELIA Seminar, Bordeaux, France, 3 October 2018:

S. X. Hu, W. Theobald, J. L. Peebles, S. P. Regan, P. B. Radha, D. T. Michel, Y. H. Ding, V. N. Goncharov, T. R. Boehly, R. Epstein, E. M. Campbell, G. Duchateau, A. Casner, V. Tikhonchuk, L. A. Collins, J. D. Kress, and B. Militzer, "Understanding ICF Implosions on OMEGA: From Intrinsic Material Properties to Laser Imprint."

M. S. Wei, C. M. Krauland, S. Muller, S. Zhang, J. Li, J. L. Peebles, F. N. Beg, W. Theobald, E. Borwick, C. Ren, C. Stoeckl, D. Haberberger, T. Filkins, D. Turnbull, R. Betti, E. M. Campbell, J. Trela, D. Batani, K. Glize, R. Scott, and L. Antonelli, "Laser–Plasma Instabilities and Hot-Electron Generation in the Shock-Ignition Intensity Regime."

The following presentations were made at the First LMJ–PETAL User Meeting, Bordeaux, France, 4–5 October 2018:

E. M. Campbell, "A Perspective on the Future of ICF and HEDP Research."

W. Theobald, R. Betti, A. Bose, S. X. Hu, E. M. Campbell, S. P. Regan, C. McCoy, A. Casner, L. Ceurvorst, and M. Karasik, "The Hybrid Target Approach: A Promising Path Forward to Mitigate Laser Imprint in Direct-Drive Inertial Confinement Fusion."

M. S. Wei and J. M. Soures, "Overview of the Omega Laser Facility and Basic Science User Program."

E. M. Campbell, "Fusion: Making a Star on Earth and the Quest for the Ultimate Energy Source to Power the Planet," presented at the AEFM Seminar, Rochester, NY, 11 October 2018.

———————

Y. Zhao, "AlGaN Metal–Semiconductor–Metal UV Photodetectors," presented at Industrial Associates, Rochester, NY, 19 October 2018.

———————

The following presentations were made at the 4th International Conference on High Energy Density Physics, Ningbo, China, 21–25 October 2018:

R. Betti, V. Gopalaswamy, J. P. Knauer, A. R. Christopherson, D. Patel, K. M. Woo, A. Bose, K. S. Anderson, T. J. B. Collins, S. X. Hu, V. Yu. Glebov, A. V. Maximov, C. Stoeckl, F. J. Marshall, M. J. Bonino, D. R. Harding, R. T. Janezic, J. H. Kelly, S. Sampat, T. C. Sangster, S. P. Regan, E. M. Campbell, M. Gatu Johnson, J. A. Frenje, C. K. Li, R. D. Petrasso, and O. A. Hurricane, "Progress Toward Ignition and Burn in Inertial Confinement Fusion."

D. H. Froula, J. P. Palastro, D. Turnbull, T. J. Kessler, A. Davies, A. Howard, L. Nguyen, D. Ramsey, G. W. Jenkins, S.-W. Bahk, I. A. Begishev, R. Boni, J. Bromage, S. Bucht, R. K. Follett, D. Haberberger, J. Katz, and J. L. Shaw, "Flying Focus: Spatiotemporal Control of Intensity for Laser-Based Applications."

J. P. Knauer, R. Betti, V. Gopalaswamy, M. J. Bonino, E. M. Campbell, T. J. B. Collins, C. J. Forrest, V. Yu. Glebov, V. N. Goncharov, D. R. Harding, O. M. Mannion, J. A. Marozas, F. J. Marshall, P. W. McKenty, D. T. Michel, P. B. Radha, S. P. Regan, T. C. Sangster, C. Stoeckl, M. Gatu Johnson, and J. A. Frenje, "Direct-Drive, High-Adiabat, Cryogenic Implosion Results from the OMEGA Laser System" (invited).

K. Luo, D. Mejia-Rodriguez, V. V. Karasiev, J. Dufty, and S. B. Trickey, "Development of Free Energy Density Functional Theory: Predictive Power of First Principles Approximations for Warm Dense Matter."

———————

The following presentations were made at Tritium Focus Group-Sandia, Albuquerque, NM, 22–25 October 2018:

D. Bassler, C. Fagan, W. T. Shmayda, and W. U. Schröder, "Tritium Interactions with Thin Films of Al_2O_3 on Stainless-Steel 316."

C. Fagan, M. Sharpe, W. T. Shmayda, and W. U. Schroder, "Low-Pressure, Radio-Frequency–Generated Plasma for Tritium Desorption from Metals."

M. Sharpe, C. Fagan, and W. T. Shmayda, "Influence of Microstructure on the Absorption of Tritium into Gold-Plated 316 Stainless Steel."

W. T. Shmayda, N. P. Redden, and R. Earley, "Enhancing Gas Chromatography Performance."

———————

P. B. Radha, "Overview and Status of Direct-Drive Inertial Confinement Fusion in the United States," presented at the 27th IAEA Fusion Energy Conference (FEC 2018), Ahmedabad, India, 22–27 October 2018.

———————

The following presentations were made at the NIF VISAR Workshop, Livermore, CA, 23–24 October 2018:

M. K. Ginnane, A. Sorce, J. D. Kendrick, R. Boni, B. Saltzman, D. Weiner, M. Zaghoo, D. N. Polsin, B. J. Henderson, J. Zou, M. Couch, C. M. Rogoff, M. C. Gregor, T. R. Boehly, J. R. Rygg, and G. W. Collins, "Improvements to the VISAR and Streaked Optical Pyrometer at the Omega Laser Facility."

J. L. Peebles, S. X. Hu, V. N. Goncharov, N. Whiting, P. M. Celliers, S. J. Ali, G. Duchateau, E. M. Campbell, T. R. Boehly, and S. P. Regan, "First Direct-Drive Measurements of Laser-Imprint-Induced Shock-Velocity Nonuniformities on OMEGA."

———————

The following presentations were made at the U.S.-Japan Workshop on Theory and Simulations of High-Field and High-Energy-Density Physics, Portland OR, 3–4 November 2018:

A. Howard, D. Turnbull, A. Davies, D. H. Froula, and J. P. Palastro, "Photon Acceleration in the Ionization Front of a Flying Focus."

P. M. Nilson, F. Ehrne, C. Mileham, D. Mastrosimone, C. Taylor, R. K. Jungquist, R. Boni, J. Hassett, C. R. Stillman,

S. T. Ivancic, D. J. Lonobile, R. W. Kidder, M. J. Shoup III, A. B. Sefkow, A. A. Solodov, W. Theobald, C. Stoeckl, S. X. Hu, D. H. Froula, K. W. Hill, L. Gao, M. Bitter, P. Efthimion, I. Golovkin, and D. D. Meyerhofer, "High-Resolving-Power, Streaked X-Ray Spectroscopy of Picosecond-Scale Relativistic Laser–Matter Interactions on the OMEGA EP Laser System."

J. L. Peebles, J. R. Davies, D. H. Barnak, A. B. Sefkow, P. A. Gourdain, R. Betti, and A. Arefiev, "Characterizing Magnetic and Electric Fields from Laser-Driven Coils Using Axial Proton Probing."

H. Rinderknecht, H.-S. Park, J. S. Ross, P. A. Amendt, D. P. Higginson, S. C. Wilks, R. K. Follett, D. Haberberger, J. Katz, D. H. Froula, N. M. Hoffman, G. Kagan, B. Keenan, A. Simakov, L. Chacon, and E. Vold, "Ion-Velocity Structure in Strong Collisional Plasma Shocks."

———————————

The following presentations were made at the 60th Annual APS Division of Plasma Physics, Portland OR, 5–9 November 2018:

K. S. Anderson, C. J. Forrest, O. M. Mannion, D. T. Michel, R. C. Shah, J. A. Marozas, P. B. Radha, F. J. Marshall, J. P. Knauer, R. Epstein, V. Gopalaswamy, M. Gatu Johnson, and S. Laffite, "Modeling of Target Offset in Warm Implosions on OMEGA."

D. Cao, R. C. Shah, S. P. Regan, C. Sorce, R. Epstein, I. V. Igumenshchev, V. Gopalaswamy, A. R. Christopherson, W. Theobald, P. B. Radha, and V. N. Goncharov, "Using the 10 to 20 keV X-Ray Spectrum to Infer an Electron Temperature (T_e) as an Implosion Diagnostic on OMEGA."

D. A. Chin, P. M. Nilson, G. W. Collins, T. R. Boehly, J. R. Rygg, F. Coppari, Y. Ping, D. Trail, I. Szumila, and M. Harmand "Interpreting EXAFS Spectra: Toward Ramp-Compression Studies of Iron Oxide (FeO)."

A. R. Christopherson, R. Betti, S. Miller, V. Gopalaswamy, D. Cao, D. Keller, and J. D. Lindl, "Thermonuclear Ignition and the Onset of Propagating Burn in Inertial Fusion."

G. W. Collins, J. R. Rygg, T. R. Boehly, M. Zaghoo, D. N. Polsin, B. J. Henderson, X. Gong, L. Crandall, R. Saha, J. J. Ruby, G. Tabak, M. Huff, Z. Sprowal, A. Chin, M. K. Ginnane, P. M. Celliers, J. H. Eggert, A. Lazicki, R. F. Smith, R. Hemley,

F. Coppari, B. Bachman, J. Gaffney, D. E. Fratanduono, D. G. Hicks, Y. Ping, D. Swift, D. G. Braun, S. Hamel, M. Milllot, M. Gorman, R. Briggs, S. Ali, R. Kraus, M. McMahon, S. Brygoo, R. Jeanloz, R. Falcone, F. N. Beg, C. Bolme, A. Gleason, S. H. Glenzer, H. J. Lee, T. Duffy, J. Wang, J. Wark, and G. Gregori, "Matter at Extreme Energy Density: Exotic Solids to Inertial Fusion" (invited).

T. J. B. Collins, C. Stoeckl, R. Epstein, R. Betti, J. A. Delettrez, W. Bittle, C. J. Forrest, V. Yu. Glebov, V. N. Goncharov, D. R. Harding, I. V. Igumenshchev, D. W. Jacobs-Perkins, R. T. Janezic, J. H. Kelly, T. Z. Kosc, C. Mileham, D. T. Michel, R. L. McCrory, P. W. McKenty, F. J. Marshall, S. F. B. Morse, P. B. Radha, S. P. Regan, B. Rice, T. C. Sangster, M. J. Shoup III, W. T. Shmayda, C. Sorce, W. Theobald, J. Ulreich, M. D. Wittman, J. A. Frenje, M. Gatu Johnson, and R. D. Petrasso, "Cryogenic Target Performance and Fuel-Ablator Perturbation Growth."

L. Crandall, J. R. Rygg, G. W. Collins, T. R. Boehly, M. Zaghoo, P. M. Celliers, D. E. Fratanduono, M. C. Gregor, A. Jenei, M. Millot, J. H. Eggert, and D. Spaulding, "Equation-of-State Measurements of Precompressed CO_2."

R. S. Craxton, Y. Yang, E. M. Garcia, P. W. McKenty, M. J. Schmitt, and K. Molvig, "*Revolver* Designs for the National Ignition Facility Using Current and Optimized Phase Plates."

A. Davies, J. Katz, S. Bucht, D. Haberberger, J. P. Palastro, I. A. Begishev, J. L. Shaw, D. Turnbull, R. Boni, D. H. Froula, and W. Rozmus, "Ultrafast Thomson Scattering and the Effects of Collisions on the Electron Plasma Wave Feature."

J. R. Davies, D. H. Barnak, R. Betti, P.-Y. Chang, V. Yu. Glebov, E. C. Hansen, J. P. Knauer, J. L. Peebles, A. B. Sefkow, K. J. Peterson, and D. B. Sinars, "Laser-Driven Magnetized Liner Inertial Fusion on OMEGA" (invited).

Y. H. Ding, S. X. Hu, A. J. White, O. Certik, and L. A. Collins, "*Ab Initio* Studies on Stopping Power of Warm Dense Matter with Time-Dependent Orbital-Free Density Functional Theory."

D. H. Edgell, R. K. Follett, J. Katz, J. P. Palastro, D. Turnbull, and D. H. Froula, "Density Profile Measurements on OMEGA Using the CBET Beamlets Diagnostic."

R. Epstein, C. Stoeckl, P. B. Radha, T. J. B. Collins, P. W. McKenty, D. Cao, R. C. Shah, D. Cliche, and R. C. Mancini,

"Inferring Shell Nonuniformity in OMEGA Implosions by Self-Emission Radiography."

R. K. Follett, J. G. Shaw, D. H. Edgell, D. H. Froula, C. Dorrer, J. Bromage, E. M. Campbell, E. M. Hill, T. J. Kessler, J. P. Palastro, J. F. Myatt, J. W. Bates, and J. L. Weaver, "Suppressing Parametric Instabilities with Laser Frequency Detuning and Bandwidth" (invited).

C. J. Forrest, K. S. Anderson, V. Yu. Glebov, V. Gopalaswamy, V. N. Goncharov, J. P. Knauer, O. M. Mannion, P. B. Radha, S. P. Regan, T. C. Sangster, R. C. Shah, C. Stoeckl, J. A. Frenje, and M. Gatu Johnson, "Evaluating the Residual Kinetic Energy in Direct-Drive Cryogenic Implosions on OMEGA."

P. Franke, D. Turnbull, J. P. Palastro, J. Katz, I. A. Begishev, R. Boni, J. Bromage, A. L. Milder, J. L. Shaw, and D. H. Froula, "Ionization Waves of Arbitrary Velocity."

D. H. Froula, J. P. Palastro, D. Turnbull, T. J. Kessler, A. Davies, P. Franke, A. Howard, L. Nguyen, D. Ramsey, G. W. Jenkins, S.-W. Bahk, I. A. Begishev, R. Boni, J. Bromage, S. Bucht, R. K. Follett, D. Haberberger, J. Katz, J. L. Shaw, F. A. Hegmann, D. Purschke, N. Vafaei-Najafabadi, J. Vieira, and F. Quéré, "Flying Focus: Spatial and Temporal Control of Intensity for Laser Based Application" (invited).

M. K. Ginnane, A. Sorce, J. D. Kendrick, R. Boni, B. Saltzman, D. Weiner, M. Zaghoo, D. N. Polsin, B. J. Henderson, J. Zou, M. Couch, C. M. Rogoff, M. C. Gregor, T. R. Boehly, J. R. Rygg, and G. W. Collins, "Improvements to the VISAR and Streaked Optical Pyrometer at the Omega Laser Facility."

V. Yu. Glebov, C. J. Forrest, J. P. Knauer, O. M. Mannion, S. P. Regan, T. C. Sangster, C. Stoeckl, M. J. Eckart, G. P. Grim, A. S. Moore, and D. J. Schlossberg, "DT Yield and Ion Temperature Measurement with a Cherenkov Neutron Time-of-Flight Detector on OMEGA."

V. N. Goncharov, "Perturbation Evolution at Early Stages of Inertial Confinement Fusion Implosions."

X. Gong, D. N. Polsin, L. Crandall, M. Huff, B. J. Henderson, J. R. Rygg, T. R. Boehly, G. W. Collins, A. Jenei, M. G. Gorman, R. Briggs, J. H. Eggert, and M. I. McMahon, "X-Ray Diffraction of Ramp-Compressed Potassium."

V. Gopalaswamy, R. Betti, J. P. Knauer, K. M. Woo, D. Patel, A. R. Christopherson, A. Bose, N. Luciani, F. J. Marshall,

C. Stoeckl, V. Yu. Glebov, S. P. Regan, D. T. Michel, W. Seka, D. H. Edgell, R. C. Shah, D. Cao, V. N. Goncharov, J. A. Delettrez, I. V. Igumenshchev, P. B. Radha, T. J. B. Collins, T. C. Sangster, E. M. Campbell, M. Gatu Johnson, R. D. Petrasso, C. K. Li, and J. A. Frenje, "Optimization of Direct-Drive Inertial Fusion Implosions Through Predictive Statistical Modeling" (invited).

D. Haberberger, A. Shvydky, J. P. Knauer, S. X. Hu, V. N. Goncharov, S. T. Ivancic, and D. H. Froula, "Density Measurements of the Inner Shell Release."

A. M. Hansen, D. Turnbull, D. Haberberger, J. Katz, D. Mastrosimone, A. Colaïtis, A. B. Sefkow, R. K. Follett, J. P. Palastro, and D. H. Froula, "Cross-Beam Energy Transfer Platform Development on OMEGA."

R. J. Henchen, J. Katz, D. Cao, J. P. Palastro, D. H. Froula, M. Sherlock, and W. Rozmus, "Direct Measurements of Nonlocal Heat Flux by Thomson Scattering" (invited).

B. J. Henderson, T. R. Boehly, M. Zaghoo, J. R. Rygg, D. N. Polsin, X. Gong, L. Crandall, M. Huff, M. K. Ginnane, G. W. Collins, S. Ali, and P. M. Celliers, "Broadband Reflectivity Diagnostic Development for Dynamic Compression Experiments on OMEGA EP."

A. Howard, D. Turnbull, A. Davies, D. H. Froula, and J. P. Palastro, "Photon Acceleration in the Ionization Front of a Flying Focus."

S. X. Hu, R. Epstein, V. N. Goncharov, and E. M. Campbell, "Direct-Drive-Ignition Designs with Gradient-Density Double Shells."

M. Huff, J. R. Rygg, G. W. Collins, T. R. Boehly, M. Zaghoo, D. N. Polsin, B. J. Henderson, L. Crandall, D. E. Fratanduono, M. Millot, R. F. Smith, J. H. Eggert, P. M. Celliers, M. C. Gregor, and C. A. McCoy, "Measurements of Sound Speed in Iron Shock-Compressed to ~1 TPa."

I. V. Igumenshchev, R. C. Shah, R. Betti, E. M. Campbell, V. N. Goncharov, J. P. Knauer, S. P. Regan, A. Shvydky, A. L. Velikovich, and A. J. Schmitt, "Mitigating Imprint in Direct-Drive Implosions Using Rarefaction Flows."

V. V. Karasiev, S. X. Hu, M. Zaghoo, and T. R. Boehly, "Study of the Exchange-Correlation Thermal Effects for Transport and Optical Properties of Shocked Deuterium."

J. P. Knauer, C. Stoeckl, R. Betti, V. Gopalaswamy, K.S. Anderson, D. Cao, M. J. Bonino, E. M. Campbell, T. J. B. Collins, C. J. Forrest, V. Yu. Glebov, V. N. Goncharov, D. R. Harding, J. A. Marozas, F. J. Marshall, P. W. McKenty, P. B. Radha, S. P. Regan, T. C. Sangster, and R. C. Shah, "Burn-Rate Measurements from the High-Performance Cryogenic Implosion Campaign on OMEGA."

L. S. Leal, A. V. Maximov, A. B. Sefkow, R. Betti, and V. V. Ivanov, "Modeling of a Laser-Generated Plasma in MG Magnetic Fields."

O. M. Mannion, K. S. Anderson, C. J. Forrest, V. Yu. Glebov, J. P. Knauer, Z. L. Mohamed, S. P. Regan, T. C. Sangster, R. C. Shah, C. Stoeckl, and M. Gatu Johnson, "Integrated Analysis of Nuclear Measurements from the Target-Offset Campaign on OMEGA."

J. A. Marozas, G. D. Kerbel, M. M. Marinak, and S. Sepke, "Implementation of the Low-Noise, 3-D Ray-Trace Inverse-Projection Method in the Radiation-Hydrodynamics Code *HYDRA*."

F. J. Marshall, V. N. Goncharov, J. H. Kelly, T. Z. Kosc, and A. Shvydky, "*In Situ* Measurements of Direct-Drive Illumination Uniformity on OMEGA."

A. V. Maximov, J. G. Shaw, R. W. Short, and J. P. Palastro, "Saturation of Stimulated Raman Scattering in Inhomogeneous Plasma."

P. W. McKenty, T. J. B. Collins, J. A. Marozas, E. M. Campbell, K. Molvig, and M. J. Schmitt, "Numerical Investigation of Laser Imprint Mitigation in *Revolver* Ignition Designs."

A. L. Milder, P. Franke, J. Katz, J. P. Palastro, S. T. Ivancic, J. L. Shaw, A. S. Davies, I. A. Begishev, R. H. Cuffney, M. Spilatro, and D. H. Froula, "Measurement of the Langdon Effect in Laser-Produced Plasma Using Collective Thomson Scattering."

S. C. Miller, J. P. Knauer, C. J. Forrest, V. Yu. Glebov, O. M. Mannion, W. T. Shmayda, T. J. B. Collins, J. A. Marozas, K. S. Anderson, P. B. Radha, and V. N. Goncharov, "Deceleration-Phase Rayleigh–Taylor Growth Effects on the Performance of Direct-Drive Implosions."

Z. L. Mohamed, J. P. Knauer, C. J. Forrest, and M. Gatu Johnson, "Wave-Function Amplitude Analysis of the ^{5}He Resonance in the TT Neutron Spectrum."

P. M. Nilson, F. Ehrne, C. Mileham, D. Mastrosimone, C. Taylor, R. K. Jungquist, R. Boni, J. Hassett, C. R. Stillman, S. T. Ivancic, D. J. Lonobile, R. W. Kidder, M. J. Shoup III, A. B. Sefkow, A. A. Solodov, W. Theobald, C. Stoeckl, S. X. Hu, D. H. Froula, K. W. Hill, L. Gao, M. Bitter, P. Efthimion, I. E. Golovkin, and D. D. Meyerhofer, "High-Resolving-Power, Streaked X-Ray Spectroscopy on the OMEGA EP Laser System."

J. P. Palastro, T. M. Antonsen, Jr., L. Nguyen, A. Colaïtis, R. K. Follett, D. Turnbull, J. Vieira, and D. H. Froula, "Cherenkov Radiation from a Plasma."

D. Patel, R. Betti, V. Gopalaswamy, J. P. Knauer, K. M. Woo, S. P. Regan, T. C. Sangster, C. Stoeckl, and F. J. Marshall, "A Novel Double-Spike Pulse Shape for OMEGA Cryogenic Implosions."

R. Paul, S. X. Hu, and V. V. Karasiev, "High-Pressure Phase Diagram of Silicon."

J. L. Peebles, J. R. Davies, D. H. Barnak, A. B. Sefkow, P. A. Gourdain, R. Betti, and A. V. Arefiev, "Characterizing Magnetic and Electric Fields from Laser-Driven Coils Using Axial Proton Probing."

D. N. Polsin, X. Gong, G. W. Collins, M. Huff, L. Crandall, T. R. Boehly, J. R. Rygg, A. Jenei, M. Millot, J. H. Eggert, and M. I. McMahon, "X-Ray Diffraction of Ramp-Compressed Sodium."

S. P. Regan, V. N. Goncharov, D. Cao, R. Epstein, R. Betti, M. J. Bonino, T. J. B. Collins, E. M. Campbell, C. J. Forrest, V. Yu. Glebov, D. R. Harding, J. P. Knauer, J. A. Marozas, F. J. Marshall, P. B. Radha, T. C. Sangster, R. C. Shah, C. Stoeckl, R. W. Luo, M. E. Schoff, and M. Farrell, "Dependence of Hot-Spot Mix in DT Cryogenic Implosions on the Design Adiabat."

H. G. Rinderknecht, D. T. Casey, R. Bionta, R. Hatarik, A. Moore, E. P. Hartouni, D. Scholssberg, G. P. Grim, O. L. Landen, and P. K. Patel, "Signatures of Systematic Azimuthal Asymmetry in Nuclear Diagnosis of ICF Implosions on the NIF."

M. J. Rosenberg, A. A. Solodov, R. K. Follett, W. Seka, S. P. Regan, R. Epstein, A. R. Christopherson, R. Betti, A. V. Maximov, T. J. B. Collins, V. N. Goncharov, R. W. Short, D. Turnbull, D. H. Froula, P. B. Radha, J. F. Myatt, P. Michel, M. Hohenberger, L. Masse, G. Swadling, J. S.

Ross, T. Chapman, J. D. Moody, J. W. Bates, and A. J. Schmitt, "Laser–Plasma Interaction Experiments at Direct-Drive Ignition-Relevant Scale Lengths at the National Ignition Facility."

J. J. Ruby, J. R. Rygg, C. J. Forrest, V. Yu. Glebov, D. A. Chin, G. W. Collins, B. Bachmann, J. A. Gaffney, Y. Ping, H. Sio, and N. V. Kabadi, "Measurement of Plasma Conditions at Shock Collapse on OMEGA."

R. Saha, J. Topp-Mugglestone, G. Gregori, T. White, S. P. Regan, G. W. Collins, and J. R. Rygg, "Atomic and Electronic Structure of Warm Dense Silicon."

J. L. Shaw, Z. Barfield, D. Haberberger, A. M. Hansen, J. Katz, D. Mastrosimone, D. H. Froula, F. Albert, P. M. King, N. Lemos, J. Williams, P. Fan, and Y. Lu, "Laser Wakefield Acceleration Platform for OMEGA EP."

A. Shvydky, D. Haberberger, J. Carroll-Nellenback, D. Cao, D. H. Froula, V. N. Goncharov, S. X. Hu, I. V. Igumenshchev, J. P. Knauer, J. A. Marozas, A. V. Maximov, P. B. Radha, S. P. Regan, and T. C. Sangster, "Numerical Simulations of Shock-Release OMEGA EP Experiments."

A. A. Solodov, M. J. Rosenberg, W. Seka, R. Epstein, R. W. Short, R. K. Follett, A. R. Christopherson, R. Betti, P. B. Radha, S. P. Regan, D. H. Froula, V. N. Goncharov, J. F. Myatt, P. Michel, M. Hohenberger, T. Chapman, J. D. Moody, J. W. Bates, and A. J. Schmitt, "Hot-Electron Generation and Preheat in Direct-Drive Experiments at the National Ignition Facility."

C. Stoeckl, T. J. B. Collins, R. Epstein, V. N. Goncharov, R. K. Jungquist, C. Mileham, P. B. Radha, S. P. Regan, T. C. Sangster, and W. Theobald, "Investigating Small Scale Mix in Direct-Drive Cryogenic DT Implosions with Radiography on OMEGA."

G. Tabak, M. Millot, T. R. Boehly, L. Crandall, B. J. Henderson, M. Zaghoo, S. Ali, P. M. Celliers, D. E. Fratanduono, S. Hamel, A. Lazicki, D. Swift, P. Loubeyre, R. Kodama, K. Miyanishi, T. Ogawa, N. Ozaki, T. Sano, R. Jeanloz, D. G. Hicks, G. W. Collins, J. H. Eggert, and J. R. Rygg, "Equation of State and Metallization of Methane Shock-Compressed to 400 GPa."

W. Theobald, R. Betti, A. Bose, S. X. Hu, E. M. Campbell, S. P. Regan, C. A. McCoy, A. Casner, L. Ceurvorst, and M. Karasik, "The Hybrid Target Approach: A Promising Path

Forward to Mitigate Laser Imprint in Direct Drive Inertial Confinement Fusion."

D. Turnbull, P. Franke, S.-W. Bahk, I. A. Begishev, R. Boni, J. Bromage, S. Bucht, A. Davies, D. Haberberger, J. Katz, T. J. Kessler, A. L. Milder, J. P. Palastro, J. L. Shaw, D. H. Froula, M. Edwards, Q. Jia, K. Qu, N. Fisch, N. Vafaei-Najabadi, J. Vieira, and F. Quéré, "Ionization Waves of Arbitrary Velocity."

K. M. Woo, R. Betti, O. M. Mannion, D. Patel, V. N. Goncharov, K. S. Anderson, P. B. Radha, J. P. Knauer, V. Gopalaswamy, A. R. Christopherson, E. M. Campbell, H. Aluie, D. Shvarts, J. Sanz, and A. Bose, "Impact of Three-Dimensional Hot-Spot Flow Asymmetry on Ion-Temperature Measurements in Inertial Confinement Fusion Experiments."

M. Zaghoo, G. W. Collins, T. R. Boehly, J. R. Rygg, V. V. Karasiev, S. X. Hu, and P. M. Celliers, "Breakdown of Fermi Degeneracy in the Simplest Liquid Metal" (invited).

H. Zhang, R. Betti, D. Zhao, H. Aluie, R. Yan, and D. Shvarts, "Self-Similar Multimode Bubble-Front Evolution of the Ablative Rayleigh–Taylor Instability in Two and Three Dimensions."

J. L. Peebles, J. R. Davies, D. H. Barnak, R. Betti, V. Yu. Glebov, E. C. Hansen, J. P. Knauer, K. J. Peterson, and D. B. Sinars, "Scaled Neutron-Yield Enhancement Using the Laser-Driven MagLIF Platform on the OMEGA Laser," presented at the MagLIF Meeting, Portland OR, 5–9 November 2018.

M. S. Wei, "Status of FY18 OLUG Findings and Recommendations," presented at OLUG Meeting at APS Division of Plasma Physics, Portland OR; 6 November 2018.

The following presentations were made at Technology of Fusion Energy 2018, Orlando, FL, 11–15 November 2018:

C. Fagan, M. Sharpe, W. T. Shmayda, and W. U. Schröder, "Tritium Retention in Hexavalent Chromate-Conversion–Coated Aluminum Alloy."

J. L. Peebles, J. R. Davies, D. H. Barnak, R. Betti, V. Yu. Glebov, E. C. Hansen, J. P. Knauer, K. J. Peterson, and D. B. Sinars, "Pulsed-Power and Laser-Driven Magnetized Liner Inertial Fusion."

M. Sharpe, C. Fagan, and W. T. Shmayda, "Distribution of Tritium in the Near Surface of 316 Stainless-Steel."

W. T. Shmayda, C. R. Shmayda, and J. Torres, "Tritium Extraction from Water."

———————

T. C. Sangster, "Status of Laser-Direct-Drive Fusion in the U.S.," presented at the Institute of Applied Physics and Computational Mathematics, Beijing, China, 29–30 November 2018.

———————

D. H. Froula, C. Dorrer, E. M. Hill, R. K. Follett, A. A. Solodov, J. P. Palastro, D. Turnbull, D. H. Edgell, J. Bromage, T. J. Kessler, J. G. Shaw, A. M. Hansen, A. L. Milder, J. Katz, R. Boni, J. D. Zuegel, V. N. Goncharov, E. M. Campbell, P. Michel, D. Strozzi, M. Glensky, K. Peterson, J. W. Bates, A. Schmitt, J. L. Weaver, and J. F. Myatt, "Innovative Science and Broadband Lasers at LLE—A Path to an Expanded ICF Design Space," presented at Fusion Power Associates 39th Annual Meeting and Symposium, Washington, DC, 4–5 December 2018.

———————

The following presentations were made at the Joint U.S./Israel Workshop on High-Energy-Density Physics, Tel Aviv, Israel, 10–12 December 2018:

R. Betti, "Fusion Research at LLE: Direct Drive and Magnetized Targets."

T. R. Boehly, "High-Energy-Density Physics Research at LLE."

E. M. Campbell, "NIF—An Unexpected Journey, Lessons Learned to Secure "Projects of Scale" and the Future of ICF Research."

T. C. Sangster, "Overview of the Laboratory for Laser Energetics."

J. D. Zuegel, C. Dorrer, E. M. Hill, R. K. Follett, A. A. Solodov, J. P. Palastro, D. Turnbull, D. H. Edgell, J. Bromage, T. J. Kessler, J. G. Shaw, A. M. Hansen, A. L. Milder, J. Katz, R. Boni, V. N. Goncharov, E. M. Campbell, P. Michel, D. Strozzi, M. Glensky, K. Peterson, J. W. Bates, A. Schmitt, J. L. Weaver, and J. F. Myatt, "Laser–Plasma Instabilities and R&D Plans for Fourth-Generation ICF Lasers."